Title
Magnetostrictive Ferri & Antiferromagnetic Thin Films for Multiferroic Applications

Author
Shirazi, Paymon

Publication Date
2021

Peer reviewed|Thesis/dissertation

UNIVERSITY OF CALIFORNIA

Los Angeles

Magnetostrictive Ferri & Antiferromagnetic Thin Films for Multiferroic Applications

A dissertation submitted in partial satisfaction of the
requirements for the degree of Doctor of Philosophy
in Mechanical Engineering

by

Paymon Shirazi

2021

ABSTRACT OF THE DISSERTATION

Magnetostrictive Ferri & Antiferromagnetic Thin Films for Multiferroic Applications

by

Paymon Shirazi

Doctor of Philosophy in Mechanical Engineering

University of California, Los Angeles, 2021

Professor Gregory P. Carman, Chair

Over the last decade, the multiferroic concept has shown considerable success in numerous device applications requiring the control of magnetism through voltage-induced strains generated by piezoelectrics coupled to magnetostrictive materials. This approach in the control of magnetism overcomes the associated challenges with device reduction such as decreased energy efficiency by application of voltages instead of currents for operation, leading to the efficient and effective control of magnetism at reduced dimensions. Consequently, there has been an increasing demand for superior thin-film magnetostrictive materials possessing large magnetostriction and lower strain-mediated switching thresholds targeted towards micro and nanoscale multiferroic applications. As materials with these properties are critically vital for future multiferroic applications, further material development coupled with innovative investigation methods are required to meet this demand. This dissertation addresses these scientific requirements by demonstrating relevant developments and investigations on magnetostrictive ferrimagnetic and antiferromagnetic thin films for next generation multiferroic applications. In ferrimagnetic magnetostrictive $Tb_{0.3}Dy_{0.7}Fe_2$ (Terfenol-D) and multilayer

$Ni_{81}Fe_{19}/TbFe_2$ thin films, the atomic level spin and orbital moments are measured by X-ray magnetic circular dichroism (XMCD) to determine the contributions of specific elements towards various components of the magnetic anisotropy and the interface-mediated exchange coupling interaction respectively. In antiferromagnetic γ-FeMn thin films, the influence of stress (i.e. strain) on the orientation of the Néel vector is studied and an indirect method for the calculation of the saturation magnetostriction λ_s by AC magnetic susceptibility measurements are demonstrated. The results presented in this dissertation aid in the development of superior energy-efficient and effective magnetostrictive ferri and antiferromagnetic thin films to meet the growing demand of micro and nanoscale magnetic devices for future multiferroic applications.

The dissertation of Paymon Shirazi is approved.

Robert N. Candler

Pei-Yu Chiou

Yongjie Hu

Gregory P. Carman, Committee Chair

University of California, Los Angeles

2021

For my family and friends, your continued support has made this possible.

TABLE OF CONTENTS

LIST OF FIGURES

Page

LIST OF TABLES

Page

ACKNOWLEDGMENTS

This work has been accomplished with the support of many inspiring individuals. Professor Carman, I would like to express my sincere gratitude in allowing me to explore new and cutting edge research topics which have allowed me to become the researcher am I today. I am very fortunate to have a graduate advisor who appreciates my potential and strengths, which has enabled me to have the confidence in the knowledge I know today. I believe that through your guidance since my arrival at UCLA, I have grown much more immensely as researcher with more knowledge on magnetic materials than I had initially imagined. Due to your continued support, I was able to perform any necessary research in the UCLA cleanrooms in addition to research opportunities at the state-of-the-art synchrotron facilities.

Additionally, I would like to express my sincere gratitude to my committee members, Professors, Eric Chiou, Yongjie Hu, and Robert Candler. You have all inspired me to be become a more critical researcher due to the material I have learned either directly or indirectly from your lectures, discussions/presentations on your research, or from discussions with your graduate students. You have directly inspired me to work harder and become a better researcher in numerous ways. For these reasons, I am grateful and honored to have you serve on my Ph.D committee.

I would like to thank Dr. Mohanchandra Panduranga of the Active Materials Lab (AML) who has significantly helped me in my time as Ph.D student at UCLA. His consistent desire and aptitude to progress forward on our combined work has enabled me to achieve many of the results presented in this dissertation and has my eternal gratitude. Furthermore, I would like to thank Dr. Alpha T. N'Diaye from the Advanced Light Source (ALS) at the Lawrence Berkeley National Laboratory (LBNL) for his guidance, discussions, and training on X-ray magnetic circular dichroism (XMCD). Without his support, the content presented in chapters 4 & 5 of this dissertation would not be possible. Additionally, I would like to

thank my mentor, Dr. Subrata Sanyal from the Naval Surface Warfare Center - Corona Division, for selecting me for the Science Mathematics & Research for Transformation (SMART) Scholarship, followed by his tireless support through the Ph.D. program and summer internships. To my undergraduate research advisor, Professor Nosang V. Myung, thank you for introducing me to research and for your continued support on my piezoelectric nanofiber research. Our combined discussions over coffee with Dr. Youngwoo Rheem spurred my deep interest in magnetic materials "as researchers did not really understand them".

I am fortunate to be a part of the Active Materials Lab (AML) whom is composed of some of the most interesting, up-beat & fun, diverse, and knowledgeable individuals I have encountered in my life. I recall the first day I visited the Active Materials Lab (AML) as an undergraduate and met my future lab-mate Tony Barra. We instantly clicked, exchanged numbers (we even had a common area code (i.e. 949)) and discussed a few topics on piezoelectric materials. I appreciate your willingness to always help and provide your ideas on topics involving magnetics. Additionally, it is due to the discussion I had with you that I am able to understand antiferromagnetism and their complex behavior. Today, and along with Devin Schneider we still play Escape from Tarkov from time to time. Devin you are also one of the most interesting individuals I have met both scientifically and on a personal level. I greatly enjoyed our discussions on magnetic phenomena, quantum mechanics, and on topics related to Iran. Andres Chavez, you were very quiet yet very nice, and once I got to know you we had more in common than I had expected. Thank you for being very helpful and teaching me the fundamentals of magnetism in my first year of the program. Auni Kundu, our honorary guest in the Carman lab, I am forever grateful for our friendship. You have always brightened the room, brought everyone together from coffee breaks to lab outings, and made sure that everyone was doing alright in the graduate program. Ted (Taehwan) Lee, I owe you most of my Ph.D dissertation as most of the work presented here are based off of your ideas. You have always helped me succeed in research and experiments, and you even trained me on the Denton sputtering machine in the Nanolab that accelerated my research

at UCLA. QC and Cai Chen you were always very nice although we did not talk much as our research did not have much overlap.

To my other labmates who have not yet graduated, I am fortunate to have worked with all of you. John Nance you are very quiet but once you open up, you are a pretty interesting guy. Thank you for your invites to trivia nights, you are quite knowledgeable on content outside of the lab. Micheal Guevara De Jesus, without your support I would not be able to understand the various anisotropic contributions to the magnetic anisotropy. Thank you for making many cafe lattes and for our somewhat scientifically useful discussions in the mornings. Yu-Ching Hsaio, thank you for being you and always bringing up everyone's spirit in lab. I am grateful to have you as both a labmate and as a friend and you make some mean taro gummies. Matthew McIntosh and Victor Estrada, you two are my Dallas area labmates, what a small world. I enjoyed our conversations on many topics greatly and glad to be able to have you both as labmates and friends. Jesse Rivera, we are both sometimes commuters and I greatly enjoyed our discussions in the early mornings. Some of the topics we discussed have substantially opened my mind to new ideas about the world. Emily Burnside, thank you for being the kindest person I have encountered to date. Thank you for taking care of us in lab with food and goodies, you have really helped us out in our darkest days, for which I am eternally grateful for. Also you were the only labmate that I have taken courses with from my time at UCLA. Shreya Patel, you joined our lab too late even though you have been a part of TANMS since I joined in 2017. I wish we could have had you as an honorary member of the lab a long time ago. Malcolm Jackson, you were also one of the kinder and more open-minded individuals I have encountered. I remember the talks we had when you were presenting your poster at the TANMS annual reviews, I learned so much from you in both DFT and Mumax3. Rouda Zheng, you are quiet too (mainly because you are busy), but have always been nice and very helpful.

To friends outside of lab, this could not have achieved without your support. Brian Mac-

Donald and Corey Kruczek, if you two did not push me to pursue my Ph.D. studies at UCLA, I would be writing this dissertation entirely differently. I am eternally grateful for your genuine friendship from the get-go brothers. Nima Moravedje, I am grateful to what you have done for me from my first day at UCLA to the last. I would have never been able to enjoy UCLA and LA the same if it were not for you brother. Soroosh Daraie, you always ask how I am doing and how things are in the Ph.D. program, for this I thank you brother. Ryin Rouzbehani, thank you for always lighting up the room and being down for events which have gotten me out of comfort zone during my Ph.D. brother. Arad Saebi and Behdad Farajnejad, I cannot believe that we have known each other from physics class at Saddleback community college, thank you for your continued friendship all this time. To Babak Fard-Moghadam, Farshid Allahakbari, and Ali Hashemi, I sincerely appreciate the experiences we had in our time at FUTEK, which are unforgettable. Atessa Sanjarvash, thank you for your tireless friendship over the years, you have taught me many valuable and irreplaceable lessons in my life. Additionally, significant portions of this dissertation was prepared during our virtual study sessions over the COVID-19 pandemic. Jennifer Luu, thank for initially choosing to be friends with a Ph.D. student during his last year of the program. Thank you for making my last year of the program much more enjoyable and memorable, I would like to express my deepest appreciation for your care and patience with me towards the end of my program.

Furthermore, I would like to formally acknowledge the use of the fabrication facility at the Integrated Systems Nanofabrication Cleanroom (ISNC) and the Molecular Instrumentation Center (MIC) at the California NanoSystems Institute (CNSI) at UCLA. This content is based upon work supported by or in part by the Army Research Laboratory and the U.S. Army Research Office Grant No. W911NF-17-0364. I gratefully acknowledge support from the National Science Foundation (NSF) through the Cooperative Agreement Award No. EEC-1160504 for solicitation NSF 11-537 (TANMS). This research used resources of the Advanced Light Source, a U.S. DOE Office of Science User Facility under Contract No. DE-

AC02-05CH11231. Magnetic data were acquired on a SQUID magnetometer supported by No. NSF MRI-1625776. Moreover, I personally would like to acknowledge support from the Department of Defense Science Mathematics and Research for Transformation (SMART) scholarship.

VITA

Paymon Shirazi

EDUCATION

University of California, Riverside — *Riverside, CA*

Bachelor of Science in Chemical Engineering — **2017**

University of California, Los Angeles — *Los Angeles, CA*

Master of Science in Mechanical Engineering — **2021**

RESEARCH EXPERIENCE

Undergraduate Research Assistant — **2015–2017**

University of California, Riverside — *Riverside, California*

PROFESSIONAL EXPERIENCE

Engineering Intern — **2014–2017**

FUTEK Advanced Sensor Technology — *Irvine, CA*

PUBLICATIONS

1. **Shirazi, P.**, Panduranga, M.K., Lee T., Barra, A., Estrada V., Tran D., & Carman, G.P. (2021). Strain-Induced Nèel Vector Reorientation and Magnetostriction in Antiferromagnetic γ-FeMn Thin Films. **Under Preparation**.

2. **Shirazi, P.**, Lee T., Panduranga, M.K., NĎiaye, A.T., Barra, A., Jackson M.A., Gue-

vara De Jesus M., McIntosh M.M., Wang K.L., & Carman, G.P. (2021). Tb Moment Enhancements in Soft Exchange Coupled $TbFe_2/Ni_{81}Fe_{19}$ Multilayers. **Applied Physics Letters**. *Under Review*

3. Hsiao Y.C., Gopman D.B., Mohanchandra K., **Shirazi, P.**, Lynch C.S., (2021). Effect of Interfacial and Edge Roughness on Magnetoelectric Control of Co/Ni Microdisks on PMN-PT(011). **Scientific Reports**. *Under Review*

4. Guevara De Jesus M., Xiao Z., Goiriena-Goikoetxea M., Chopdekar R.V., Panduranga M.K., **Shirazi, P.**, ..., & Lynch C.S., (2021). Magnetic State Switching in FeGa Microstructures. **Smart Materials & Structures**. *Under Review*

5. Barra, A., Ross, A., Gomonay, O., Baldrati, L., Chavez, A., Lebrun, R., ... **Shirazi. P.** , ... Kläui, M. (2021). Effective strain manipulation of the antiferromagnetic state of polycrystalline NiO. **Applied Physics Letters**, 118(17), 172408.

6. **Shirazi, P.**, Lee, T., Panduranga, M.K., N'Diaye, A.T., Barra, A., & Carman, G.P. (2021). Rare-Earth Orbital Moment Contributions to the Magnetic Anisotropy in Magnetostrictive $Tb_{0.3}Dy_{0.7}Fe_2$.**Applied Physics Letters**, 118(16), 162401.

7. Schneider, J.D., Domann, J.P., Panduranga, M. K., Tiwari, S., **Shirazi, P.**, Yao, Z., ... Carman, G.P. (2019). Experimental Demonstration and Operating Principles of a Multiferroic Antenna. **Journal of Applied Physics**, 126(22), 224104.

8. **Shirazi, P.**, Ico, G., Anderson, C.S., Ma, M.C., Kim, B.S., Nam, J., & Myung, N.V. (2017). Size-dependent Piezoelectric Properties of Electrospun $BaTiO_3$ for Enhanced Energy Harvesting. **Advanced Sustainable Systems**, 1(11), 1700091.

Chapter 1

Introduction

1.1 Motivation

Controlling the orientation of the magnetic moment is a critical component in virtually all applications involving magnetic materials for operation. Reorientation of the moment is achieved by overcoming the magnetic anisotropy which dictates and governs the orientation of the magnetic moment in materials. There are numerous approaches that facilitate overcoming the magnetic anisotropy utilizing applied magnetic fields [1, 2], electrical currents by methods such as spin-transfer torque (STT) [3] & spin-orbit torque (SOT) [4], using voltages (i.e. electric fields) through voltage-controlled magnetic anisotropy (VCMA) [5], thermally induced methods using lasers [6] or electrical currents/voltages [7], in addition to numerous abstract methods that are not mentioned here. However, in comparison, the multiferroic approach employing voltage-induced strains from piezoelectrics coupled to magnetostrictive materials has shown widespread success in the efficient and effective control of the orientation of the magnetic moment. The magnetic moment has been successfully reoriented and controlled by this method in devices ranging from the nano/micro-scale to one's on the con-

tinuum in areas involving cell-sorting [8], high & ultra-low frequency antennas [9], sensor & actuators [10], and magnetic random access memory [11], demonstrating its applicability to a wide array of applications.

Following the rapid progression of the multiferroic approach in these sectors, there is an increased demand for new magnetostrictive materials with improved properties to further reduce energy consumption and increase device efficiencies[12]. Namely, one of the most important material parameters for these efforts are to develop materials with larger saturation magnetostriction at lower saturation fields. In the past, one of the most sought-out methods to develop new materials with these properties have been through reducing the magnetocrystalline anisotropy (MCA) preformed by alloying and optimizing material compositions [13, 14]. This was first demonstrated in rare-earth ferrimagnetic $Tb_{0.3}Dy_{0.7}Fe_2$ (Terfenol-D), which today is one of the most widely investigated giant magnetoelastic materials due to its large room temperature magnetostriction with small magnetocrystalline anisotropy (MCA) [15]. The magnetic properties of Terfenol-D were engineered by alloying ferrimagnetic $TbFe_2$ with $DyFe_2$ to minimize the MCA while retaining large magnetostriction [16, 17]. Researchers studied various compositions to optimize the magnetostriction while minimizing the MCA for sonar applications and termed this selected composition (i.e. $Tb_{0.3}Dy_{0.7}Fe_2$) Terfenol-D [18].

More recently, rare-earth thin films such as Terfenol-D are becoming more heavily utilized in applications, specially cell-sorting devices due to their large single-domain states [19, 20]. As a result, it is also important to investigate the magnetoelastic contributions towards the magnetic anisotropy as the residual stresses present in thin films influence the dynamics of the magnetic moment altering the anisotropic energy barrier for device operation [21]. However, there are challenges with studying and optimizing the magnetic anisotropy by alloying as done in the past. Investigations of complex ternary intermetallic alloys such as Terfenol-D (i.e. $TbFe_2$ & $DyFe_2$) composed of two distinct alloys are challenging as the electronic

structures of the $TbFe_2$ and $DyFe_2$ are much different separately, than when alloyed together [22, 23]. Additionally, the MCA and magnetoelastic anisotropy (i.e. magnetostriction) arise from spin-orbit coupling in the crystal lattice which are dictated by the spin and orbital angular momenta of the rare-earth elements these materials. Therefore, in order to more accurately examine the magnetic responses due to alloying in intermetallics, the spin and orbital moment responses of the elemental components (i.e. Tb, Dy, & Fe) need to separately examined.

An alternative method to overcome the large MCA (i.e. anisotropy) in magnetostrictive materials for multiferroic applications has been successfully achieved through a multilayer approach, utilizing layers composed of repeating harder-magnetostrictive and ultra soft-magnetic layers. This has been demonstrated in multilayers of amorphous rare-earth transition metal (RE-TM) alloys and antiparallelly exchange coupled nanocrystalline transition metals (TMs). It has been found that these materials in a multilayer structure possess superior magnetic properties such as decreased damping, lower saturation and coercive fields, and enhanced magnetostriction as contrasted to their intrinsic monolithic layers. Various studies have shown that these property improvements originate from magnetic interactions at the interfaces due to competing anisotropic energies (e.g. exchange, magnetoelastic, perpendicular, etc.) producing localized magnetic order/disorder in the RE-TM layers [24, 25, 26]. However, due to the material complexity as well as access to sophisticated measurement systems, focused studies on RE-TM/TM multilayers have been limited in developing a more complete understanding of the underlying physics governing these property enhancements. Therefore, closer examination of the local interactions are warranted to better understand and subsequently design future multilayered RE-TM/TM heterostructures with specific property improvements.

Experimental work and micromagnetic simulations on RE-TM/TM multilayers have shown improvements in magnetostriction and reduced coercive fields compared to their monolithic

thin film counterparts [27, 28]. In amorphous $Tb_{41}Fe_{59}/Fe_{83}Al_{17}$ multilayers, interface interactions including localized interlayer stresses reduced the coercive field by 50% while retaining similar magnetostriction as monolithic $TbFe_2$ films [29]. In a related study conducted on $TbFe_2$/Co multilayers, researchers demonstrated the field to reach magnetic saturation was reduced by 38% [30] through a reported exchange interaction at the interface. In $TbFe_2/Fe_3Ga$ multilayers, coercive fields smaller than either of the monolithic films were reported by maximizing the antiparallel exchange coupling between layers [31], which was more recently attributed to the competition between antiferromagnetic (i.e. antiparallel) exchange and domain wall energies present at the interfaces [32]. In all of these studies, the property enhancements originated from spin-spin interactions and spin-orbit coupling [33] and require additional studies at spin and orbital moment levels to better understand the underlying sources leading to these property improvements.

Measurement techniques such as soft X-ray absorption (XAS) and X-Ray magnetic circular dichroism (XMCD) paired with the XMCD sum rule calculations have been used to study elemental spin-orbit moments and their influence on the magnetic anisotropy in various materials [34, 35, 36]. These studies are performed by lowering temperatures to increase the magnetic anisotropy due to stronger spin-orbit coupling that can be accurately measured by XMCD [33]. XAS and XMCD spectroscopy have also been successfully utilized to study element specific magnetic behavior in layered magnetic structures [37, 38]. In this space, several investigations have been performed on RE-TM/TM bilayers with relatively few studying multilayers. Through luminescence yield detection techniques, the entire multilayer structure can be studied to determine the combined effects of all the interface-mediated interlayer interactions in these complex heterostructures. Consequently, it appears that XAS and XMCD offer a viable approach for the study of the various anisotropic contributions in complex intermetallic rare-earth alloys in addition to the interface-mediated interactions in magnetic multilayered systems, which may offer useful information to researchers developing new materials for the multiferroics community.

As an alternative to ferromagnetic (FM) materials, antiferromagnets (AFMs) have recently garnered heavy research attention due to their unique material properties. Louis Néel who won the Nobel prize in 1970 for his discovery of the antiparallel nature and behavior of AFMs famously claimed "they are interesting, but useless" in his laureate speech. However, this belief instantaneously changed overnight as in the early 2010's the successful 90°reorientation of the Néel vector in several collinear metallic AFMs by spin-orbit torques (SOTs) were demonstrated [39, 40, 41]. Their lack of stray-fields [42], intrinsically faster resonances [43], and the ability to be manipulated by SOTs have significantly attracted attention the attention of researchers developing the next generation of magnetic memory devices. Additionally, the availability of AFMs with metallic [44], semiconducting [45], or insulating material properties [46] allows their readily availability towards a wider array of device designs and configurations. However, their prospects in the multiferroic field are largely unknown, as it is implied that AFMs possess magnetostrictive properties similar to FMs, but the experimental measurement of the saturation magnetostriction in AFM thin-films have not been successfully demonstrated.

Measurement of the magnetostrictive properties in AFMs have been widely absent due to the difficulty in the application of the large magnetic fields required to saturate AFMs beyond their spin-flop field (H_{sf}). Direct measurement of the magnetostriction in AFMs began with the bulk room-temperature AFM NiO, reporting magnetostriction values up to -20 ppm [47, 48]. However, measurement of the magnetostrictive properties in other AFMs have been increasingly difficult as most results have been widely contradicting. In metallic AFMs, investigations on the bulk polycrystalline γ-FeMn alloys have shown considerably large magnetostriction with results ranging from 350 [49] to 750 ppm [50] originating from one group. However, more recent investigations on bulk γ-FeMn alloys have contradicted previous results with the reported absence of magnetostriction in several compositions of γ-$Fe_{1-x}Mn_x$ (x=0.38, 0.42, 0.46, 0.50, & 0.56) [51]. Additionally, experimental results and first-principles calculations for metallic AFMs show that the pre-stress state of the material

is important in obtaining AFMs with magnetostriction. For instance, in γ-FeMn alloys, it was shown that magnetostriction is only obtained when the material is under compressive stresses [52, 53]. Therefore, the results of these combined studies indicate that γ-FeMn alloys may possess magnetostrictive properties which are governed by the pre-stress-state (i.e. compressive stress) demanding further experimental investigation. These results are necessary to demonstrate the magnetostrictive properties in AFM thin films which will allow these materials to become utilized in future multiferroic applications.

This dissertation addresses new investigation methods for the design of magnetostrictive intermetallic and multilayered materials with superior magnetic properties tailored for multiferroic applications. This is demonstrated by element specific investigations of the spin and orbital momenta by XMCD and the XMCD sum rule approach which is utilized to study the elements that control the MCA and magnetoelastic anisotropic responses in complex intermetallics such as Terfenol-D. Additionally, similar investigations by XMCD and its sum rule calculations are shown in this dissertation on multilayered RE-TM/TM heterostructures which show magnetization enhancements with ultra soft magnetic responses due to interface mediated interactions between specific elements in the hard-magnetostrictive and the ultra-soft layers. Furthermore, the in-plane to out-of-plane 90°reorientation of the Néel vector with applied stresses (i.e. strains) in polycrystalline metallic AFM thin-films are presented to showcase the magnetoelastic response and the saturation magnetostriction in AFM thin films. The results presented in this dissertation aid in the development of superior energy-efficient and effective magnetostrictive ferri and antiferromagnetic thin films to meet the growing demand of micro and nanoscale magnetic devices in future multiferroic applications.

1.2 Dissertation Overview

Chapter 2 provides the fundamental concepts of magnetism discussed in this dissertation. This chapter begins by illustrating the origin of magnetism in materials at the atomic level. Further, a brief overview of the various types of magnetic ordering are introduced to provide the background for the research conducted on ferri and antiferromagnetic systems. Furthermore, the magnetization process and the origins of the hysteric behavior are briefly discussed to provide an introduction to the various energies that contribute towards the magnetic anisotropy, which is heavily referenced in chapters 4-6 of this dissertation.

Chapter 3 of this dissertation provides the background required to understand the X-Ray magnetic circular dichroism (XMCD) results in chapters 4 and 5. This first begins with the brief overview of the interaction of transmitting X-Rays with matter. Subsequently, X-Ray absorption (XAS) in materials are introduced followed by XAS several detection methods typically used in XAS experiments since these are prerequisites in understanding XMCD. Next, the fundamental concepts that produce the dichroic responses in magnetic materials with a net spontaneous magnetization in response to polarized circular X-Rays are provided to understand XMCD spectroscopy. Finally, the XMCD sum rules are introduced which utilize both the XAS and XMCD spectra in magnetic materials to determine the elemental spin and orbital angular momenta which are vital for grasping the results in chapters 4 and 5.

In chapter 4, soft X-Ray Magnetic Circular Dichroism (XMCD) spectroscopy at the Dy and Tb $M_{4,5}$ and the Fe $L_{2,3}$ edges were performed on sputter deposited polycrystalline Terfenol-D ($Tb_{0.3}Dy_{0.7}Fe_2$) film on sapphire substrates at temperatures from 100 to 300 K to evaluate the elementwise contribution to the magnetocrystalline anisotropy and coercive field. The elemental spin and orbital magnetic moments were calculated using the X-Ray Magnetic Circular Dichroism sum rules. As temperatures decreased, the Tb and Fe moments plateau

at 200 K with values of 7.6 μ_B/atom and 1.8 μ_B/atom respectively while the Dy moment increases to 8.9 μ_B/atom at 100 K. Between 300 to 200 K the change in magnetic anisotropy is dominated by thermally induced magnetoelastic effects while for temperatures below 200 K magnetocrystalline anisotropy (MCA) changes are dominant. The MCA changes below 200 K appear to be due to increases in the Dy orbital moment with decreasing temperature in this temperature regime.

In chapter 5 explores moment enhancements in two multilayers composed of ultra-thin $Ni_{81}Fe_{19}$ and $TbFe_2$ (2nm/4nm or 4nm/2nm) layers using X-ray magnetic circular dichroism (XMCD). The elementwise XMCD results indicate that these enhancements are induced by interface mediated antiparallel exchange coupling between Tb in the $TbFe_2$ and Fe in the $Ni_{81}Fe_{19}$. XMCD M-H curves demonstrate this coupling is sufficient to provide pronounced saturation and reorientation in the Tb orbital and spin moments with coercive fields similar to monolithic $Ni_{81}Fe_{19}$ at or near the interfaces. Results also show increased magnetic ordering lengths within $TbFe_2$ layers as the $TbFe_2$ layer thickness increases.

In chapter 6, the residual stresses in magnetron sputtered polycrystalline FeMn thin films on Silicon substrates were varied by adjusting the deposition Argon pressure to study the influence of strain on the orientation of the Néel vector. Here, a strain-induced phase transition from α-FeMn to γ-FeMn is demonstrated by a -0.03% compressive strain (-55 MPa stress). Further, AC susceptibility measurements show an in-plane to out-of-plane reorientation (i.e. 90reorientation) in the γ-FeMn Néel vector followed by a 10 kOe increase in the spin-flop field resultant from a -0.028% compressive strain (-52 MPa stress). Calculations using measured AC and DC susceptibility data indirectly predict a saturation magnetostriction value of 116 ppm for γ-FeMn thin films.

Chapter References

[1] Saied Tehrani. Status and outlook of mram memory technology. In *2006 International Electron Devices Meeting*, pages 1–4. IEEE, 2006.

[2] Derac Son and Yuk Cho. Under water sonar transducer using terfenol-d magnetostrictive material. *Journal of magnetics*, 4(3):98–101, 1999.

[3] Zhitao Diao, Zhanjie Li, Shengyuang Wang, Yunfei Ding, Alex Panchula, Eugene Chen, Lien-Chang Wang, and Yiming Huai. Spin-transfer torque switching in magnetic tunnel junctions and spin-transfer torque random access memory. *Journal of Physics: Condensed Matter*, 19(16):165209, 2007.

[4] Shunsuke Fukami, T Anekawa, C Zhang, and H Ohno. A spin–orbit torque switching scheme with collinear magnetic easy axis and current configuration. *nature nanotechnology*, 11(7):621–625, 2016.

[5] Juan G Alzate, P Khalili Amiri, P Upadhyaya, SS Cherepov, J Zhu, M Lewis, R Dorrance, JA Katine, J Langer, K Galatsis, et al. Voltage-induced switching of nanoscale magnetic tunnel junctions. In *2012 International Electron Devices Meeting*, pages 29–5. IEEE, 2012.

[6] Richard FL Evans, Thomas A Ostler, Roy W Chantrell, Ilie Radu, and Theo Rasing. Ultrafast thermally induced magnetic switching in synthetic ferrimagnets. *Applied Physics Letters*, 104(8):082410, 2014.

[7] P Khalili Amiri, P Upadhyaya, JG Alzate, and KL Wang. Electric-field-induced thermally assisted switching of monodomain magnetic bits. *Journal of Applied Physics*, 113(1):013912, 2013.

[8] Reem Khojah, Zhuyun Xiao, Mohanchandra K Panduranga, Michael Bogumil, Yilian Wang, Maite Goiriena-Goikoetxea, Rajesh V Chopdekar, Jeffrey Bokor, Gregory P Carman, Rob N Candler, et al. Single-domain multiferroic array-addressable terfenol-d (smart) micromagnets for programmable single-cell capture and release. *Advanced Materials*, 33(20):2006651, 2021.

[9] Joseph D Schneider, John P Domann, MK Panduranga, Sidhant Tiwari, Paymon Shirazi, Zhi Yao, Casey Sennott, David Shahan, Skyler Selvin, Geoff McKnight, et al. Experimental demonstration and operating principles of a multiferroic antenna. *Journal of Applied Physics*, 126(22):224104, 2019.

[10] JM Barandiaran and J Gutierrez. Magnetoelastic sensors based on soft amorphous magnetic alloys. *Sensors and Actuators A: Physical*, 59(1-3):38–42, 1997.

[11] Zhiguang Wang, Yue Zhang, Yaojin Wang, Yanxi Li, Haosu Luo, Jiefang Li, and Dwight Viehland. Magnetoelectric assisted 180 magnetization switching for electric field addressable writing in magnetoresistive random-access memory. *ACS nano*, 8(8):7793–7800, 2014.

[12] TJ Moran and B Lüthi. Elastic and magnetoelastic effects in magnetite. *Physical Review*, 187(2):710, 1969.

[13] RQ Wu, LJ Chen, A Shick, and AJ Freeman. First-principles determinations of magneto-crystalline anisotropy and magnetostriction in bulk and thin-film transition metals. *Journal of magnetism and magnetic materials*, 177:1216–1219, 1998.

[14] A Kumagai, Asaya Fujita, K Fukamichi, K Oikawa, R Kainuma, and K Ishida. Mag-

netocrystalline anisotropy and magnetostriction in ordered and disordered fe–ga single crystals. *Journal of magnetism and magnetic materials*, 272:2060–2061, 2004.

[15] A E Clark and H S Belson. Giant room-temperature magnetostrictions in $TbFe_2$ and $DyFe_2$. *Physical Review B*, 5(9):3642, 1972.

[16] A E Clark, H S Belson, and N Tamagawa. Huge magnetocrystalline anisotropy in cubic rare earth-Fe_2 compounds. *Physics Letters A*, 42(2):160–162, 1972.

[17] A E Clark, H S Belson, and N Tamagawa. Magnetocrystalline anisotropy in cubic rare earth-Fe_2 compounds. In *AIP Conference Proceedings*, volume 10, pages 749–753. American Institute of Physics, 1973.

[18] Mark B Moffett, Arthur E Clark, Marilyn Wun-Fogle, Jan F Lindberg, Joseph P Teter, and Elizabeth A McLaughlin. Characterization of Terfenol-D for magnetostrictive transducers. *The Journal of the Acoustical Society of America*, 87(S1):S95–S95, 1990.

[19] Zhuyun Xiao, Roberto Lo Conte, Cai Chen, Cheng-Yen Liang, Abdon Sepulveda, Jeffrey Bokor, Gregory P Carman, and Robert N Candler. Bi-directional coupling in strain-mediated multiferroic heterostructures with magnetic domains and domain wall motion. *Scientific reports*, 8(1):1–10, 2018.

[20] Mohanchandra K Panduranga, Zhuyun Xiao, Joseph D Schneider, Taehwan Lee, Christoph Klewe, Rajesh Chopdekar, Padraic Shafer, Alpha T N'Diaye, Elke Arenholz, Rob N Candler, et al. Single magnetic domain Terfenol-D microstructures with passivating oxide layer. *Journal of Magnetism and Magnetic Materials*, page 167798, 2021.

[21] J I Arnaudas, C De La Fuente, M Ciria, L Benito, C Dufour, K Dumesnil, and A Del Moral. Magnetoelastic stresses in epitaxial (110) Terfenol-D thin films. *Journal of magnetism and magnetic materials*, 240(1-3):389–391, 2002.

[22] D M Eagles. Models for the heavy rare earth metals and (rare earth) Fe2 compounds involving 5d and 6s electrons. *Physik der kondensierten Materie*, 16(3):181–199, 1973.

[23] Paymon Shirazi, Taehwan Lee, Mohanchandra K Panduranga, Alpha T N'Diaye, Anthony Barra, and Gregory P Carman. Rare-earth orbital moment contributions to the magnetic anisotropy in magnetostrictive tb0. 3dy0. 7fe2. *Applied Physics Letters*, 118(16):162401, 2021.

[24] Colin R Rementer, Kevin Fitzell, Qiang Xu, Paul Nordeen, Gregory P Carman, Yuanxun E Wang, and Jane P Chang. Tuning static and dynamic properties of FeGa/NiFe heterostructures. *Applied Physics Letters*, 110(24):242403, 2017.

[25] IA Subbotin, EM Pashaev, AL Vasiliev, Yu M Chesnokov, GV Prutskov, EA Kravtsov, MV Makarova, VV Proglyado, and VV Ustinov. The influence of microstructure on perpendicular magnetic anisotropy in Co/Dy periodic multilayer systems. *Physica B: Condensed Matter*, 573:28–35, 2019.

[26] ZS Shan and David J Sellmyer. Magnetism of rare-earth–transition-metal nanoscale multilayers. I. experiments on Dy/Co, Dy/Fe, and Tb/Fe. *Physical Review B*, 42(16):10433, 1990.

[27] J Juraszek, A Grenier, J Teillet, N Tiercelin, F Petit, J Ben Youssef, and M Toulemonde. Swift ion irradiation of magnetostrictive multilayers. *Nuclear Instruments and Methods in Physics Research Section B: Beam Interactions with Materials and Atoms*, 245(1):157–160, 2006.

[28] F Petit, J Juraszek, J Ben Youssef, J Teillet, DT Dekadjevi, and H Le Gall. Effect of annealing on the structural and magnetic properties of giant magnetostrictive multilayers. *Journal of magnetism and magnetic materials*, 290:839–842, 2005.

[29] WANG Wei, MI Yiming, QIAN Shiqiang, and ZHOU Xiying. Magnetic and magne-

tostrictive properties of amorphous TbFe/FeAl multilayer thin film. *Journal of Rare Earths*, 26(4):571–574, 2008.

[30] A Grenier, J Juraszek, N Tiercelin, J Teillet, M Toulemonde, and JM Le Breton. Magnetostrictive properties of kr-ion irradiated multilayers. *Journal of magnetism and magnetic materials*, 310(2):2624–2626, 2007.

[31] R Ranchal, V Gutiérrez-Díez, and V González-Martín. Magnetic properties of nanostructured systems based on $TbFe_2$. *Journal of alloys and compounds*, 536:S329–S332, 2012.

[32] Pablo Bartolomé and Rocío Ranchal. Synthetic domain walls in $[TbFeGa/TbFe]_2$ multilayers. *Nanotechnology*, 31(33):335715, 2020.

[33] Bernard Dennis Cullity and Chad D Graham. *Introduction to magnetic materials*. John Wiley & Sons, 2011.

[34] B T Thole, Paolo Carra, F Sette, and Gerrit van der Laan. X-ray circular dichroism as a probe of orbital magnetization. *Physical review letters*, 68(12):1943, 1992.

[35] Paolo Carra, B T Thole, Massimo Altarelli, and Xindong Wang. X-ray circular dichroism and local magnetic fields. *Physical Review Letters*, 70(5):694, 1993.

[36] J Stöhr. Exploring the microscopic origin of magnetic anisotropies with X-ray magnetic circular dichroism (XMCD) spectroscopy. *Journal of Magnetism and Magnetic Materials*, 200(1-3):470–497, 1999.

[37] S Mangin, C Bellouard, S Andrieu, F Montaigne, P Ohresser, NB Brookes, and B Barbara. Magnetization reversal in exchange-coupled GdFe/TbFe studied by x-ray magnetic circular dichroism. *Physical Review B*, 70(1):014401, 2004.

[38] Biplab Sanyal, Carolin Antoniak, Till Burkert, Bernhard Krumme, Anne Warland, Frank Stromberg, Christian Praetorius, Kai Fauth, Heiko Wende, and Olle Eriksson.

Forcing ferromagnetic coupling between rare-earth-metal and 3 d ferromagnetic films. *Physical review letters*, 104(15):156402, 2010.

[39] Shunsuke Fukami, Chaoliang Zhang, Samik DuttaGupta, Aleksandr Kurenkov, and Hideo Ohno. Magnetization switching by spin–orbit torque in an antiferromagnet–ferromagnet bilayer system. *Nature materials*, 15(5):535–541, 2016.

[40] Jing Zhou, Xiao Wang, Yaohua Liu, Jihang Yu, Huixia Fu, Liang Liu, Shaohai Chen, Jinyu Deng, Weinan Lin, Xinyu Shu, et al. Large spin-orbit torque efficiency enhanced by magnetic structure of collinear antiferromagnet irmn. *Science advances*, 5(5):eaau6696, 2019.

[41] XF Zhou, J Zhang, F Li, XZ Chen, GY Shi, YZ Tan, YD Gu, MS Saleem, HQ Wu, F Pan, et al. Strong orientation-dependent spin-orbit torque in thin films of the antiferromagnet mn 2 au. *Physical Review Applied*, 9(5):054028, 2018.

[42] Tomas Jungwirth, X Marti, P Wadley, and J Wunderlich. Antiferromagnetic spintronics. *Nature nanotechnology*, 11(3):231–241, 2016.

[43] Anthony Barra, John Domann, Ki Wook Kim, and Greg Carman. Voltage control of antiferromagnetic phases at near-terahertz frequencies. *Physical Review Applied*, 9(3):034017, 2018.

[44] Saima A Siddiqui, Joseph Sklenar, Kisung Kang, Matthew J Gilbert, André Schleife, Nadya Mason, and Axel Hoffmann. Metallic antiferromagnets. *Journal of Applied Physics*, 128(4):040904, 2020.

[45] I Fina, X Marti, D Yi, J Liu, JH Chu, C Rayan-Serrao, S Suresha, AB Shick, J Železnỳ, T Jungwirth, et al. Anisotropic magnetoresistance in an antiferromagnetic semiconductor. *Nature communications*, 5(1):1–7, 2014.

[46] Natascha Hedrich, Kai Wagner, Oleksandr V Pylypovskyi, Brendan J Shields, Tobias Kosub, Denis D Sheka, Denys Makarov, and Patrick Maletinsky. Nanoscale mechanics of antiferromagnetic domain walls. *Nature Physics*, 17(5):574–577, 2021.

[47] L Alberts and EW Lee. Magnetostriction in antiferromagnetic nickel oxide. *Proceedings of the Physical Society (1958-1967)*, 78(5):728, 1961.

[48] TR McGuire and WA Crapo. Magnetic susceptibility and magnetostriction of coo, mno, and nio. *Journal of Applied Physics*, 33(3):1291–1292, 1962.

[49] WY Peng and JH Zhang. Magnetostriction studies in an antiferromagnetic polycrystalline mn 42 fe 58 alloy. *Applied physics letters*, 89(26):262501, 2006.

[50] Aina He, Tianyu Ma, Jingjing Zhang, Wei Luo, and Mi Yan. Antiferromagnetic mn50fe50 wire with large magnetostriction. *Journal of magnetism and magnetic materials*, 321(22):3778–3781, 2009.

[51] R Sato Turtelli, C Grijalva, F Kubel, D Geist, R Grössinger, M Kriegisch, S Sorta, M Zehetbauer, and N Mehmood. Low magnetostriction in fe100-xmnx (x= 45, 48, 50, 52, 55) alloys. In *IOP Conference Series: Materials Science and Engineering*, volume 60, page 012006. IOP Publishing, 2014.

[52] E Linville, D Han, J Judy, J Sivertson, and S Mao. Stress effects on the magnetic properties of femn and nimn spin valves. *IEEE transactions on magnetics*, 34(4):894–896, 1998.

[53] Jan-Philipp Hanke, Frank Freimuth, Stefan Blügel, and Yuriy Mokrousov. Prototypical topological orbital ferromagnet γ-femn. *Scientific reports*, 7(1):1–7, 2017.

Chapter 2

Scientific Background

2.1 The Origin of Magnetism in Materials

At the atomic level, magnetism originates from the magnetic dipole moments of individual atoms. The net magnetic dipole moment in atoms arise due to partially filled electrons shells (i.e. unpaired electrons) that contribute their orbital and spin angular momenenta. The orbital angular momentum arises from the electrons orbiting the atomic nuclei whereas the spin angular momentum is an intrinsic property of an electron originating from quantum mechanics and lacks a classical counterpart. To show this in better prospective, consider an electron moving around an atomic nucleus in a Bohr orbit of radius r, with velocity v, with mass m_e, and charge e^- as shown in figure 2.1. The electron, as a charged particle orbiting the atomic nucleus generates a current $i = ev/2\pi r$. As a result of the generated current loop, a magnetic dipole is generated perpendicular to the orbit of the electron. The magnetic moment of the dipole generated is equal to $\mu_l = iA$ where A is the area encompassed by the electron orbit and i is the current generated by the motion of the charged electron. The revolution of the electron around the nucleus in a circular fashion (i.e. not the movement of

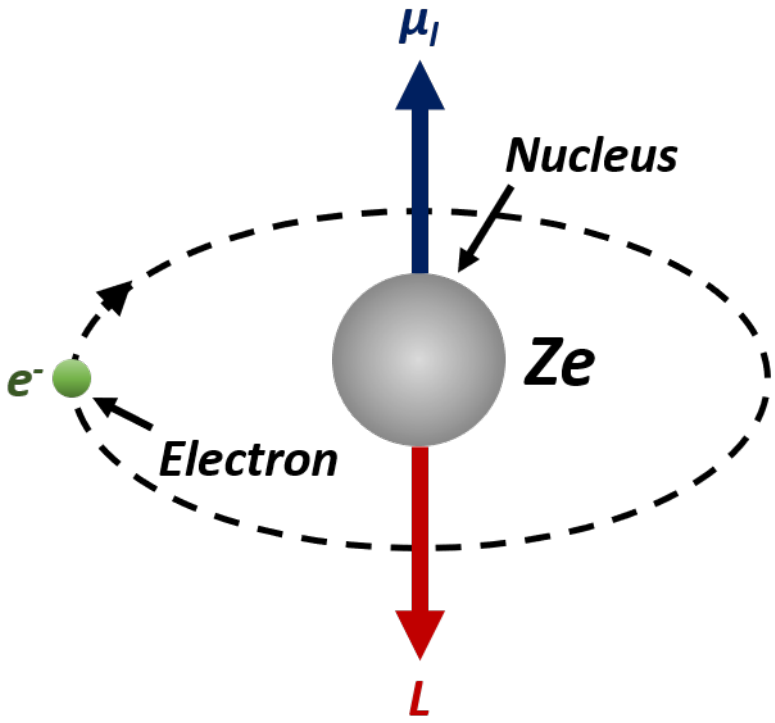

Figure 2.1: Simplified model of an atom with an electron orbiting around the atomic nucleus. The generated magnetic moment $\vec{\mu_l}$ from the orbiting electron lies antiparallel with the angular momentum $\vec{L}$.

a charged particle) also contributes angular momentum $\vec{L}$ with magnitude $L = vrm_e$. The ratio between L and μ_l is given by fundamental constants as shown by equation 2.1.

$$\frac{\mu_l}{L} = \frac{\mu_B}{\hbar} \tag{2.1}$$

Here, μ_B is the Bohr magneton given by

$$\mu_B = \frac{e\hbar}{2m_e} = 0.927 \times 10^{-23}(Am^2) \; or \; (J/T) \tag{2.2}$$

and $\hbar = h/2\pi = 1.054571800(13) \times 10^{-34} Js$ is the reduced Planck's constant.

Equation 2.1 can be rewritten in vector form to provide both the magnitude and direction

of μ_l relative to $\vec{L}$ by

$$\vec{\mu_l} = -\frac{\mu_B}{\hbar}\vec{L} \tag{2.3}$$

where quantum mechanically the magnitude of $\vec{L}$ is given by

$$L = \hbar\sqrt{l(l+1)} \tag{2.4}$$

where l is the orbital angular momentum quantum number taking an integer value between 0 and $n-1$. Here n denotes the principle quantum number and confining the size of the electron's orbit and its energy. As such, the magnetic dipole moment is given by

$$\mu_l = \mu_B\sqrt{l(l+1)} \tag{2.5}$$

and its z component is given by

$$\mu_{lz} = -\mu_B m_l \tag{2.6}$$

where m_l is called the magnetic quantum number taking on allowed integer values of $+l$ and $-l$ respectively. In equation 2.6, the negative sign indicates that the moment and the orbital angular momentum are antiparallel due to the negative charge of the electron. In 1922, O. Stern and W. Geralch determined that electrons possess an intrinsic quantum mechanical spin angular momentum $\vec{S}$ where its magnitude is described by the expression [1]

$$S = \hbar\sqrt{s(s+1)} \tag{2.7}$$

where s is the spin quantum number taking on a value of $1/2$ and with its following z

component given by

$$S_z = \hbar m_s \tag{2.8}$$

where m_s is the spin projection quantum number taking values of $+s$ and $-s$. The magnetic moment generated from the spin angular momentum in vector form is related to direction of the spin angular momentum by the following

$$\vec{\mu_s} = -g_e \mu_B \vec{S} \tag{2.9}$$

where $g_e = 2.002290716(10)2$ is the splitting factor also known as the gyromagnetic factor (g-factor) for a free electron [2]. The z component of the spin moment is then given by

$$\mu_{sz} = -g_e \mu_B m_s \tag{2.10}$$

It is important to note that the experimental observation that an electron deflects in only two directions when propelled in a non-uniform magnetic field leads to the conclusion that μ_{sz} can only take upon two values. This aligns with quantum numbers, as for example, for an electron with $s = 1/2$ it is known that $m_s = \pm s$ corresponding to the "spin-up" and "spin-down" states. The orbital angular momentum and spin angular momentum are coupled together through a spin-orbit interaction known as Russel-Saunder's coupling. If we consider both the spin and orbital angular momenta, we can quantify a value J known as the total angular momentum of an electron. In vector form the total angular momentum of an electron is given by $\vec{J} = \vec{L} + \vec{S}$, following $\vec{L}$ and $\vec{S}$ precessing around $\vec{J}$ as shown in figure 2.2. Similar to the orbital and spin angular momenta, the magnitude of the total angular momentum is described by

$$J = \hbar \sqrt{j(j+1)} \tag{2.11}$$

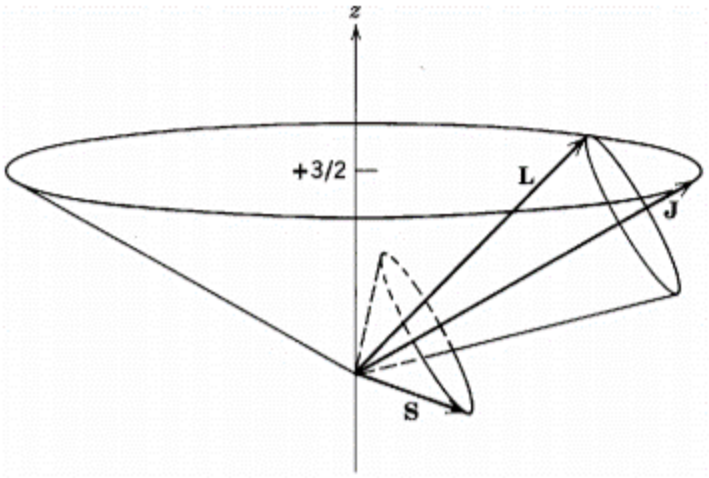

Figure 2.2: The angular momentum vectors, $\vec{L}$, $\vec{S}$, and $\vec{J}$. $\vec{L}$ and $\vec{S}$ precess around $\vec{J}$, where $\vec{J}$ is arises to the spin($\vec{S}$)-orbit($\vec{S}$) coupling with the value of the vector sum of $\vec{J} = \vec{L} + \vec{S}$[3].

where j is the total angular momentum quantum number, where inequalites are used to determine j are given by

$$|\vec{J}| = |\vec{L} + \vec{S}| \geq ||\vec{L}| - |\vec{S}|| \tag{2.12}$$

which then by writing the quantities in terms of the quantum numbers equates to

$$|\sqrt{j(j+1)}h| \geq |\sqrt{l(l+1)}h - \sqrt{s(s+1)}h| \tag{2.13}$$

and for an electron with $s = 1/2$, $j = l + 1/2$ and $j = l - 1/2$ are satisfied for the above. The z component of j is given by

$$J_z = m_j \hbar \tag{2.14}$$

where m_j takes on values between $+j$ and $-j$. Therefore the total magnetic moment in terms of the spin and orbital magnetic moments is given by

$$\vec{\mu} = \mu_B(\vec{L} + 2\vec{S}) \tag{2.15}$$

For a free atom in its ground state, $\vec{L}, \vec{S}$ and $\vec{J}$ can be determined by applying Hund's rules which are as follows [4]:

1) Electrons take on the max value of S without violating the Puali exclusion principle.

2) Maximize the orbital angular momentum L as long as it does not violate rule 1.

3) If an electron shell is less than half-full, J takes its minimum possible value $J = L - S$ as the ground state, but if the shell is more than half-full it takes the form $J = L + S$ as its ground state.

It is important to note that the Russel-Saunders coupling described above applies to lighter atoms with (Z $<$ 30) where the total spin $\vec{S}$ of the group of electrons is coupled with the total angular momentum $\vec{L}$ which results in the total angular momentum $\vec{J}$. In contrast for heavier atoms such as rare-earth elements, the individual spin and orbital angular momenta of the atoms are strongly coupled to the individual total angular momentum for that electron alone. In this case, Russel-Saunders coupling does not accurately describe the electron interactions and L-S coupling must be used where the angular momentum of the individual electrons are summed to determine the total angular momentum J for the atom as follows

$$\vec{J} = \sum_{i=1} \vec{j_i} = \vec{l_i} + \vec{s_i}. \tag{2.16}$$

2.2 Magnetic Ordering

The magnetic ordering of materials is determined by the individual attractive or repulsive forces governed by the magnetic dipole interactions of their atoms. According to the arrangment of their magnetic dipoles in the presence or absence of an externally applied magnetic field, magnetic materials can be classified as diamagnetic, paramagnetic, ferromagnetic, antiferromagnetic, and ferrimagnetic as shown in figure 2.3. Although, many other classifications

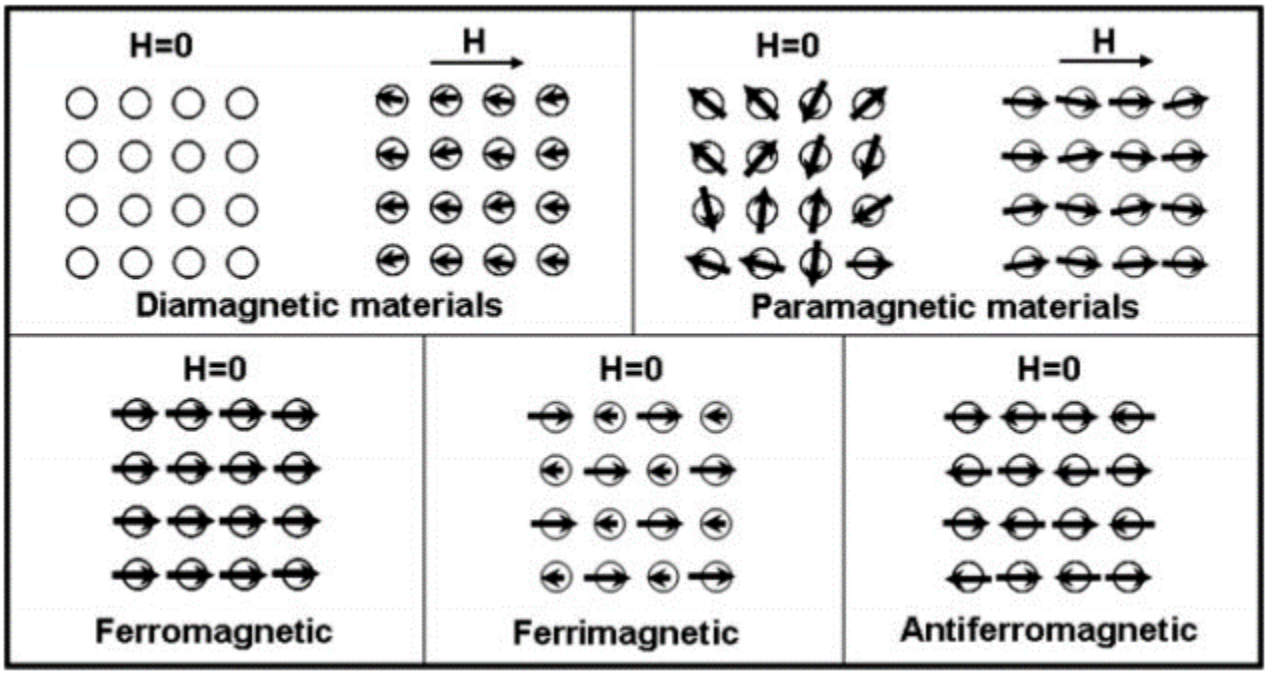

Figure 2.3: The arrangement of the magnetic dipoles in diamagnetic, paramagnetic, ferromagnetic, ferrimagnetic, and antiferromagnetic materials [5]

of magnetic materials have been termed to date, only the few mentioned above are necessary to provide the background for the content in the future chapters.

2.2.1 Diamagnetism

Electrons which possess a closed shell in an atom usually have their spin and orbital moments oriented so that the atom as a whole has no net dipole moment. In other words, diamagnetism is experienced for elements which lack unpaired electrons in their outer orbital shell. Therefore in the periodic table, diamagnetism is experienced for monoatomic gases (i.e. H_2, N_2, etc.). Similar principles apply to ionic solids such as NaCl in which the bonding ionic bonding occurs with the transfer of an electron from Na atoms to the Cl atoms. The resulting ions (i.e. Na^+ and Cl^-) then both possess completely filled electron shells resulting in the overall diamagnetic nature in ionic compounds. Compounds which are covalently bonded in which electrons are shared equally between atoms) are also diamagnetic (i.e. C (diamond),

Si, Ge, etc.) due to the similar filled shell principle.

2.2.2 Paramagnetism

Paramagnetic materials can be explained classically and quantum mechanically. The classical theory of paramagnetism is best described by the Curie Law which demonstrates that the mass susceptibility χ_m varies inversely proportional with the absolute of temperature as follows

$$\chi_m = C/T \tag{2.17}$$

where C is the Curie constant per gram. Later it was proven that the Curie Law is a very special case of the Curie-Weiss law which more accurately portrays the paramagnetic behavior given by

$$\chi_m = \frac{C}{T-\theta} \ , \ (T > \theta > 0) \tag{2.18}$$

where θ is a constant with the units of absolute temperature T. The idea of paramagnetism was first constructed by Langevin, stating that such materials consists of atoms each with the same overall magnetic moment μ in which the spin and orbital moments within individual atoms do not cancel out [6]. However, in the absence of an externally applied magnetic field H, the atomic moments point in different directions so that the net magnetization of the sample is zero. Naturally as H is applied, the magnetic moments of the individual atoms have the tendency to point in the direction of H if there is no counteracting force. However, as substantially large fields are required to align the magnetic moments in the direction of H, an existing thermal agitation force must exist which tends to align the individual moments at random. This results in a partial alignment of the moments with H following a small but positive magnetic susceptibility. By increasing the temperature, the randomizing effects

are enhanced which in turn decrease the susceptibility. To put this into perspective, typical values for paramangetic substances are between $\chi_m = 10^{-5} - 10^{0}$.

Paramagnetism can be understood by quantum mechanics quite easily. In quantum mechanics, the energy of the system is not continuously variable and must exist in discrete states called *quanta*. Comparing the classical model to the quantum mechanical model, for an individual atom the moment can be freely oriented in any particular angle θ classically, whereas quantum mechanically it must take on discrete allowed values of angles (i.e. θ_1, θ_2, etc.). As such, the states with different J_z are degenerate in the absence of H. With the application of H, the degeneracy is removed by the appearance of a magnetic moment in the field with the energy (Zeeman energy):

$$\epsilon_z = -J_z H. \tag{2.19}$$

2.2.3 Ferromagnetism

In contrast to paramagnets, ferromagnets possess much higher magnetic susceptibilities ranging between $\chi_m = 10^{0} - 10^{7}$. As a result, such materials exhibit strong magnetic behavior with large induced magnetization. The reason for the pronounced magnetic behavior is due to the strong atomic moments arising from unpaired electrons in addition to the parallel alignment of those atomic magnetic moments due to parallel aligned magnetic domains in the absence of a magnetic field. The magnetic domains do not always necessarily align completely parallel with one another and form so called domain walls. The magnetic domains align in direction of the applied field by volume variation of the individual domains. The spontaneous magnetization and the proposed mechanism of magnetic domains was first proposed by Weiss by describing an effective molecular field [7]. It was proposed that the molecular field was proportional to the bulk magnetic saturation but failed for ferromagnetic

materials due to their intrinsic domain structure. However, he was not entirely wrong as in this case, the molecular field was proportional to the saturation magnetization at $T = 0K$.

In 1928, W. K. Heisenberg introduced the exchange interaction between neighboring spins, $\vec{S_i}$ and $\vec{S_j}$ which explains the origin of large molecular fields in ferromagnets. The energy of the exchange interaction ϵ_{ex} is the eigenvalue of the Hamiltonian given by

$$\mathcal{H}_{ex} = \mathcal{H}_{ij} = -2J\vec{S_i}\vec{S_j}cos(\phi) \tag{2.20}$$

where J is the exchange integral and should not be confused with the total angular momentum and ϕ is the angle between the two spins. By convention the positive value of J denotes a parallel spin (i.e. ferromagnetic state), whereas a negative value denotes an antiparallel spin (i.e. antiferromagnetic state).

The temperature dependence on the magnetic behavior of ferromagnets can be described through their magnetic susceptibility. These materials possess significantly larger magnetic susceptibilities in comparison to paramgnets due to their stronger magnetic moments and relatively longer range ordering. However, beyond a certain temperature known as the Curie Temperature T_c, these materials begin to behave paramagnetically. Therefore, a ferromagnet's magnetic susceptibility can be described by

$$\chi_m = \frac{C}{T - T_c}. \tag{2.21}$$

The Curie temperature is the absolute limit in which the ferromagnetism holds. As $T = T_c$ is reached the magnetic susceptibility diverges indicating non-zero magnetization in the absence of a magnetic field.

2.2.4 Antiferromagnetism

The fundemental physics of antiferromagnetism was described by Louis Néel in the 1930s earning him a renowned Nobel prize [8]. Antiferromagnets can be viewed as two ferromangetic sublattices which oppose each other such that the magnetic moments completely cancel each other. Similar to ferromagnetic materials, the antiferromagnetic ordering is governed by the exchange interaction for negative values of J. As such, these materials consist of antiparallel spins which result in an overall net zero magnetization as the moments completely cancel each other out. However, a very small magnetization may appear for canted/disordered antiferromagnets or polycrystalline antiferromagnetic specimens which are comprised of pinned moments due to grain boundaries. These materials possess small magnetic susceptibility on the order of $\chi_m = 10^{-5} - 10^{-2}$ similar to that of paramagnetism, with their difference being an ordered magnetism exists in antiferromagnets. However, the susceptibility of antiferromagnets increases with increasing temperature reaching a maximum value at the Néel temperature T_N. Similar to ferromagnets, above T_N the antiferromagnetic ordering is lost and paramagnetic ordering prevails following the Curie-Weiss law.

2.2.5 Ferrimagnetism

Ferrimagnets are an interesting class of magnetic materials which consist of two or more sublattices with an antiparallel configuration that do not completely cancel. This occurs as the magnetic moments of the sublattices are not similar in magnitude but oppose each other. These magnetic materials possess specific characteristics and properties from both ferromagnetic and antiferromangetic materials. To put this into perspective, J in ferrimagnets must be positive as they possess a spontaneous net moment, in contrast to antiferromagnets. However, values of J in ferrimagnets are substantially smaller than the values found for ferromagnets. In addition, ferrimagnets follow the similar increase in susceptibility as

antiferrimagnets. The magnetic susceptibility of ferrimagnets increases with temperature, becoming paramagnetic beyond T_N.

2.3 Magnetization & Magnetic Hysteresis Curves

The study of the magnetic hysteresis loops in all classes of magnetic materials provides insightful information on its material properties. Typically, hysteresis loops are commonly studied for ferro and ferrimagnetic materials. As a result, this section shall begin with the introduction of the hysteresis loop for an ideal ferro/ferrimagnet as shown in figure 2.4. The hysteresis loop describes the magnetic flux density of an already pre-magnetized material as a function of the applied field H denoted by B which is equal to

$$B(H) = \mu_0[H + M(H)] \tag{2.22}$$

where $\mu_0 = 1.25663706 \times 10^{-7}(H/m)$ is the permeability of free space $M(H)$ is the magnetization of the material as a function of H. In the B curve, B_m is the saturation induction, and B_r is the remanence describing the value of B when the applied field H is removed. Another important parameter is the coercive field H_c, which describes the magnitude of the applied field to coerce the material back to zero induction (i.e. demagnetize the material). Now that the B hysteresis loop is understood, the relationship between B and H can be investigated. The permeability of a magnetic sample μ is given by the slope of the BH curve as such

$$\mu = \frac{B}{H} \tag{2.23}$$

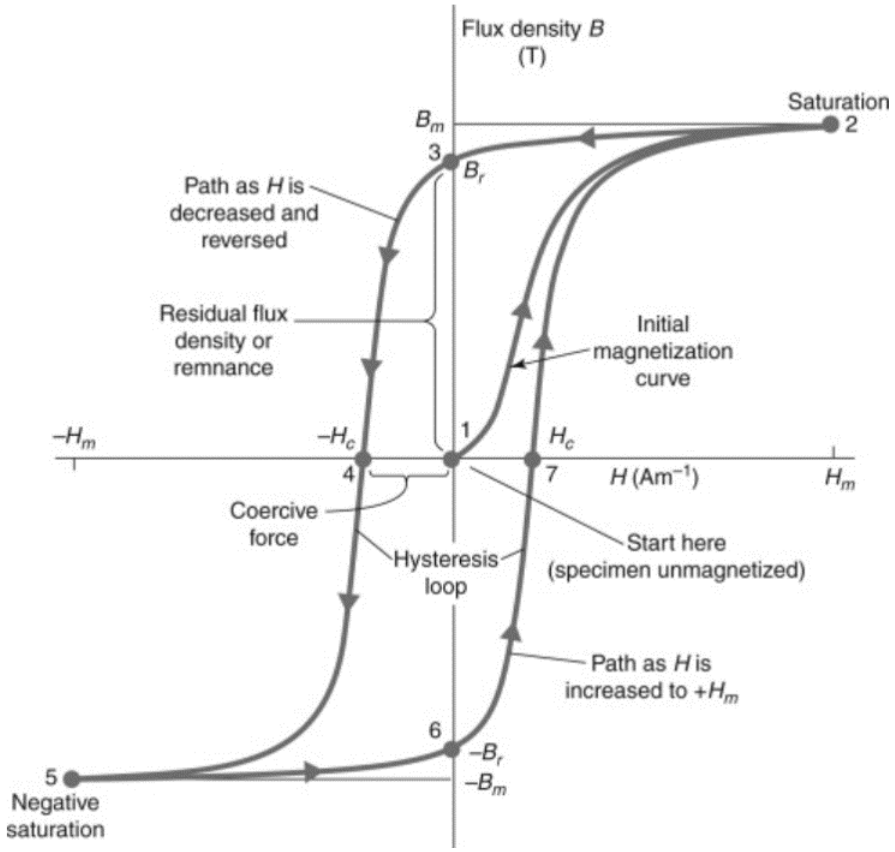

Figure 2.4: Magnetization and hysteresis loop of an ideal ferro/ferri magnet. [9].

which can be rewritten in terms of the materials relative permeability μ_r as

$$\mu_r = \frac{\mu}{\mu_0} = \frac{B}{\mu_0 H} \tag{2.24}$$

which is dimensionless similar to μ.

In figure 2.4, the inner curve represents the materials virgin magnetization curve. This describes the magnetization of a ferro/ferrimagnetic material which has not been magnetized. Here, M_s represents the materials saturation magnetization where the maximum value for the magnetic moment is measured and is equal to B_m. It is important to note that once the material has been magnetized once, the magnetic hysteresis curve will then begin to behave similar to the outer loop. Most notably, the inner curve describing the virgin magnetization begins from a near zero value in both the magnetization and applied field (origin of the BH

axis). However, the induced magnetization B will never full return to that position once the material has been exposed to a saturating magnetic field H_m. As such, the magnetization curve MH can provide insightful information on the material's susceptibility as such

$$\chi = \frac{M}{H} \tag{2.25}$$

where χ is the susceptibility and M is the magnetization of the material as a function of the applied field H. various forms of the susceptibility such as the mass, atomic, volume, and molar susceptibilities are used which depends on the units in which the magnetization M where measured. For instance as the mass susceptibility was used extensively in the previous section, the mass susceptibility can be given by χ_m

$$\chi_m(\frac{emu}{Oe \cdot g}) = \frac{M(emu/cm^3)}{H(Oe)}\rho(g/cm^3) \tag{2.26}$$

where ρ is the density of the magnetic material. The mass susceptibility χ_m and the relative permeability μ_r can be related to each other by combining equations 2.24 and 2.25 as

$$\mu_r = \mu_0(1 + \chi_m) \tag{2.27}$$

In general, for the various classes of magnetic materials described in the previous section, the permeability and susceptibility can be generalized as shown in table 2.1.

Type	$\boldsymbol{\mu}$	$\boldsymbol{\chi}$
Free Space	1	0
Diamagnets	$\mu < 1$	small & $\chi < 0$
Ferro & Ferrimagnets	large & $\mu \gg 1$	large & $\chi \gg 1$
Para & Antiferromagnets	$\mu > 1$	small & $\chi > 0$

Table 2.1: The generalization of the permeability and susceptibility of free space, diamagnets, ferro & ferrimagnets, and para & antiferromagnets.

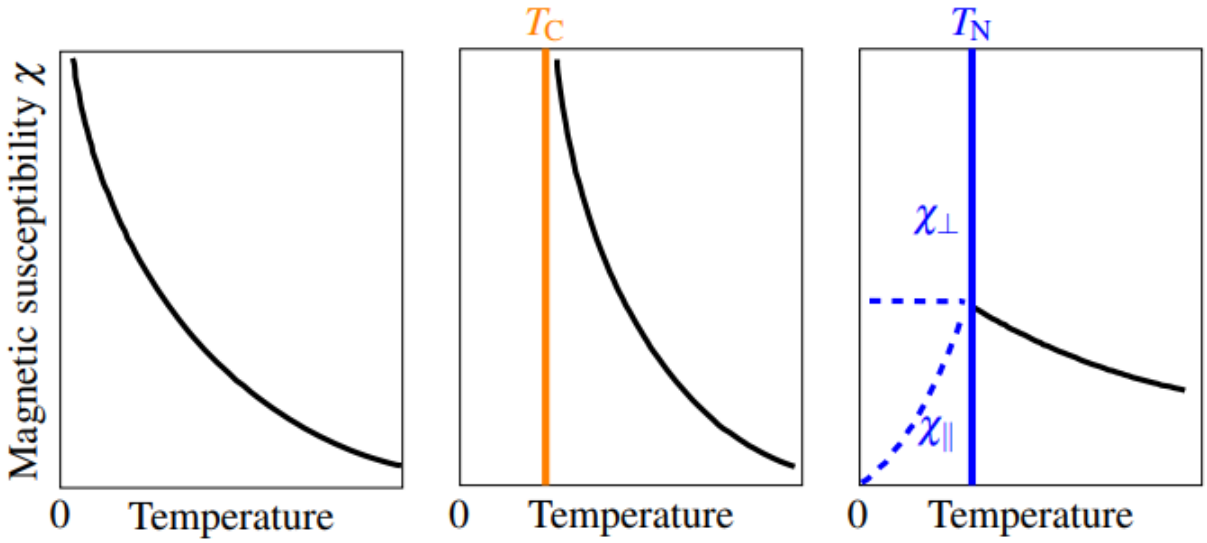

Figure 2.5: From left to right, the magnetic susceptibility shown as a function of temperature for a paramagnet, ferromagnet, and antiferromagnet [10].

As discussed earlier, paramagnets and antiferromagnets have similar hysteresis curves with relatively small but positive magnetic permeability μ and susceptibility χ.

2.4 Magnetic Anisotropy

Anisotropy is derived from the Greek words *Anisos* "unequal", and *tropos* meaning "turn". As described earlier, magnetic dipoles which give rise to magnetism are intrinsically directional. Therefore, as all magnetic materials are comprised of many magnetic dipoles oriented in various configurations, there must be a preferred orientation in some materials which is governed by the so called magnetic anisotropy. The importance of magnetic anisotropy in the design of many magnetic commercial devices employing ferro and ferrimagnetic materials is of significant importance as represented by the coercive field of magnetic materials. This is because magnetic properties in magnetic materials possess different characteristics in various directions arising from the intrinsic magnetic anisotropy. Therefore, to fundamentally understand the magnetic behavior completely in ferro and ferrimagnetic materials, a

thorough understanding of magnetic anisotropy is required. The most significant sources of magnetic anisotropy shall be explained here which are the magnetocrystalline (MCA), the magnetoelastic anisotropy (MEA), elastic anisotropy, and the shape anisotropy which is also referred to as the demagnetizing field (demag for short), the zeeman energy, and last the energy arising from the exchange interaction. Therefore, the total energy of a magnetic system E_T can be written as

$$E_T = E_{MCA} + E_{MEA} + E_{ex} + E_{demag} + E_{zeeman}\ (J/m^3) \tag{2.28}$$

where E_{MCA} is the energy from the MCA, E_{MEA} is the energy from the MEA, E_{el} is energy from the elastic anisotropy, and E_{Demag} is the energy from the shape anisotropy, E_{zeeman} is the zeeman energy, and E_{ex} is the energy due to the exchange interaction. It is important to note that the exchange interaction is completely isotropic and does not contribute to the overall anisotropy. Therefore, the total anisotropic energy in a magnetic system can be rewritten as

$$E_{an} = E_{MCA} + E_{MEA} + E_{el} + E_{demag} + E_{zeeman}\ (J/m^3) \tag{2.29}$$

The total anisotropy E_{an} is related to the coercive field H_c and saturation magnetization M_s of the magnetic material by

$$E_{an} = M_s H_c. \tag{2.30}$$

Equations 2.29 and 2.30 will be very important in the findings presented in the future sections. Below, the origin of the individual contributions to the total magnetic anisotropy shall be explained.

2.4.1 Magnetocrystalline Anisotropy

The magnetocrystalline anisotropy (MCA) is the only source of anisotropy intrinsic to a material, as it originates from the spin-orbit coupling [11]. One would believe the origin of the MCA would be due to the exchange interaction of two neighboring spins controlling their parallel or antiparallel alignment. However, the exchange interaction is strong but completely isotropic as it only depends on the angle between the two as show in in equation 2.20. To understand how the MCA originates from spin-orbit coupling, the interaction energies between the spin, orbit, and lattice must be compared to each other as shown in figure 2.6. The spin-orbit coupling is strong but relatively weak compared to the strength of the orbit with the lattice, as the orbital moments are quenched. The quenched orbits cause their orientations to become fixed very strongly to the lattice and the application of very large fields do not reorient them.

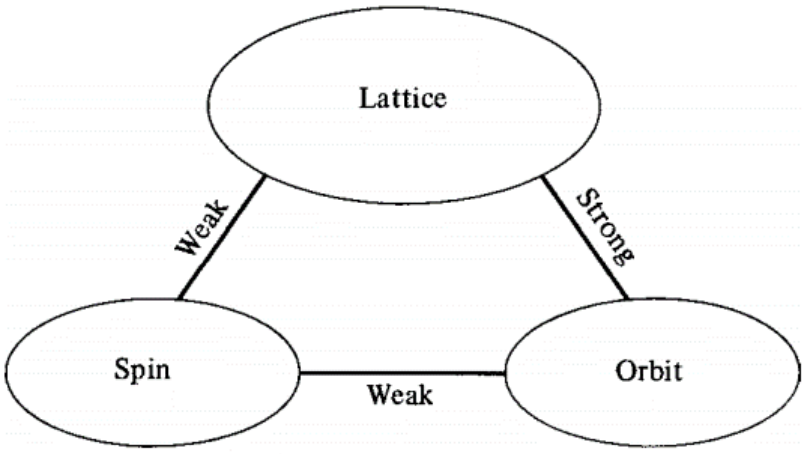

Figure 2.6: The strength of the interactions between the spin, orbit, and lattice [11]

Now consider the interaction of the spin and the orbital motion of the electrons together. The application of a magnetic field tends to reorient the electron and the orbit of the electron also tends to become reoriented. However, the orbit is strongly coupled with the lattice resisting any attempts to become reoriented. Therefore, the energy required to overcome the spin-

orbit coupling which in turn will rotate the entire spin-system is the MCA. The magnitude of the MCA energy decreases more rapidly than the magnetization as temperatures are increased, vanishing at the curie point. The energy of the MCA E_{MCA} naturally depends on the crystal structure of the magnetic material. However, two important equations for E_{MCA} have been developed which accurately describe the energy in all crystal systems which are divided into the cubic anisotropy and the uniaxial anistropy.

MCA in Cubic Crystals

E_{MCA} for cubic crystals approximated to the 6^{th} order given by

$$E_{MCA}^{Cubic} = K_0 + K_1(\alpha_1^2 + \alpha_2^2 + \alpha_3^2) + K_2(\alpha_1^2\alpha_2^2\alpha_3^2) \tag{2.31}$$

where K_1 and K_2 are the magnetocrystalline aniostropy constants and vary for each material system, and α_1, α_2, and α_3 are the directional cosine terms with respect to the direction of magnetization vector $\vec{M}_s$.

Each cubic crystal system has its own easy and hard direction. To put this into perspective, BCC iron has the easy axis in the <100> and hard axis in the <111> directions as shown in figure 2.7. The magnetocystalline anisotropy constants play an important role in determining the preferred crystallographic orientation of the MCA. As shown in figure 2.9a for iron, $K_1 > K_2$ where the dominant K_1 approximating the 4^{th} term is positive resulting in $< 100 >$ as the easy axis in BCC systems. However, nickel crystallizes in FCC which has the preferred easy axis along the <111> direction and hard axis along <100> as shown in figure 2.8. As shown in figure 2.9a for nickel, $K_1 < K_2$ where the dominant K_1 approximating the 4^{th} term is negative resulting in <111> as the easy axis in FCC systems.

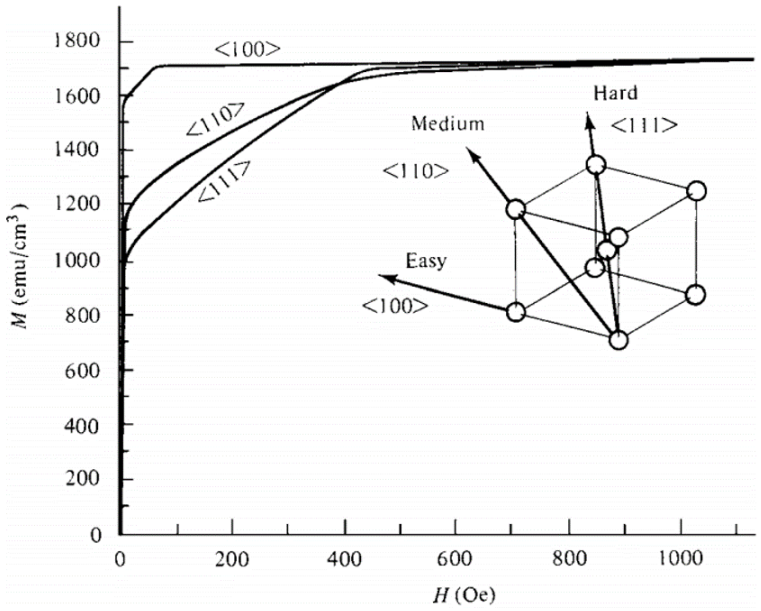

Figure 2.7: Magnetization curve for single crystal BCC iron,where he easy axis of magnetization lies along the $< 100 >$ crystallographic direction [11].

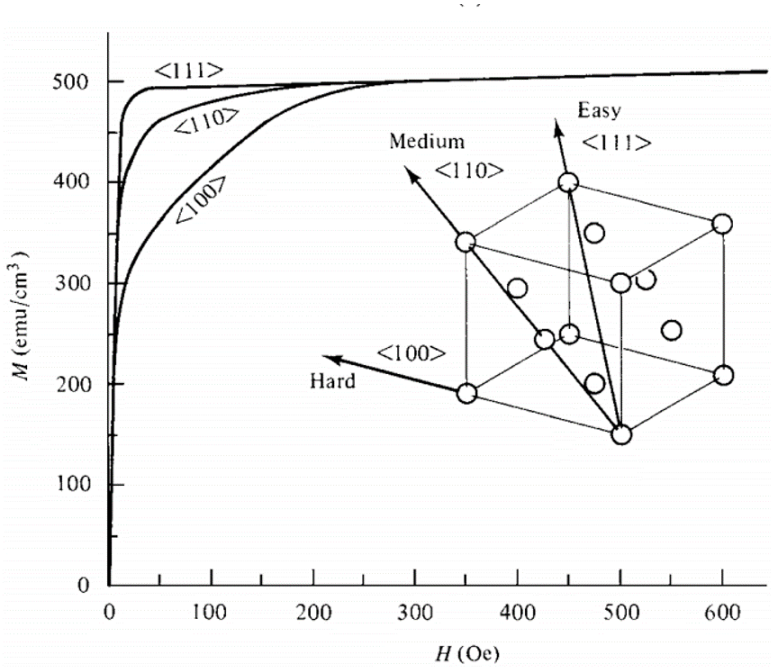

Figure 2.8: Magnetization curve for single crystal FCC Nickel, where the easy axis of magnetization lies along the $< 111 >$ crystallographic direction [11].

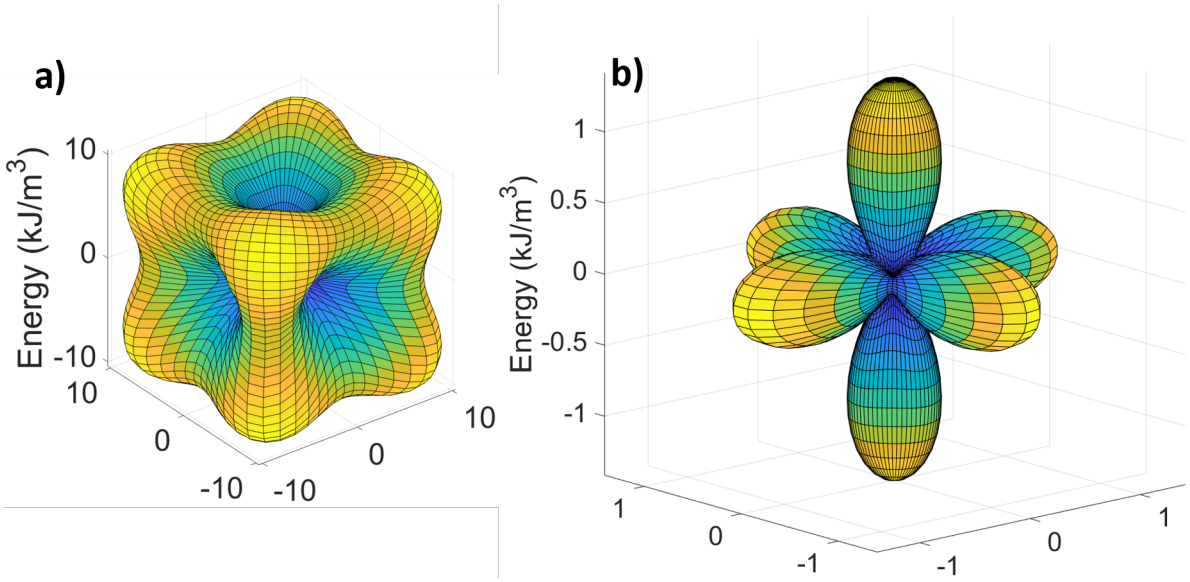

Figure 2.9: Surface energy plots of the MCA energy in a) BCC iron for $K_1 > K_2$ b) FCC nickel where $K_1 < K_2$.

MCA in Uniaxial Crystals

Uniaxial crystals contain one crystallographic axis that is physically substantially longer than other crystallographic axes. These crystals systems are hexagonal, tetragonal, and trigonal crystal structures where the c-axis is noted as the much longer axis, hence the term uniaxial crystal. As such, the E_{MCA} for uniaxial crystals approximated to the 4^{th} is given by

$$E_{MCA} = K_0 + K_1 sin^2(\theta) + K_2 sin^4(\theta) \tag{2.32}$$

where θ is the angle between the magnetization vector $\vec{M}_s$ and the crystallographic c-axis (the easy axis of magnetization), and K_1 and K_2 are the magnetocrystalline anisotropy constants unique for each magnetic material. Similar to the cubic magnetocrystalline anisotropy constants, the K_1 and K_2 terms dictate the orientation of the magnetization.

If both K_1 and K_2 are positive, the $\vec{M}_s$ falls along the c-axis where the minimum energy is found for $\theta = 0^o$. If both K_1 and K_2 are negative, $\vec{M}_s$ lies along a basal plane perpendicular

to the c-axis where the minimum energy is found for $\theta = 90^o$. If K_1 and K_2 have opposing signs, the situation is much more complex as shown in figure 2.10. If K_1 is positive and K_2 is negative, the line $K_2 = -K_1$ is the boundary between the magnetization lying in the basal plane or the c-axis. In this case if $K_1 = -K_2$, there are two easy direction lying at 0^o and 90^o. Now if K_1 is negative and K_2 is positive, the limit of the easy-plane behavior follows $K_2 < \frac{-1}{2}K_1$ where in this range the minimum E_{MCA} lies between the angles of $0 - 90^o$ and there is an *easy cone* of magnetization in this state.

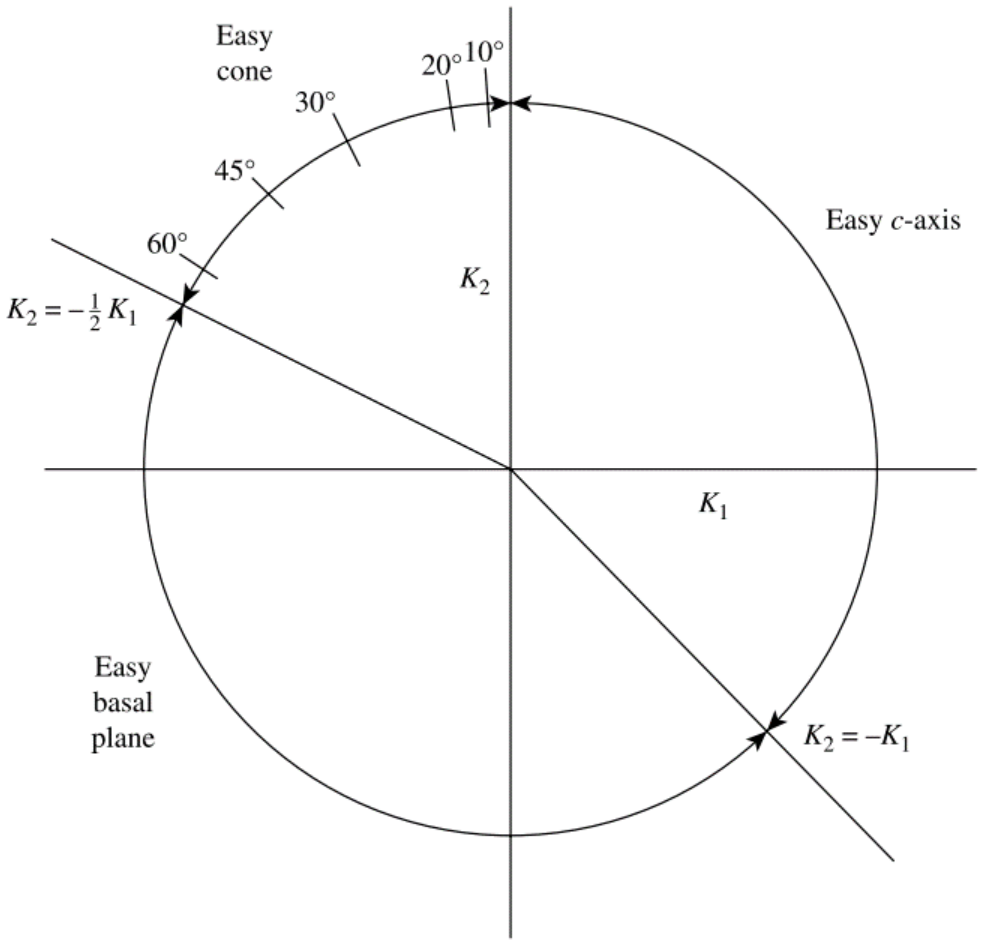

Figure 2.10: Easy directions and planes in uniaxial crystals for all possible values of K1 and K2. [11]

2.4.2 Magnetoelastic Anisotropy

The magnetoelastic anisotropy (MEA) arises due to the effect of stresses (or strains) which alter the magnetic domain structure. Similar to the MCA, the MEA originates from the modulation of the spin-orbit coupling which in turn controls the magnetic domains [12]. To put this into perspective, any mechanical strain directly effects the crystal lattice where modification to the spin-orbit coupling occurs [13]. In addition, MEA is defined for both cubic and uniaxial crystals similar to the MCA which will both be discussed below.

MEA in Cubic Crystals

The cubic MCA energy term to the 4^{th} order is given by

$$E_{MEA}^{cubic} = B_1(\epsilon_1\alpha_1^2 + \epsilon_2\alpha_2^2 + \epsilon_3\alpha_2^2) + 2B_2(\epsilon_4\alpha_2\alpha_3 + \epsilon_5\alpha_1\alpha_3 + \epsilon_6\alpha_1\alpha_2) \tag{2.33}$$

where α_i are the directional cosine terms with respect to the magnetization vector $\vec{M}_s$, ϵ_i are the strains measured along the crystallographic directions, and B_1 and B_2 are the magnetoelastic coupling coefficients. B_1 and B_2 are given by

$$B_1 = -\frac{3}{2}(c_{11} - c_{12})\lambda_{100} \ , \quad B_2 = -3c_{44}\lambda_{111} \tag{2.34}$$

where c_{11} and c_{12} are the elastic constants, and λ_{100} are the magnetostriction constants λ_{111}. As one would expect, the MEA and magnetostriction are one where the former is the energy and the later describes the physical effect. Therefore, it is clear that without understanding the physical origin of MEA, it is near impossible to fully comprehend the physical origin of magnetostriction which shall be reviewed in more detail in section 2.4. As such, the significant importance of magnetic anisotropy can be clearly highlighted here where magnetostriction (MEA) driving many of today's devices in industry could not exist

without magnetic anisotropy.

Equation 2.35 can be written in terms of the magnetostriction constants as

$$E_{MCA}^{cubic} = -\frac{3}{2}\lambda_{100}\sigma(\alpha_1^2\gamma_1^2 + \alpha_2^2\gamma_2^2 + \alpha_3^2\gamma_3^2) - 3\lambda_{111}\sigma(\alpha_1\alpha_2\gamma_1\gamma_2 + \alpha_2\alpha_3\gamma_2\gamma_3 + \alpha_1\alpha_3\gamma_1\gamma_3) \quad (2.35)$$

where σ is the magnitude of the stress vector ($\sigma = |\vec{\sigma}|$), and γ_i are the directional cosine terms with respect to the stress vector $\vec{\sigma}$. Equation 2.35 represents the MEA for a single crystal magnetic sample. However, magnetic materials today are largely polycrystalline. As such, equation 2.35 can be simplified for a polycrystals assuming $\lambda_{100} = \lambda 111 = \lambda_{si}$

$$E_{MCA,si}^{cubic} = \frac{3}{2}\lambda_{si}\sigma sin^2(\theta) \quad (2.36)$$

where θ is the angle between the magnetization vector $\vec{M}_s$ and the stress vector $\vec{\sigma}$.

MEA in Uniaxial Crystals

The MEA in uniaxial crystals is similar to that of the polycrystalline cubic materials in equation 2.36. However, for uniaxial crystals it can be rewritten

$$E_{MCA}^{uniaxial} = K_\sigma sin^2(\theta) \quad (2.37)$$

where K_σ is the stress anisotropy constant given by $K_\sigma = \frac{3}{2}\lambda_{si}\sigma$. By writing the equation in this manner, the axis of stress is the easy axis of K_σ is positive, and the easy axis lies in a plane perpendicular to the axis of stress if K_σ is negative.

2.4.3 Elastic Anisotropy

The elastic energy is also an important factor which adds to the magnetic anisotropy. The elastic energy can be described as the potential energy stored in the material as it is subjected to plastic deformation by a force/work performed on it. The elastic energy in bulk materials can be transfered in various wasy such as stretching, shearing , bending, twisting, etc. which all in various ways aid to the elastic energy of the distorted material. As such, the elastic energy can be described for all crystals by

$$E_{el} = \frac{1}{2} C_{ijkl} \epsilon_{ij} \epsilon_{kl} \tag{2.38}$$

where C_{ijkl} is the 4^{th} order elastic/stiffness tensor, and ϵ_{ij} and ϵkl are the strain tensors. For a material with cubic symmetry the elastic energy is written as

$$E_{el} = \frac{1}{2} c_{11}(\epsilon_1^2 + \epsilon_2^2 + \epsilon_3^2) + \frac{1}{2} c_{12}(\epsilon_1\epsilon_2 + \epsilon_2\epsilon_3 + \epsilon_1\epsilon_3) + \frac{1}{2} c_{44}(\epsilon_4^2 + \epsilon_5^2 + \epsilon_5^2). \tag{2.39}$$

2.4.4 Shape Anisotropy

Shape anisotropy are interchangeably used to describe the same physical phenomena. As magnetic materials have magnetic domains oriented in the same direction, magnetic "free poles" appear on the surface of the material due to a discontinuous change in the magnetization perpendicular to the surface. As a result, a large demagnetizing field followed by large magnetostatic energy are produced. In addition, this causes the formation of magnetic domains in materials, as domains are formed to minimize these demagnetizing fields by balancing the exchange energy with the magnetostatic energy. The energy term for the

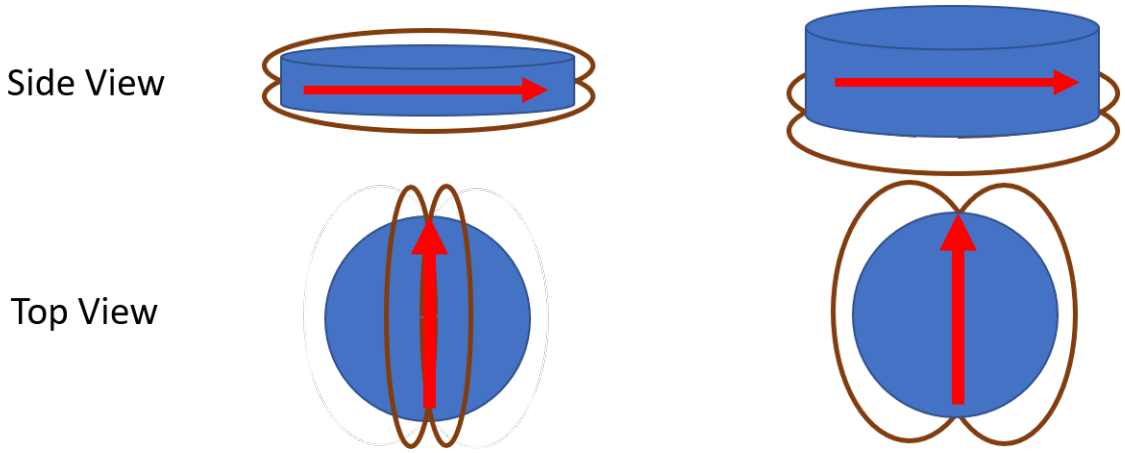

Figure 2.11: Demagnetizing field for two circular disks with in-plane magnetization. The disk on the left is thinner and has a demagnetizing field going through the top and the bottom of the disk. The disk on the right is thicker and the demagnetizing field goes around the disk to minimize its energy.

demagnetization energy can thus be written as

$$E_{demag} = \frac{1}{2}\mu_0(N \cdot \vec{M}_s) \cdot \vec{M}_s \tag{2.40}$$

where it can be written for a general ellipsoid as

$$E_{demag}^{ellip} = \frac{1}{2}\mu_0 M_s^2(N_1\alpha_1^2 + N_2\alpha_2^2 + N_3\alpha_1^2) \tag{2.41}$$

where N is the 2^{nd} order demagnetization tensor and α_i are the directional cosine terms with respect to the magnetization vector $\vec{M}_s$ [14]

The shape anisotropy is naturally dependent on the geometric shape of the magnetic material. The shape anisotropy in a constant attempt to be at a minimum. Figure 2.11 shows the top and side view of two circular disks with similar radii but varying thicknesses where the brown lines represent the demagnetization field of each disk. The demagnetization field shown in the left thinner disk minimizes by preferring to pass over and under the disk rather than going across the sides. However, for the the thicker disk shown on the left, the demagnetization field prefers to go around the disk to minimize its energy. The shape anisotropy also governs

the domain structure as naturally domains are a way of minimizing the demagnetization field. As such, by micropatterning various shaped magnetic structures (i.e. disks) single domain or multi-domain states can generated in magnetic structures.

2.4.5 Zeeman Energy

The Zeeman energy is the energy introduced to the system in response to an externally applied magnetic field. It is a form of potential energy of continuous magnetic moments when subjected to an applied magnetic field given by

$$E_{zeeman} = \mu_0 \int_V M \cdot H dV \tag{2.42}$$

where V represents the volume of the body, μ_0 is the permeability of free space, M is the magnetization, and H is the externally applied magnetic field.

2.5 Magnetostriction

When a magnetic material is subjected to an externally applied magnetic field its dimensions changes, termed magnetostriction. It was found by Joule in 1842 who witnessed a change in the dimensions of an iron rod by applying a weak magnetic field lengthwise to an iron rod [15]. The fractional change of in length $\lambda = \Delta l/l$ is naturally a strain which can be distinuished from an applied strain ϵ as a result of stress σ by defining

$$\lambda = \frac{\Delta l}{l} \tag{2.43}$$

where λ is the unit-less magnetostriction term and l and Δl represent the length and the change in the length respectively. The value of λ measured at the saturation magnetization

M_s is termed the saturation magnetostriction denoted by λ_s as shown in figure 2.12.

As the magnetostrictive effect is rooted from the magnetoelastic anisotropy (MEA), therefore it also originates from spin-orbit coupling. As such, the magnetostrictive effect occurs by domain wall motion [16]. Magnetostriction is not prominently seen in many magnetic materials, in which values of λ_s are roughly on the order of 10^{-5}. However, as a result of inverse magnetostrictive effects such as the application of various external stresses, alter magnetic properties such as the permeability μ and the coercive field H_c. In turn, this effects the size and shape of the magnetic hysteresis loop, which is very useful for magnetic devices utilizing highly magnetostrictive materials.

Two types of magnetostriction occur, spontaneous magnetostriction and forced magnetostriction. Spontaneous magnetostriction occurs when a material is heated beyond its Curie temperature T_c and then cooled to below it. Forced magnetostriction occurs when a sample is subjected to an externally applied magnetic field large enough to increase the magnetization of the domain above its spontaneous value. Both types of magnetostriction increase the spin-order in the system.

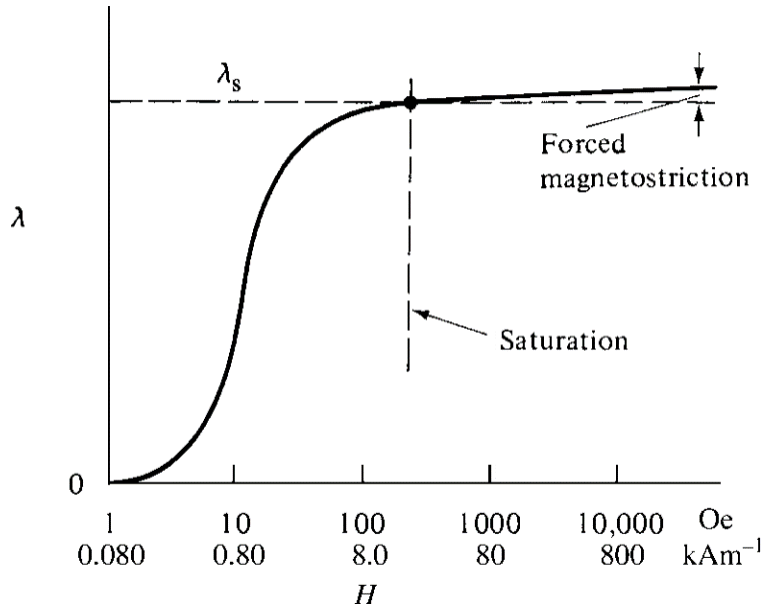

Figure 2.12: Magnetostriction as a function of the applied field [11].

2.5.1 Magnetostriction in Single Crystals

Measurement of the magnetostriction coefficients λ_{100} and λ_{111} for various magentostrictive materials are of significantly importance to the scientific community in particular for those who utilize these values in micromagnetic models. Figure 2.13 shows the measurement of magnetostriction in single crystal iron in the [100] direction. In figure 2.13a, the multi-domain structure is clearly seen in the single crystal iron sample. In figure 2.13b, although an exaggeration of the magnetostrictive effect is presented, it is clearly evident that the majority of the domains have rotated to the direction of the applied field. As the domains which were originally oriented along the [010] direction rotate by domain wall motion, the domain must expand in the [100] direction and contract in the [010] direction resulting in the elongation of the crystal Δl. As such, the measured difference in the length shown by Δl is used to determine λ_{100} for iron in this example. Through a similar approach in the [111] direction, λ_{111} can also be determined.

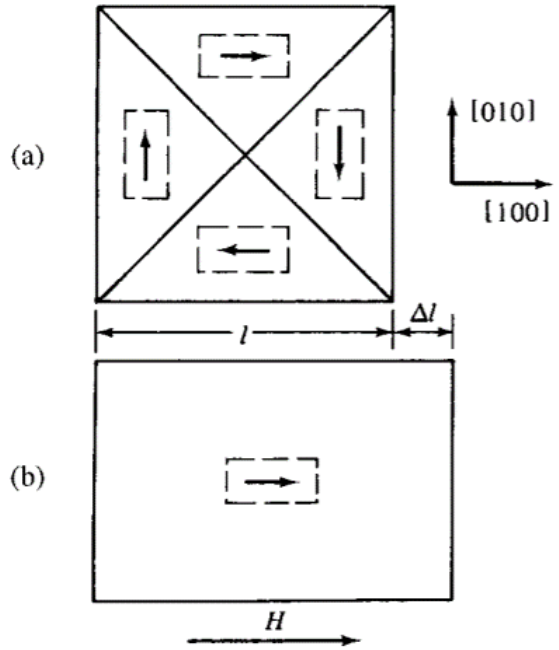

Figure 2.13: Measurement of the magnetostriction in single crystal iron in the [100] direction [11].

2.5.2 Saturation Magnetostriction in Cubic Crystals

It is a common misconception that the cubic crystals which undergo magnetostriction are completely cubic, as this is the case only when the material is at a temperature above T_c [17]. However, the tetragonality is fairly small and the crystals can be assumed to be pseudo-cubic. As such, the saturation magnetostriction term for these crystals can be written as

$$\lambda_s = \lambda_{100} + 3(\lambda_{111} - \lambda_{100})(\alpha_1^2\alpha_2^2 + \alpha_2^2\alpha_3^2 + \alpha_1^2\alpha_3^2) \tag{2.44}$$

2.6 Summary

This chapter aims to provide a brief understanding of the fundamental principles of magnetic materials and their properties which will be extensively covered in detail in the next chapters. The origin of magnetism is necessary to understand the content in Chapter 3 where the interaction of X-rays with the spin and orbital magnetic moments are explained. The magnetic ordering of magnetic materials are necessary to comprehend the various dynamics and properties intrinsic to each class of magnetism, in particular ferri and antiferromagnets for this dissertation. Without the comprehension of magnetic anisotropy, most of the applications employing magnetic materials cannot be practically understood. Evidently, it is critical to provide an extensive background on magnetic anisotropy, as its manipulation leads to the majority of today's working magnetic devices. And the last section covers magnetostriction, an intrinsic property of all magnetic materials. Coupling magnetostrictive materials with piezoelectric ones has lead to the development of the field of multiferroics which represents the future of efficient magnetic based devices.

Chapter References

[1] Walther Gerlach and Otto Stern. Der experimentelle nachweis der richtungsquantelung im magnetfeld. In *Walther Gerlach (1889–1979)*, pages 26–29. Springer, 1989.

[2] KHJ Buschow and FR de Boer. Magnetostrictive materials. In *Physics of Magnetism and Magnetic Materials*, pages 171–175. Springer, 2003.

[3] Robert Eisberg and Robert Resnick. *Quantum physics of atoms, molecules, solids, nuclei, and particles*. 1985.

[4] David J Griffiths and Darrell F Schroeter. *Introduction to quantum mechanics*. Cambridge University Press, 2018.

[5] Unyong Jeong, Xiaowei Teng, Yong Wang, Hong Yang, and Younan Xia. Superparamagnetic colloids: controlled synthesis and niche applications. *Advanced Materials*, 19(1):33–60, 2007.

[6] Willie Sucksmith and RR Pearce. The paramagnetism of the ferromagnetic elements. *Proceedings of the Royal Society of London. Series A. Mathematical and Physical Sciences*, 167(929):189–204, 1938.

[7] Pierre Weiss. L'hypothèse du champ moléculaire et la propriété ferromagnétique. 1907.

[8] Louis Néel. Magnetism and local molecular field. *Science*, 174(4013):985–992, 1971.

[9] ML Wang and G Wang. Electromagnetic sensors for assessing and monitoring civil infrastructures. In *Sensor Technologies for Civil Infrastructures*, pages 238–264. Elsevier, 2014.

[10] Azize Koç. Ultrafast x-ray studies on the non-equilibrium of the magnetic and phononic system in heavy rare-earths. 2018.

[11] Bernard Dennis Cullity and Chad D Graham. *Introduction to magnetic materials*. John Wiley & Sons, 2011.

[12] Charles Kittel, Paul McEuen, and Paul McEuen. *Introduction to solid state physics*, volume 8. Wiley New York, 1996.

[13] Earl R Callen and Herbert B Callen. Static magnetoelastic coupling in cubic crystals. *Physical Review*, 129(2):578, 1963.

[14] Richard M Bozorth. Ferromagnetism, chap. 18, 1951.

[15] James Prescott Joule. Xvii. on the effects of magnetism upon the dimensions of iron and steel bars. *The London, Edinburgh, and Dublin Philosophical Magazine and Journal of Science*, 30(199):76–87, 1847.

[16] E du Tremolet de Lacheisserie. Magnetoelastic properties of amorphous alloys. *Journal of Magnetism and Magnetic Materials*, 25(3):251–270, 1982.

[17] Richard D James and Manfred Wuttig. Magnetostriction of martensite. *Philosophical magazine A*, 77(5):1273–1299, 1998.

Chapter 3

X-Ray Absorption (XAS) and Magnetism

This section will review the basics of X-Ray absorption (XAS) and how it can be utilized to probe the magnetism of materials on an elemental basis. This is typically achieved by the dichroic response in magnetic materials when exposed to polarized X-Rays (i.e. circularly and linearly polarized) in conjunction with an applied field. Circularly polarized X-Rays are utilized to probe the magnetic response of elements with a spontaneous net moment. This technique is referred to as X-Ray Magnetic Circular Dichroism (XMCD). On the other hand, the magnetic response of atomic elements which couple antiparallely are studied by X-Rays with linear polarization by a method called X-Ray magnetic linear dichroism (XMLD). Both XMCD and XMLD are derivatives of XAS and have become exceptionally important tools for investigating the magnetic responses of individual atomic elements in complex magnetic systems. To understand the physical operating principles of XMCD and XMLD, the theory of XAS must be introduced first.

3.1 X-Ray Absorption Spectroscopy (XAS)

X-Rays are electromagnetic radiation (i.e. light) with wavelengths ranging between 0.01-100 Å. As such, all materials will absorb certain energies of X-Ray radiation when exposed to white-light (non-monochromatic) X-Rays. Figure 3.1 shows a thin film of material with thickness $z < 1000$ Åin transmission mode. Upon introduction of the sample to the incident X-Ray beam I_0, the transmitted beam $I(z)$ is attenuated with a linear absorption coefficient $\mu(E)$ [1] given by equation 3.1.

$$I_z = I_0 e^{-\mu(E)z} \tag{3.1}$$

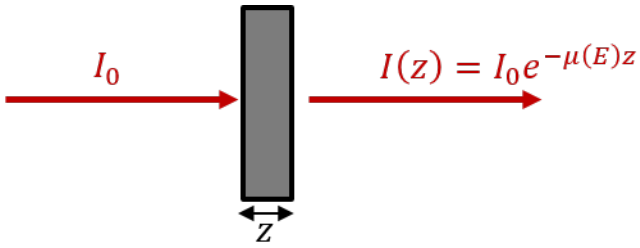

Figure 3.1: Absorbance of X-Rays through a thin film of thickness z in transmission mode.

The attenuation of X-Rays is due to absorption and scattering processes that occur once they enter material mediums. Each substance has a characteristic length λ which is inversely related to the linear absorption coefficient as $\mu(E) = 1/\lambda$. The interaction of X-Rays with the charged particles such as electrons, results in their oscillation due to the electric field contribution of the electromagnetic wave (i.e. X-Rays). This oscillation is heightened at certain energies called the absorption edges as the time-dependent field causes a sharp energy rise between the transitions between the initial and final states. The absorption edge energies are determined by the binding energy of the core-level electrons which these transitions occur from [2]. XAS is performed by sweeping the energy of the incident beam and measuring the

intensity of the transited beam as shown by 3.2. Here, the two distinct peaks are as a result of the sharp electron transitions at roughly 707 eV and 720 eV which are referred to as Fe L_3 and L_2 absorption edges.

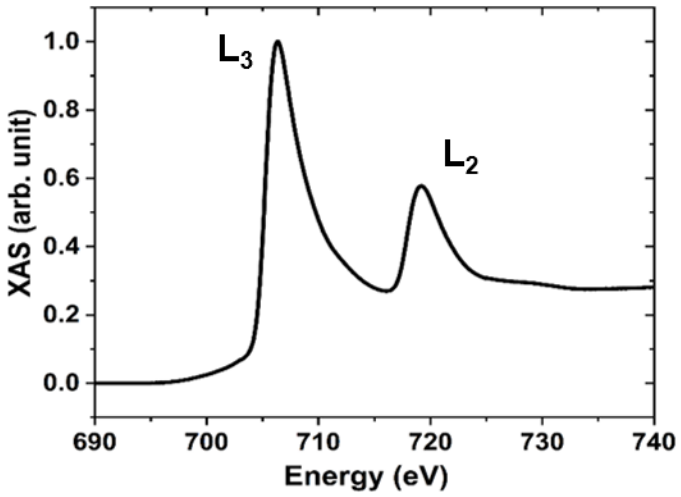

Figure 3.2: X-Ray absorption of BCC Fe at the L_3 and L_2 edges.

The two absorption edges arise from electron transitions from the $2p$ electron orbital to empty $3d$ valence states. To understand this better, refer to figure 3.3 which shows the attenuation and ejection of the core-electrons in Fe. Figure 3.3a) shows a simplified diagram of the electron configuration of Fe before absorption of X-Rays. Figure 3.3b) shows the electron configuration once the X-Rays with the absorption edge intensity have been absorbed at the L-edges and the electron has become ejected from the $2p$ to the $3d$ orbital. This can be more clearly understood by referring to figure 3.3c) which shows the split energy levels of the $2p$ orbital. The $2p$ orbital is split into two states, $2p_{3/2}$ and $2p_{1/2}$ where the later possesses a larger binding energy due to its closer proximity to the nucleus [3]. In figure 3.3d) once the X-Ray energy absorbed by the $2p_{3/2}$ electron is roughly equal to the L_3 absorption edge energy (i.e. 707 eV), it is ejected to an empty state in the $3d$ orbital and releases its energy in form of a photoelectron. This released photoelectron is what is directly or indirectly measured during XAS. If the measured photoelectron is released from an electron originating from $2p_{3/2}$ state then the energy released is referred to as the L_3 edge energy, and if the electron originates from the $2p_{1/2}$ state it is referred to as the L_2 edge energy [4]. In the next section,

various detection mechanisms of this photoelectron will be explained in more detail.

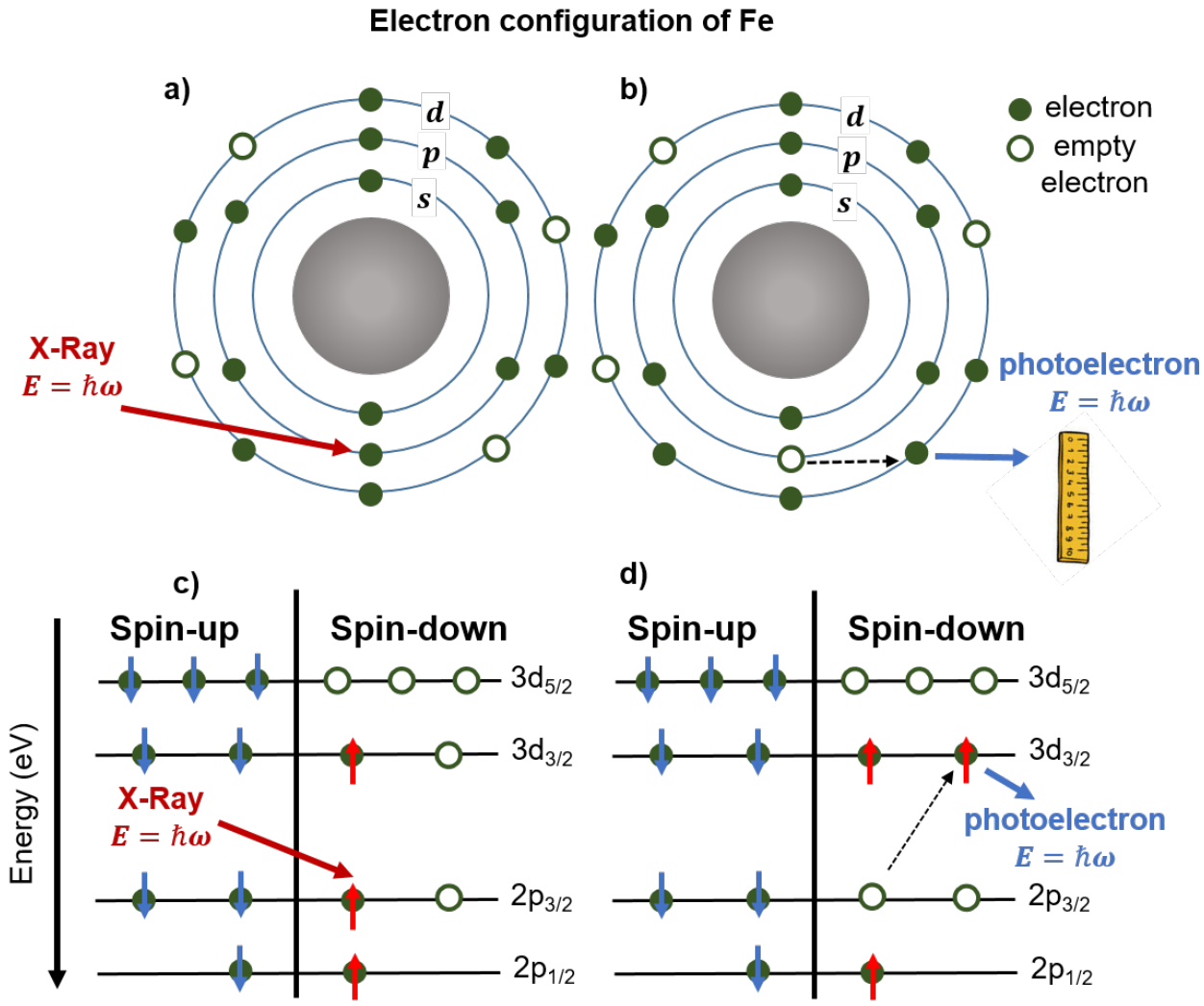

Figure 3.3: Absorption of X-Rays at the Fe L_3 edge. a) electron configuration of Fe before absorption of X-Rays. b) electron configuration of Fe after absorption of X-Rays showing core-electron ejection from p to empty d orbital. c) Detailed electronic states of Fe before absorption of X-Rays. d) electron transition from $2p_{3/2}$ state to empty $3d_{3/2}$ state showing L_3 absorption edge.

3.2 XAS Detection Methods

3.2.1 Transmission Mode

As shown in the previous section in figure 3.1, a direct measurement of the X-Ray absorption across the cross-section is through the transmittance of the photon flux through the sample. A major disadvantage of this detection method has to be that samples need to be extremely thin and mounting them within apparatuses are troublesome. However, a major advantage of transmission mode measurements are detection through the entire bulk of the sample rather than just the surface. The initial beam intensity of the sample I_0 is measured by a second grid typically either a solid metal plate or silicon photodetector [5, 6].

3.2.2 Total Electron Yield (TEY)

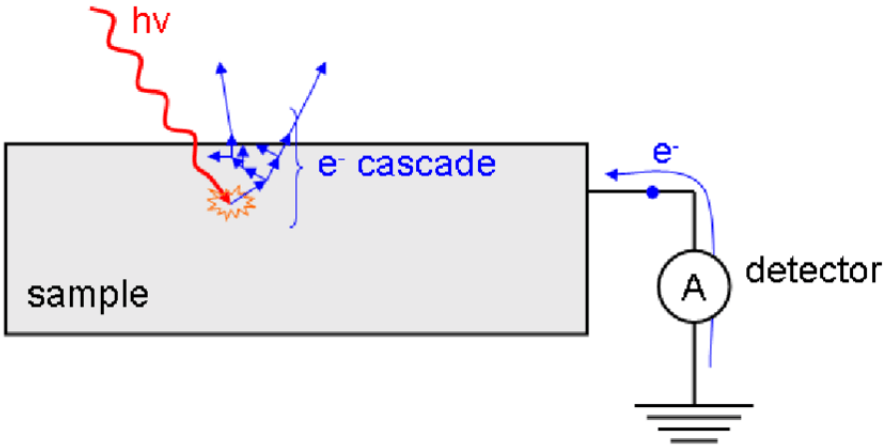

Figure 3.4: Sample configuration in total electron yeild (TEY) measurement mode from reference [7].

Figure 3.4 shows the sample mounted in total electron yield (TEY) mode. In this type of measurement, the absorbed X-Ray intensity is not directly measured as in transmission mode. Instead the the photoelectrons that are generated are measured by the drain current

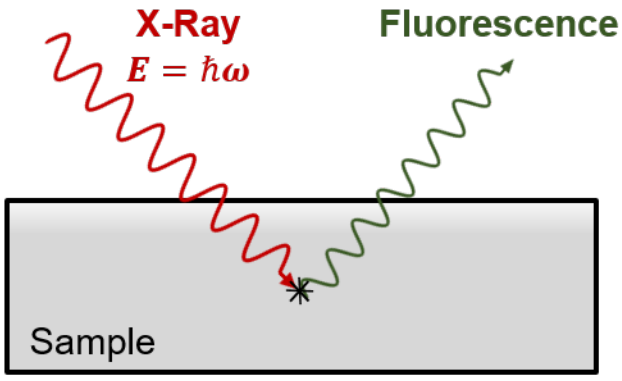

Figure 3.5: Schematic of interaction of X-Rays with sample in fluorescence yield measurement mode.

of the sample by a pico-ammeter [7]. Therefore, the absorption intensity measured by the drain current I_e is given by 3.2.

$$I_e = I_0 \mu z \tag{3.2}$$

The TEY is proportional to μ if the absorption length of the incoming X-Rays are larger than the average escape depth of the photoelectrons [5]. Since the probing depths of the secondary electrons generated are roughly 20 Å, the measurement modes are extremely sensitive on the surface. This becomes a problem for magnetic films with capping layers as the measurement mode is not sensitive at greater depths.

3.2.3 Fluorescence Yield (FY)

Due to the impracticality of using ultra-thin films for transmission mode measurements and the rather weak penetrative sensitivity of TEY, researchers have turned their interest to other detection methods of the linear X-Ray coefficient. Figure 3.5 shows the interaction

of X-Rays with a sample in fluorescence yield mode. Utilizing secondary effects such as Auger electrons and X-Ray florescence are proportional to the absorption under the proper conditions and can be utilized to determine μ [8]. Dissimilar to Auger electrons, fluorescence photons are not charged particles and are insensitive to magnetic fields [9] which become crucial for X-Ray measurements with an applied magnetic field. In addition, fluorescence photons are able to escape from insulating samples whereas Auger electrons cannot. In addition, fluorescence electrons can escape at larger depths, allowing greater penetration depths in samples [10].

3.3 X-Ray Circular Magnetic Dichroism (XMCD)

Recall that XMCD is used to determine the magnetic response of any element with a net spontaneous magnetization. For 3d transition metals, the magnetic moment arises from unpaired 3d orbital electrons whereas for rare-earth elements the magnetic moment arises from unpaired 4f electrons. Therefore, XMCD on 3d metals is typically performed at the $L_{2,3}$ absorption edges whereas for rare-earth elements it is performed at the $M_{4,5}$ absorption edges, and the reasons for this shall become clear at the end of this section. At the core, XMCD is performed by taking the difference in the absorption spectra as a function of energy of left and right-handed circularly polarized X-Rays in a fully saturated magnetic material. Figure 3.6 shows the response with the two circular polarizations denoted by the sign of μ and the XMCD which is the difference between the two. In practice, this dichroism can be obtained in various ways and in order to understand the reasons for this, the detailed electronic structure of Fe must be revisited.

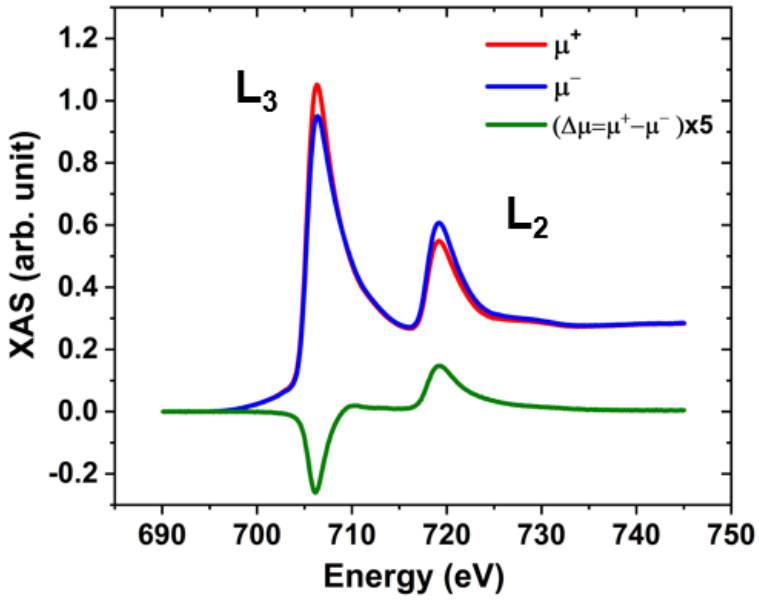

Figure 3.6: X-Ray Magnetic Circular Dichroism (XMCD) performed at the Fe $L_{2,3}$ edges in thin film $Ni_{81}Fe_{19}$.

Figure 3.7 shows the spin-polarized electronic configuration of the $2p$, $3d$, and $4s$ electronic states in Fe. It has to be noted that the $2p_{3/2}$ and $2p_{1/2}$ states have opposing spin-orbit coupling such that their total angular momentum J are $J = L+S$ and $J = L-S$ respectively. In XMCD, left and right-handed circularly polarized X-Rays are utilized to couple with these spin-up ($J = L+S$) and spin-down ($J = L-S$) states and provide preferential absorption due to the imbalance in the spin-up/spin-down density of states that are the origin of magnetism in magnetic elements [11]. Referring back to figure 3.6, as left-handed circularly polarized X-Rays (μ^+) are applied at the absorption edges, the preferential absorption for spin-up electrons occurs as shown in figure 3.7b) and only certain spin-up states may be filled. Now once right-handed polarization (μ^-) is applied at the absorption edges, the preferential absorption for spin-down electrons occurs and they cannot fall into similar energy states as in the spin-up (μ^+) polarization [12]. Therefore, due to the imbalance in the spin-up and spin-down density of states in magnetic materials, XMCD can be used as a method to

investigate the magnetic properties in materials at each individual element.

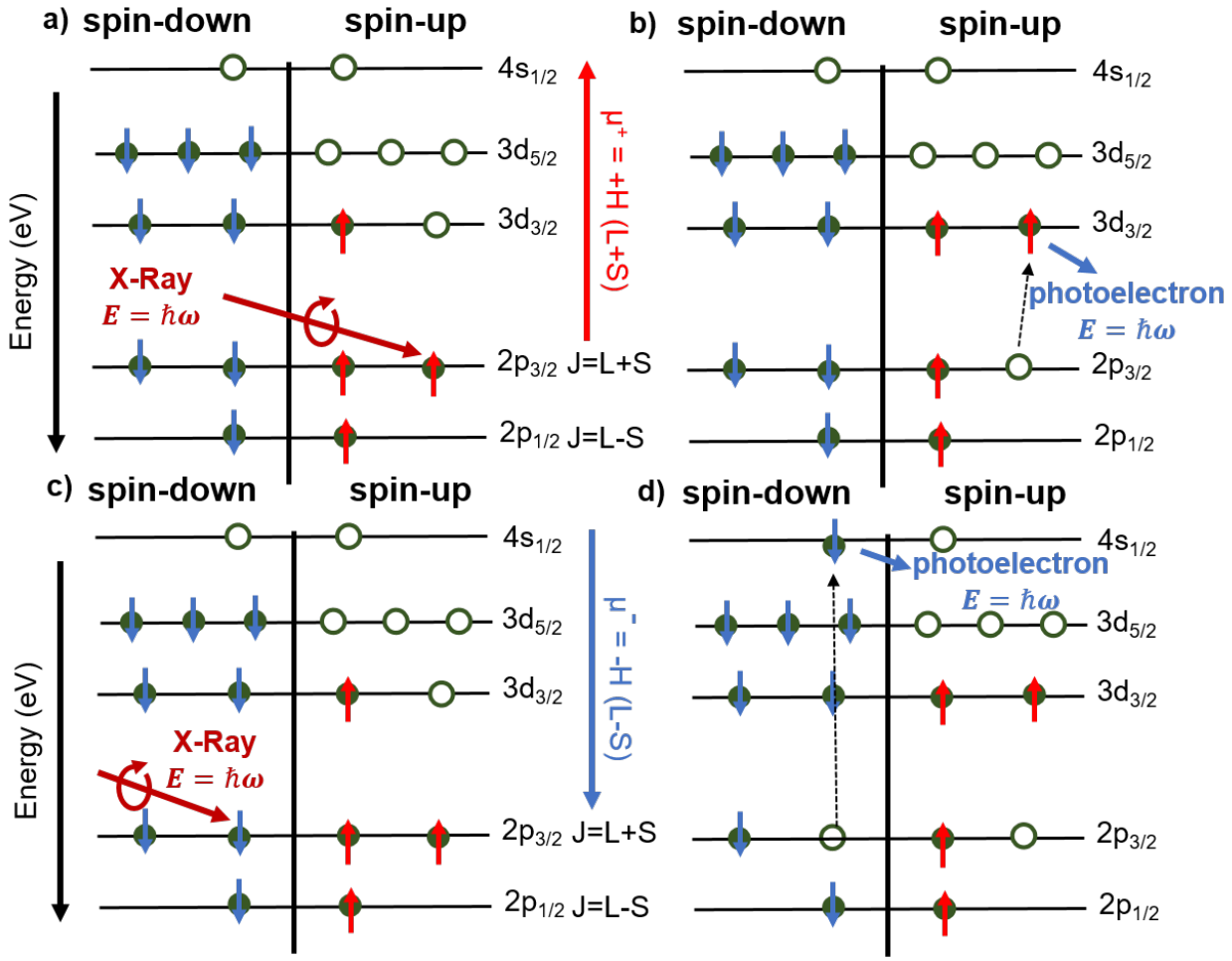

Figure 3.7: Spin-polarized absorption of X-Rays at the Fe L_3 edge. a) electron configuration of Fe before absorption of left-handed circularly X-Rays (μ^+). b) electron configuration of Fe after absorption of (μ^+) X-Rays showing that spin-up states may only occupy empty $3d$ spin-up states. c) electron configuration of Fe before absorption of right-handed circularly X-Rays (μ^-). d) electron configuration of Fe after absorption of (μ^-) X-Rays showing that spin-down states can only occupy empty spin-down states in the $4s_{1/2}$ state as all $3d$ spin-down states are fully occupied.

In practice however, the two polarizations in XMCD can be obtained by switching the orientation of the applied magnetic field, while holding the circular polarization constant and sweeping the photon energy. This provides faster sequential XAS scans as switching the polarization takes quite sometime to fully stabilize and may cause significant discrepancies in measurements. Therefore, by application of a positive magnetic field ($\mu^+ = +H$) coupling

with the spin-up states ($J = L + S$) is achieved. Subsequently, application of a negative magnetic field ($\mu^- = -H$) results in preferential absorption with the spin-down states ($J = L - S$). However, as the magnetism of elements can be directly probed, the magnetic moments of individual atomic elements may also be obtain by applying the XMCD sum rules which shall be introduced in the following section.

3.4 XMCD Sum Rules

In 1992, B.T. Thole developed a set of sum rules to deduce the orbital and spin magnetic moments of elements from the XAS and XMCD spectra [13, 14]. This was done using the opposing spin-orbit coupling at the transition metal $L_{2,3}$ edges. For transition metals, XMCD measurements performed at the L-edges are split into the L_3 edge (electron transition from $2p_{3/2}$ state to empty $3d$ states) and the L_2 edge (electron transition from $2p_{1/2}$ state to empty $3d$ states) as a result of the spin-orbit coupling of the $2p$ hole [12]. The $2p_{3/2}(L + S)$ and $2p_{1/2}(L - S)$ states governing the electron transitions at the L_3 and L_2 edges possess opposing spin-orbit coupling with an energy intensity ratio of 2 to 1 [15]. As the exact electron transitions at the $L_{3,2}$ edges ($2p_{3/2}$ & $2p_{1/2}$ $\rightarrow$ empty $3d$ states) are unknown, the XMCD sum rules integrates over the entire photon energy spectrum to include all possible electron transitions [13, 14]. As such, the elemental orbital $< L_z >$ and spin $< S_z >$ angular momentum along the beam axis (z-axis) can be determined by integrating the XAS and XMCD spectra with respect to the photon energy at the characteristic edge energies. $< L_z >$ can be determined by integrating the XMCD spectrum with respect to the photon energy (E) at the $L_{2,3}$ edges [12, 15, 11] for transition metals given by equation 3.3.

$$\langle L_z \rangle_{3d} = -\frac{2n_h}{N} \int_{L_{2,3}} (\Delta\mu_{L_3} - \Delta\mu_{L_2}) dE \tag{3.3}$$

In equation 3.5, n_h represents the number of holes (i.e. unoccupied final states) in the $3d$ orbital of each element. These values can be whole integers for example elemental Fe holds has 6 electrons in the 3d orbital therefore, it has 4 holes. These holes represent the empty states where an electron can be occupied to fulfill the transitions at the $L_{2,3}$ edges. Equation **??** represents the integrated spectrum of the unpolarized radiation N, found by integrating the averaged polarized XAS spectra (i.e. $1/2(\mu^+ + \mu^-)$) with respect to the photon energy (E) as shown by equation 3.4.

$$N = 3 \int \frac{1}{2}(\mu^+ + \mu^-)dE \tag{3.4}$$

The spin angular momentum $< S_z >$ is calculated using the intensity ratios between the $L_{2,3}$ edges ($2L_3$ to $1L_2$) for Fe [15, 11] given by equation 3.5. Referring back to 3.7, the intensity ratio of 2:1 is due to the fact that there are a total of 4 electrons in the $2p_{3/2}$ state and 2 electrons in the $2p_{1/2}$ state. The term $< T_z >$ represents the intra-atomic dipole operator related to the quadrupole moment of the spin density distribution [15] and is a correction term for the spin momentum $< S_z >$ [11].

$$\langle S_z \rangle_{3d} = -\frac{3n_h}{N} \int_{L_{2,3}} (\Delta\mu_{L_3} - 2\Delta\mu_{L_2})dE - 7\langle S_z \rangle \tag{3.5}$$

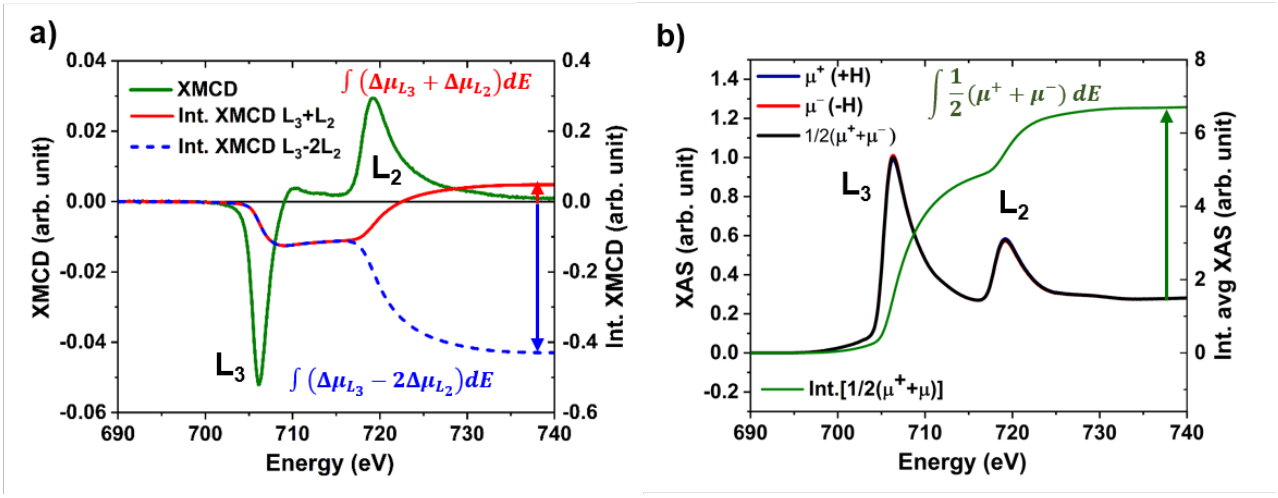

Figure 3.8: XMCD sum rules of Fe $L_{2,3}$ edges in thin film $Ni_{81}Fe_{19}$.

Application of the XMCD sum rules to the measured polarized XAS and XMCD absorption spectra can be done by referring to figure 3.8. Here, figure 3.8a) shows the XMCD in green followed by the spin and orbital integration curves in blue (dashed) and red (solid) respectively. The orbital moment integration curve shown in red denoted by (Int. XMCD $L_3 + L_2$) was performed by integration of the XMCD spectra with respect with the energy. The spin moment integration curve was obtained by taking the difference of the XMCD spectra with a 2x factor multiplied to the XMCD at the L_2 edge. As it can be seen in figure 3.8a), the integration curves both converge to a value shown by the right axis of the plot. These converged values for the orbital and spin moments can be directly applied in equations 3.3 and 3.5 to obtain the orbital and spin moment of the $3d$ elements respectively. To determine N, the polarized XAS spectra must be averaged and integrated with respect to the energy. Shown in figure 3.8b), the polarized XAS spectra are averaged and subsequently integrated. Similar to the integrated XMCD curves, the value in which the integration curve converges to can be directly applied in equation 3.4 to determine N accordingly.

The XMCD sum rules for rare-earth elements follow similar principles to the transition metals. However, since their magnetic moments arise from unpaired electrons in the $4f$

orbital, the sum rules are different in nature. XMCD measurements performed at the M-edges are split into the M_5 edge (electron transition from $3d_{5/2}$ state to empty $4f$ states) and M_4 edge (electron transition from $3d_{3/2}$ state to empty $4f$ states) as a result of spin-orbit coupling of the $3d$ hole [16]. The $3d_{5/2}(L+S)$ and $3d_{3/2}(L-S)$ states governing the electron transitions at the M_5 and M_4 edges have opposing spin-orbit coupling with an energy intensity ratio of 3 to 2 [17]. Therefore, by using polarized XAS scans (i.e. $\mu^+ = +1T\ (L+S)$ & $\mu^- = -1T\ (L-S)$), the preferential absorption of the spin-up electrons at the M_5 edges and spin-down electrons at the M_4 edges can be determined similarly to the $3d$ metals [11]. As the exact electron transitions at the $M_{5,4}$ edges ($3d_{5/2}$ & $3d_{3/2}$ $\rightarrow$ empty $4f$ states) are unknown, the XMCD sum rules integrates over the entire photon energy spectrum to include all possible electron transitions [13, 14]. As such, the elemental orbital $< L_z >$ and spin $< S_z >$ angular momentum along the beam axis (z-axis) can be determined by integrating the XAS and XMCD spectra with respect to the photon energy at the characteristic edge energies. $< L_z >$ can be determined by integrating the XMCD spectrum with respect to the photon energy (E) at the $M_{4,5}$ edges [16, 17] using equation 3.6.

$$\langle L_z \rangle_{4f} = -\frac{3n_h}{N} \int_{M_{4,5}} (\Delta\mu_{M_5} - \Delta\mu_{M_4}) dE \tag{3.6}$$

The spin angular momentum $< S_z >$ is calculated using the intensity ratios between the $M_{4,5}$ edges ($3M_5$ to $2M_4$) [16, 17] and is given by equation 3.7.

$$\langle S_z \rangle_{4f} = -\frac{3n_h}{2N} \int_{M_{4,5}} (\Delta\mu_{M_5} - \frac{3}{2}\Delta\mu_{M_4}) dE - 3\langle T_z \rangle \tag{3.7}$$

Similar to $3d$ elements, $< T_z >$ represents the intra-atomic dipole operator related to the quadrupole moment of the spin density distribution [15] and is a correction term for the spin momentum $< S_z >$ [11], n_h represents the number of holes in the $4f$ orbital, and N for is the same as equation 3.4.

Chapter References

[1] J Stohr and HC Siegmann. Magnetism, from fundamentals to nanoscale dynamics, ser. *Solid State Sciences Series. Berlin: Springer*, 2006.

[2] Joseph I Goldstein, Dale E Newbury, Joseph R Michael, Nicholas WM Ritchie, John Henry J Scott, and David C Joy. *Scanning electron microscopy and X-ray microanalysis*. Springer, 2017.

[3] Frank De Groot. Multiplet effects in x-ray spectroscopy. *Coordination Chemistry Reviews*, 249(1-2):31–63, 2005.

[4] John Evans and Moniek Tromp. *X-ray absorption spectroscopy for the chemical and materials sciences*. Wiley Online Library, 2018.

[5] Tobias Funk, Aniruddha Deb, Simon J George, Hongxin Wang, and Stephen P Cramer. X-ray magnetic circular dichroism—a high energy probe of magnetic properties. *Coordination Chemistry Reviews*, 249(1-2):3–30, 2005.

[6] CT Chen, YU Idzerda, H-J Lin, NV Smith, G Meigs, E Chaban, GH Ho, E Pellegrin, and F Sette. Experimental confirmation of the x-ray magnetic circular dichroism sum rules for iron and cobalt. *Physical review letters*, 75(1):152, 1995.

[7] Samuel Tardif, V Favre-Nicolin, F Lançon, E Arras, M Jamet, A Barski, C Porret, Pascale Bayle-Guillemaud, P Pochet, T Devillers, et al. Strain and correlation of

self-organized ge 1- x mn x nanocolumns embedded in ge (001). *Physical Review B*, 82(10):104101, 2010.

[8] Christian Michael Praetorius. *Ce M4, 5 XAS and XMCD as Local Probes for Kondo and Heavy Fermion Materials-A Study of CePt5/Pt (111) Surface Intermetallics*. PhD thesis, Universität Würzburg, 2015.

[9] AJ Achkar, TZ Regier, EJ Monkman, KM Shen, and DG Hawthorn. Determination of total x-ray absorption coefficient using non-resonant x-ray emission. *Scientific reports*, 1(1):1–8, 2011.

[10] Daisuke Asakura, Eiji Hosono, Yusuke Nanba, Haoshen Zhou, Jun Okabayashi, Chunmei Ban, Per-Anders Glans, Jinghua Guo, Takashi Mizokawa, Gang Chen, et al. Material/element-dependent fluorescence-yield modes on soft x-ray absorption spectroscopy of cathode materials for li-ion batteries. *AIP Advances*, 6(3):035105, 2016.

[11] Joanna K Kowalska, Brahamjot Nayyar, Julian A Rees, Christine E Schiewer, Sonny C Lee, Julie A Kovacs, Franc Meyer, Thomas Weyhermuller, Edwige Otero, and Serena DeBeer. Iron $L_{2,3}$-edge X-ray absorption and X-ray magnetic circular dichroism studies of molecular iron complexes with relevance to the FeMoco and FeVco active sites of nitrogenase. *Inorganic chemistry*, 56(14):8147–8158, 2017.

[12] Heiko Wende. Recent advances in X-ray absorption spectroscopy. *Reports on progress in physics*, 67(12):2105, 2004.

[13] B T Thole, Paolo Carra, F Sette, and Gerrit van der Laan. X-ray circular dichroism as a probe of orbital magnetization. *Physical review letters*, 68(12):1943, 1992.

[14] Paolo Carra, B T Thole, Massimo Altarelli, and Xindong Wang. X-ray circular dichroism and local magnetic fields. *Physical Review Letters*, 70(5):694, 1993.

[15] Yoshiki Teramura, Arata Tanaka, and Takeo Jo. Effect of coulomb interaction on the X-ray magnetic circular dichroism spin sum rule in 3d transition elements. *Journal of the Physical Society of Japan*, 65(4):1053–1055, 1996.

[16] Yoshiki Teramura, Arata Tanaka, Thole B T, and Takeo Jo. Effect of Coulomb interaction on the X-ray magnetic circular dichroism spin sum rule in rare earths. *Journal of the Physical Society of Japan*, 65(9):3056–3059, 1996.

[17] Sapana Tripathi. Xmcd investigation at $M_{4,5}$ edges of the rare earth elements in high-performance permanent magnet. 2018.

Chapter 4

Investigation of the Magnetic Anisotropy in Terfenol-D

4.1 Introduction

Manipulating the magnetic moment with applied fields or mechanical strain requires overcoming or manipulating the magnetic anisotropy and represents an important process for devices in spintronic applications. However for rare-earth materials, developing and engineering magnetic anisotropies catered to particular applications are challenging at this time as the impact of the elemental spin-orbital moments towards the overall magnetic response is not well understood [1, 2, 3]. This is specifically important as the magnetic anisotropy arises from spin-orbit coupling between the element's spins and their orbits which couple with the lattice crystal field to dictate the orientation of the magnetic moments and magnetic hardness [4, 5]. Experimental studies have shown that modifying the spin-orbital moments of specific elements within a material strongly influences the magnetic anisotropy [6, 7, 8, 9] and provides an opportunity for developing new materials optimized for particular applications.

However, detailed investigations focused on rare-earth magnetostrictive materials where both the magnetoelastic and magnetocrystalline anisotropic responses are rather large, complex, and dictate the overall magnetic response are presently lacking.

Rare-earth ferrimagnetic $Tb_{0.3}Dy_{0.7}Fe_2$ (Terfenol-D) is one of the most widely investigated giant magnetoelastic materials due to its large room temperature magnetostriction with small magnetocrystalline anisotropy (MCA) [10]. The magnetic properties of Terfenol-D were engineered by alloying ferrimagnetic $TbFe_2$ with $DyFe_2$ to minimize the MCA while retaining large magnetostriction [11, 12]. Previous researchers studied various compositions to optimize the magnetostriction while minimizing the MCA for sonar applications and termed this selected composition (i.e. $Tb_{0.3}Dy_{0.7}Fe_2$) Terfenol-D [13, 13]. Rare-earth thin films such as Terfenol-D have recently become widely utilized in a number of device applications [14, 15], innately demanding the study of various contributions towards the magnetic anisotropy in addition to the magnetocrystalline ones. Therefore, the magnetoelastic contributions towards the magnetic anisotropy must also be studied due to the residual stresses in thin films [16].

Measurement techniques such as soft X-ray absorption (XAS) and X-Ray magnetic circular dichroism (XMCD) paired with the XMCD sum rule calculations have been used to study elemental spin-orbit moments and their influence on the magnetic anisotropy in various materials [17, 18, 19]. These studies are performed by lowering temperatures to increase the magnetic anisotropy due to stronger spin-orbit coupling that can be accurately measured by XMCD [4]. An XMCD study performed on the ferrimagnetic magnetostrictive alloy $DyCo_3$ showed that the enhancement of the thermally induced magnetic anisotropy at lower temperatures was caused by increases in the Dy element's magnetic moment [20, 21]. XMCD spectroscopy on ferrimagnetic multiferroic $TbMnO_3$ showed similar thermally induced MCA changes caused by large increases in the Tb orbital moment [22, 23]. With strong foregoing evidence of the $4f$ orbital contributions to the magnetic anisotropy, we perform XMCD from

100 to 300 K (with liquid nitrogen cooling) and utilize the XMCD sum rules to investigate and directly determine the relationship between the elemental spin and orbital moments with the coercive field and formulate these contributions in terms of the magnetocrystalline and magnetoelastic anisotropies in Terfenol-D thin films.

4.2 Experimental Setup

Terfenol-D thin films were deposited on 2-inch diameter c-plane sapphire substrate using an ultra-high vacuum magnetron sputtering system. A Ta barrier and capping layer were deposited in-situ producing a layered sapphire(430 μm)/Ta(10nm)/Terfenol-D(70nm)/Ta(4nm) structure. The Terfenol-D films were deposited as described in previous work with 70 MPa tensile residual stress [24, 25]. Wavelength dispersive spectroscopy (WDS) measurements indicate the elemental composition of the films were $Tb_{0.3}Dy_{0.7}Fe_2$. A superconducting quantum interference device (SQUID) was used to measure magnetization curves at temperatures from 100 K to 300 K including field cooling curves under an applied magnetic field of 500 Oe.

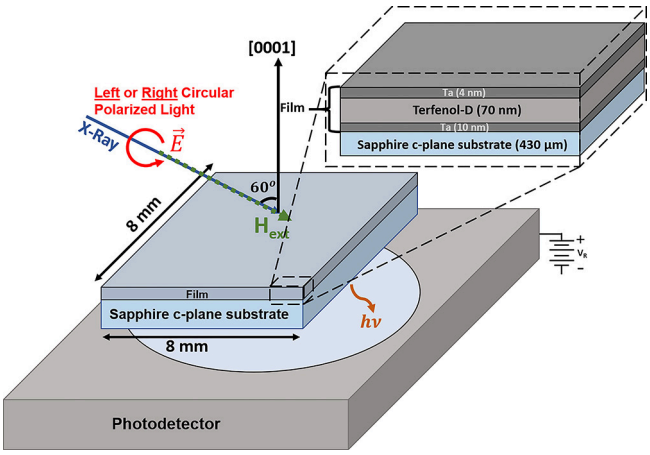

Figure 4.1: Experimental configuration of XAS/XMCD measurements performed in Luminescence yield (LY) mode where the intensity of the X-Ray induced luminescence in the sapphire substrate is measured. The X-ray angle and applied external field H_{ext} are collinear and held at angle 60from the sample normal.

X-Ray absorption (XAS) and X-Ray magnetic circular dichroism (XMCD) at the Dy and Tb $M_{4,5}$ edges, and at the Fe $L_{2,3}$ edges were performed at 100, 150, 200, 250, and 300 K using beamline 6.3.1 at the Advanced Light Source (ALS) of the Lawrence Berkeley National Laboratory (LBNL). Figure 5.1 shows the experimental setup of the XAS and XMCD measurements measured in luminescence yield (LY) mode. In these tests the sample holder is rotated such that the X-Ray, which is collinear with the applied magnetic field is incident at 60with the sample normal. The Dy and Tb $M_{4,5}$ edges were determined by sweeping the photon energy between 1280-1350 eV and 1220-1290 eV for Dy and Tb respectively, while the Fe $L_{2,3}$ edges were determined by sweeping the photon energy between 690-740 eV. The XAS scans were recorded by holding the light's circular polarization constant and sweeping the photon energy while saturating the samples at +1 T (μ^+) and -1 T (μ^-) to determine the XMCD signal ($\Delta\mu = \mu^+ - \mu^-$). The element specific M-H curves were determined by holding the photon energy constant at the characteristic edge energies and measuring the XMCD signal while sweeping the magnetic field from -1.5 T to +1.5 T. The elemental spin and orbital moments for Dy and Tb at the $M_{4,5}$ [26, 27] and Fe $L_{2,3}$ [28, 29, 30] edges were derived from the XAS and XMCD spectra using the XMCD sum rules (see chapter 3 for more details).

4.3 Results & Discussion

Figure 2(a-c) shows the polarized XAS scans (i.e. μ^+ & μ^-) and the integrated averaged XAS ($Int.\ XAS(1/2(\mu^+ + \mu^-))$) with respect to the photon energy at the Dy and Tb $M_{4,5}$ edges, and the Fe $L_{2,3}$ edges at 100 K respectively. The polarized XAS spectra in all three figures show prominent signals at the characteristic edges from Dy, Tb, and Fe without signs of oxidation.

Figure 5.2(d-f) shows the XMCD ($\Delta\mu = \mu^+ - \mu^-$), the integration of the XMCD for the

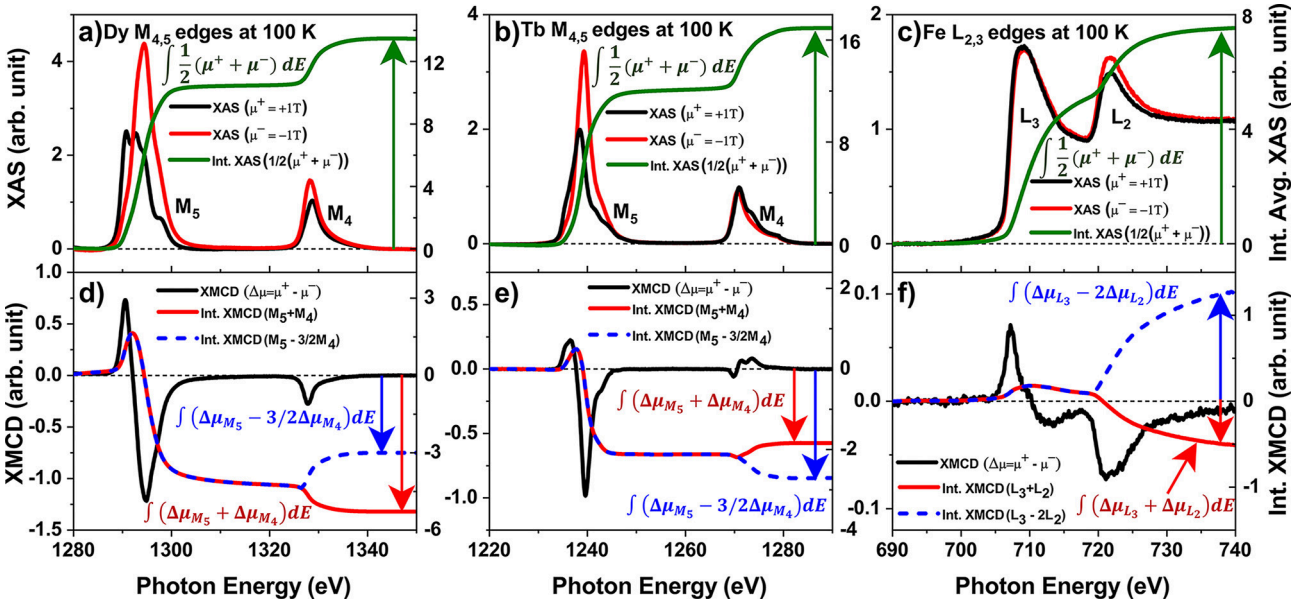

Figure 4.2: XAS and XMCD spectra taken at the Dy and Tb $M_{5,4}$ and Fe $L_{3,2}$ edges at 100 K. (a-c) Polarized XAS spectra (μ^+ & μ^-), and the integrated averaged polarized XAS ($\mu_{avg} = 1/2[\mu^+ + \mu^-]$) with respect to energy for the Dy and Tb $M_{4,5}$ and Fe $L_{2,3}$ edges. (d-f) the XMCD spectra ($\Delta\mu = \mu^+ - \mu^-$), XMCD integration for the orbital angular momentum (solid red curve), and XMCD integration for the spin angular momentum (dashed blue curve) at the Dy and Tb $M_{4,5}$ and Fe $L_{2,3}$ edges.

orbital angular momentum denoted by the solid red curve, and the integration of the XMCD for the spin angular momentum shown by the dashed blue curve for Dy, Tb, and Fe respectively at 100 K. The values used in the XMCD sum rule calculations for orbital $< L_z >$ and spin $< S_z >$ moments are calculated from the XMCD spectra shown in Figures 5.2(d-f) at the $M_{4,5}$ edges and the $L_{2,3}$ edges using equations S1-S5 in the supplemental material. The positive and negative values [Figure 5.2(d-f)] for the integrated XMCD curves shows the parallel and antiparallel alignment of the elemental spin and orbital moments within the alloy. For Dy in Figure 5.2(d), both spin and orbital moment integration curves converge to negative values indicating a parallel spin-orbit alignment as expected by Hund's rules. Tb shows similar parallel spin-orbit alignment [Figure 5.2(e)] as Dy, indicating that both rare-earths are ferromagnetically coupled as their integration curves converge to negative values [31]. However, the Fe XMCD signal and the spin and orbital moment integration curves in Figure 5.2(f) do not fully converge. The expected antiferromagnetic coupling of the Fe spin

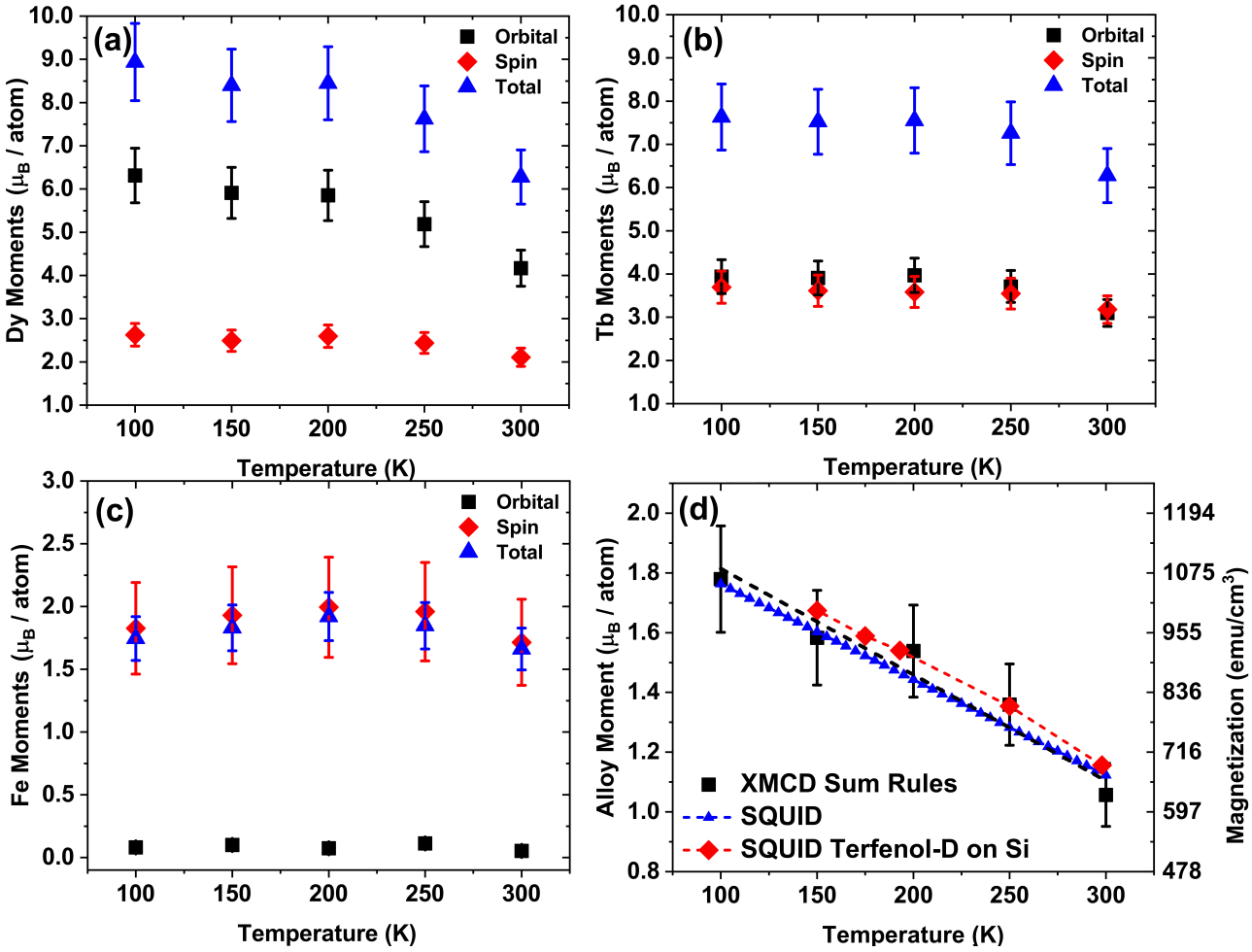

Figure 4.3: (a-c) The orbital, spin, and total (spin+orbital) moments for Dy, Tb, and Fe calculated by the XMCD sum rules with respect to temperature at 100, 150, 200, 250, and 300 K. (d) The Terfenol-D ($Tb_{0.3}Dy_{0.7}Fe_2$) alloy moment calculated based on composition by the XMCD sum rules, measured by SQUID, and Terfenol-D on (100) Silicon substrate measured by SQUID reproduced from Mohanchandra *et al.* AIP Advances **5**, 097119 (2015), with the permission of AIP Publishing.

moment with the Dy and Tb spin moments is measured here as the trend of the Fe spin moment integration curve appears to converge positively whereas the rare-earth spin moments converge negatively [32]. However, the trends of the integration curves suggest an interesting phenomenon of antiparallel spin-orbit alignment in Fe as the spin and orbital moment integration curves converge to positive and negative values respectively. Previous studies report that the underlying cause of an antiparallel spin-orbit alignment in Rare-Earth-Fe_2 (RE-Fe_2) systems may be due to the complex interactions of the RE($5d$)-RE($4f$) and RE($5d$)-Fe($3d$) electron hybridizations [33, 34, 35, 36, 37].

Figure 5.3(a-c) shows the moments of Dy, Tb, and Fe calculated by the XMCD sum rules (Eq S1-S5) at 100, 150, 200, 250, and 300 K using the data presented in Figure 5.2. The values chosen for the Fe XMCD sum rule calculation were determined by approximating the final converging value of the spin-orbit integration curves shown in Figure 5.2(f). For all three of these figures, the total moment represents the sum of the orbital $< L_z >$ and spin $< S_z >$ moments where the error bars are 10% for all moments except for the Fe orbital moment at 20% due to inaccuracies associated with the small orbital angular momentum of $3d$ transition metals [38, 39]. Figure 5.3(d) shows the Terfenol-D alloy moment calculated based on composition (i.e. $Tb_{0.3}Dy_{0.7}Fe_2$) using the elemental spin and orbital moments calculated by the XMCD sum rules, and measured by SQUID. The other SQUID measurement was taken from a Terfenol-D thin film sample deposited on a Silicon substrate with similar elemental composition confirmed by WDS [25].

Figure 5.3(a) shows the variation of the Dy spin and orbital moments with temperature. The spin moment in Dy initially increases as the temperature is reduced from 300 to 200 K then remains relatively constant with further temperature reductions, whereas the Dy orbital moment steadily increases. These results suggest the Dy orbital moment is the major contributor to the Terfenol-D alloy moment in the low temperature regime. Compared to the Dy^{3+} free ion with a moment of $10.64\mu_B$/atom, the total moment of 8.9 μ_B/atom at

100 K for Dy agrees reasonably well with previous reports for the values of the Dy moment (8.2 - 10 μ_B/atom) [40, 41, 42, 43, 44]. Noticeably, the average total Dy moment measured (i.e. 8.9 μ_B/atom at 100 K) is slightly higher than the reported average total Dy moment in $DyFe_2$ (8.3 μ_B/atom at 77 K) [45]. Figure 5.3(b) shows the Tb spin and orbital moments are similar in magnitude and exhibit moderate increases with temperature reductions from 100 to 300 K. However, there appears to be a moderate plateau region for temperatures below 200 K. The Tb^{3+} free ion with a theoretical total moment of 9.4 μ_B/atom contrasted with the total moment of 7.6 μ_B/atom measured at 100 K here [Figure 3(b)], appears to be reasonable (7.6 - 9.4 μ_B/atom) compared to reported values considering that our average Tb moment matches exactly with the reported average values of Tb in $TbFe_2$ [10, 45, 22, 46, 47]. Figure 5.3(c) shows the absolute value of the Fe spin moment increases following temperature reductions with a peak of 1.9 μ_B/atom at 200 K, whereas the plateaus at 0.101 μ_B/atom at 200 K. Figure 5.3(d) shows the total Terfenol-D moment linearly increases as temperatures were lowered. The alloy moment calculated using XMCD sum rule calculations compares well with the measured SQUID data, supporting the accuracy of the XMCD sum rule calculations [25].

Figure 4(a-b) shows the magnetic hysteresis loops of Terfenol-D (by SQUID), and element-specific Tb, Dy, and Fe (determined by XMCD) measured at 300 K and 100 K. Both figures show that the Fe total moment remains antiparallel to Dy and Tb for both temperatures studied with hysteresis loops showing opposing polarity. At both temperatures, Dy and Tb dominate the contribution to the overall alloy moment as their element-specific hysteresis loops have the same polarity with the Terfenol-D loop measured by SQUID. Notably, all of the atomic elements (Dy, Tb, Fe) along with Terfenol-D show almost identical coercive fields at each measured temperature. This is due to the fact that there is strong exchange coupling of the rare-earths to Fe due to the intermetallic nature of Terfenol-D.

Figure 4.5(a) plots the Terfenol-D coercive fields measured by SQUID, predicted coercive field

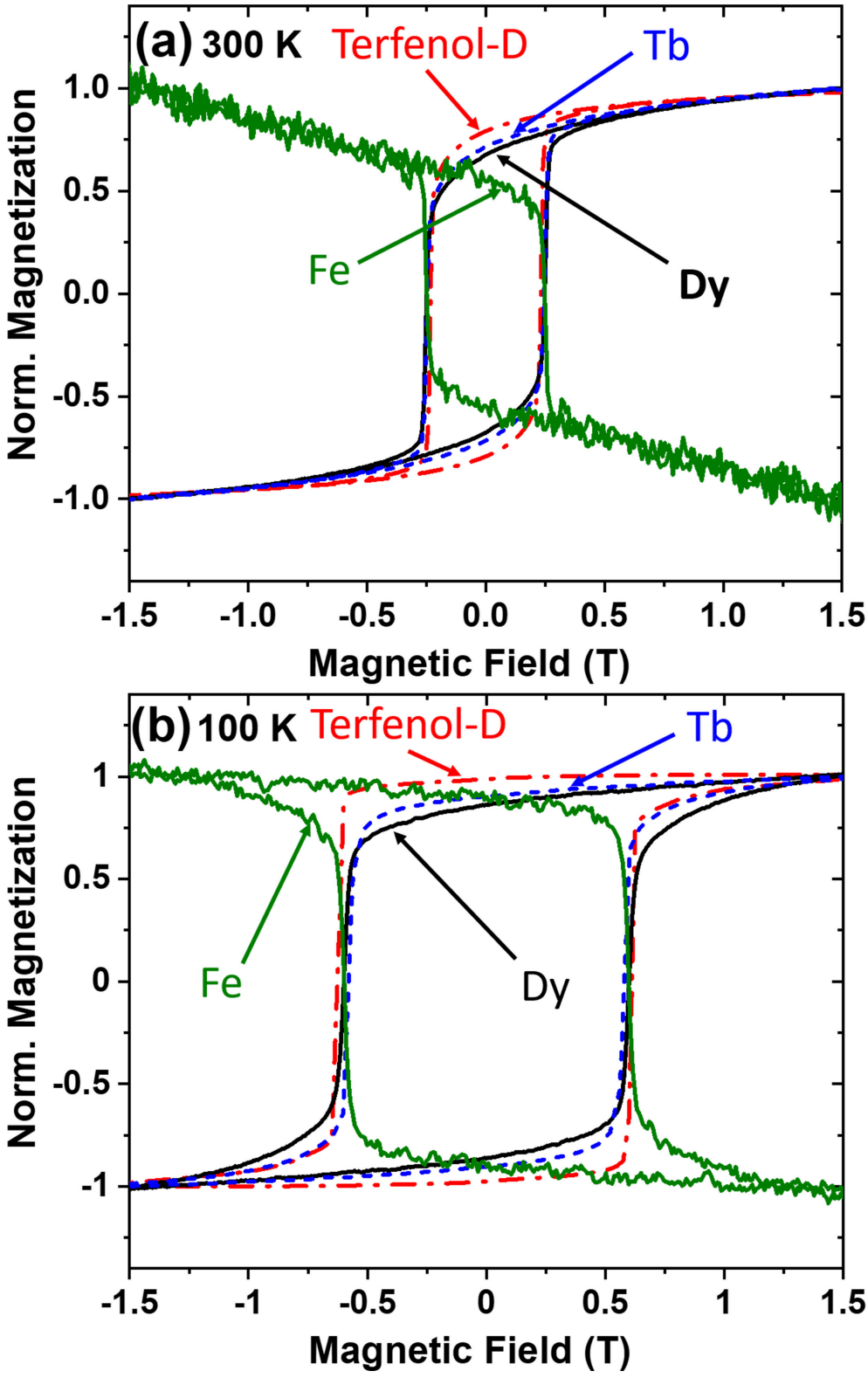

Figure 4.4: M-H loops from Terfenol-D (by SQUID), Tb, Dy, and Fe element-specific loops by XMCD measured at (a) 300 K (b) 100 K.

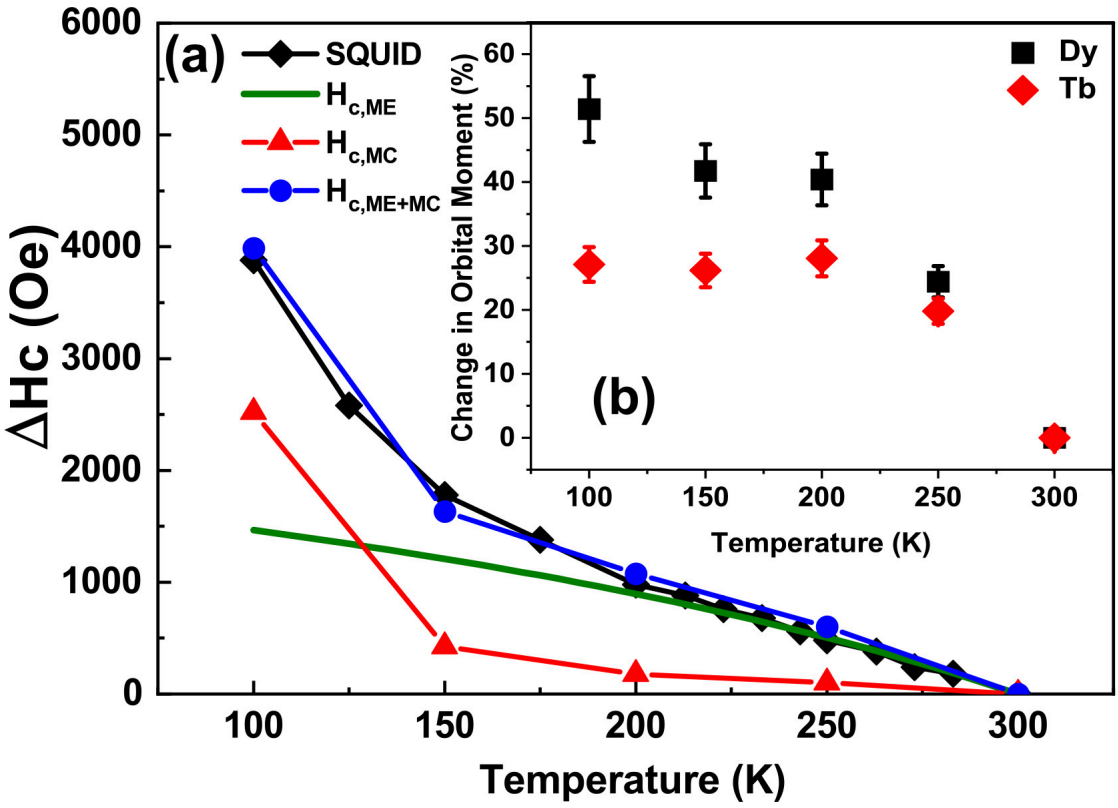

Figure 4.5: (a) Change in coercivity of Terfenol-D (by SQUID), and the expected contributions to the coercive field due to magnetoelastic (H_{ME}) anisotropy induced by thermal expansion mismatch of Terfenol-D film and sapphire substrate, the magnetocrystalline (H_{MC}) anisotropy, and their sum (i.e. H_{MC+ME}). (b) Percent change in the magnitude of the rare-earth orbital moments with temperature.

($H_{c,ME}$) changes attributed to magnetoelastic anisotropy, and predicted coercive field ($H_{c,MC}$) changes attributed to the MCA as a function of temperature. The magnetoelastic anisotropy ($H_{c,ME}$) contribution is induced by thermal expansion mismatch between the sapphire substrate and Terfenol-D film. This was calculated using the magnetoelastic energy relationship $E(T)_{ME} = \frac{3}{2}\lambda_s Y \epsilon_{th}(T) \approx \mu_0 M_s(T) \Delta H_{c,ME}$. Here, $\epsilon_{th}(T) = (\alpha_{sap} - \alpha_{TD})\Delta T$, ϵ_{th} is the is the thermally induced strain with $\alpha_{sap} = 3.4 \times 10^{-6}\ \epsilon/K$ [48, 49] and $\alpha_{TD} = 14 \times 10^{-6}\ \epsilon/K$ [50], $\lambda_s = 880\ \mu\epsilon$ is the thin film saturation magnetostriction [24], and $Y = 55\ GPa$ [51, 52, 53] is Terfenol-D's Young's modulus [54, 55, 56].The thermally induced film stresses at 100, 150, 200, 250, and 300 K was 187, 158, 129, 99, and 70 MPa respectively. The MCA ($H_{c,MC}$) contribution to the coercive field was calculated using the 6^{th} order magnetocrystalline energy (E_{MC}) given by $E_{MC} = K_1(T)(\alpha_1^2\alpha_2^2 + \alpha_1^2\alpha_3^2 + \alpha_2^2\alpha_3^2) + K_2(T)(\alpha_1^2\alpha_2^2\alpha_3^2) = \mu_0 M_s(T)\Delta H_{c,MC}$. Here, the $K_1(T)$ & $K_2(T)$ are temperature dependent magnetocrystalline constants obtained from previous test data [57] and α_1^2, α_1^2, & α_3^2 are the directional cosine terms with respect to the easy axis of magnetization (EAM). Since studies were performed on polycrystalline Terfenol-D, it is not possible to precisely determine the family of directions of the EAM. In our $H_{c,MC}$ calculations, various EAMs directions were applied but all provided similar predictions of coercive field values. Therefore, the large predicted increases in $H_{c,MC}$ with reducing temperature are dominated by the increases in the anisotropy constants $K_1(T)$ & $K_2(T)$ as reported by ref. [57].

In Figure 4.5(a), the SQUID coercive field measurements increases as the temperature is decreased from 300 to 150 K followed by a rapid increase for temperatures below 150 K. The predicted magnetoelastic ($H_{c,ME}$) contributions to the coercive field shown by the green curve displays a non-linear increase with a pseudo-linear increase below 200 K due to the increasing saturation magnetization with temperature. For temperatures between 300 to 200 K, $H_{c,ME}$ appears to be the major contributor to the changing coercive field based on the relative agreement in this range, while for temperatures below 200 K other anisotropies must be considered. The MCA ($H_{c,MC}$) contributions to the coercive field shown in the red

curve displays a significant nonlinear trend. For temperatures between 300 to 200 K, these contributions are relatively small compared to the $H_{c,ME}$ curves and deemed insignificant. At temperatures below 200 K, $H_{c,MC}$ increases rapidly and is attributed to the increase in the magnetocrystalline constants (i.e. $K_1(T)$ & $K_2(T)$). By reviewing the sum of the magnetoelastic anisotropy and MCA ($H_{c,ME+MC}$) contributions presented by the blue curve, good agreement with the SQUID measurements are found. While other contributions to the magnetic anisotropy may exist, $H_{c,MC}$ and $H_{c,ME}$ appear to be the dominant sources of anisotropy. To understand the MCA contributions to the anisotropy, it is necessary to revisit the XMCD data.

The inset of Figure 4.5(b) shows the percent change in the Dy and Tb orbital moments calculated by the XMCD sum rule calculations. Specifically, from 300 to 200 K, both Dy and Tb orbital moments change pseudo-linearly following the magnetoelastic ($H_{c,ME}$) trend presented in Figure 4.5(a). We believe that the increases in the rare-earth orbital moments are due to strain modifying the shape and preferred orientation of the $4f$ orbitals. From 200 to 150 K, the orbital moments remain constant and deviate from the $H_{c,ME}$ trend while exhibiting similarities to the $H_{c,MC}$ (i.e. increases in $K_1(T)$ & $K_2(T)$). For temperatures below 150 K, a significant change in the Dy orbital moment is observed which follows large increases in $H_{c,MC}$. The increases in the anisotropy constants for temperatures between 200 to 100 K are believed to be due to stronger and more directionally dependent spin-orbit coupling in Dy. This conclusion is supported by understanding that the origin of MCA arises from spin-orbit coupling, which originates from the increases in the Dy orbital moment at reduced temperatures. These findings imply that the increases in the rare-earth orbital moments are directly connected to the increases in the anisotropies.

4.4 Conclusion

The elemental spin-orbital moment contributions to the magnetic anisotropy of magnetostrictive polycrystalline Terfenol-D thin film were measured by XMCD. The elementwise M-H curves show the expected antiferromagnetic coupling of Tb and Dy with Fe followed by an antiparallel spin-orbit alignment in Fe. The elemental magnetic moments derived from XMCD and the XMCD sum rules found that all elemental moments show increases from 300 to 200 K. The Dy orbital moment increases below 200 K whereas Tb and Fe moments plateau in this temperature regime. The large increase in the coercive field and MCA at lower temperatures in Terfenol-D were due to the significant increase in the Dy orbital moment. This conclusion is supported by the much larger Dy moment of 8.9 μ_B/atom measured at 100 K in Terfenol-D, which is approximately 16% less than the theoretical max value of the Dy atomic moment (10.64 μ_B/atom). These results are helpful in providing a fundamental understanding of the direct relationship between elemental magnetic moments relative to the components of the magnetic anisotropy, especially in rare-earth magnetostrictive thin films which show considerable promise in future magnetoelastic spintronic applications.

Chapter References

[1] Pedram Khalili Amiri and Kang L Wang. Voltage-controlled magnetic anisotropy in spintronic devices. In *Spin*, volume 2, page 1240002. World Scientific, 2012.

[2] H Béa, M Gajek, M Bibes, and A Barthélémy. Spintronics with multiferroics. *Journal of Physics: Condensed Matter*, 20(43):434221, 2008.

[3] Wilma Eerenstein, ND Mathur, and James F Scott. Multiferroic and magnetoelectric materials. *nature*, 442(7104):759–765, 2006.

[4] Bernard Dennis Cullity and Chad D Graham. *Introduction to magnetic materials*. John Wiley & Sons, 2011.

[5] John Domann, Tao Wu, Tien-Kan Chung, and Greg Carman. Strain-mediated magnetoelectric storage, transmission, and processing: Putting the squeeze on data. *MRS Bulletin*, 43(11):848–853, 2018.

[6] Ralph Skomski, O N Mryasov, J Zhou, and David J Sellmyer. Finite-temperature anisotropy of magnetic alloys. *Journal of applied physics*, 99(8):08E916, 2006.

[7] D Weller, J Stöhr, R Nakajima, A Carl, M G Samant, C Chappert, R Mégy, P Beauvillain, P Veillet, and G A Held. Microscopic origin of magnetic anisotropy in Au/Co/Au probed with X-ray magnetic circular dichroism. *Physical Review Letters*, 75(20):3752, 1995.

[8] S Baumann, F Donati, S Stepanow, S Rusponi, W Paul, S Gangopadhyay, I G Rau, G E Pacchioni, L Gragnaniello, M Pivetta, et al. Origin of perpendicular magnetic anisotropy and large orbital moment in Fe atoms on MgO. *Physical review letters*, 115(23):237202, 2015.

[9] D Weller, Y Wu, J Stöhr, MG Samant, BD Hermsmeier, and C Chappert. Orbital magnetic moments of Co in multilayers with perpendicular magnetic anisotropy. *Physical review B*, 49(18):12888, 1994.

[10] A E Clark and H S Belson. Giant room-temperature magnetostrictions in $TbFe_2$ and $DyFe_2$. *Physical Review B*, 5(9):3642, 1972.

[11] A E Clark, H S Belson, and N Tamagawa. Huge magnetocrystalline anisotropy in cubic rare earth-Fe_2 compounds. *Physics Letters A*, 42(2):160–162, 1972.

[12] A E Clark, H S Belson, and N Tamagawa. Magnetocrystalline anisotropy in cubic rare earth-Fe_2 compounds. In *AIP Conference Proceedings*, volume 10, pages 749–753. American Institute of Physics, 1973.

[13] Mark B Moffett, Arthur E Clark, Marilyn Wun-Fogle, Jan F Lindberg, Joseph P Teter, and Elizabeth A McLaughlin. Characterization of Terfenol-D for magnetostrictive transducers. *The Journal of the Acoustical Society of America*, 87(S1):S95–S95, 1990.

[14] Zhuyun Xiao, Roberto Lo Conte, Cai Chen, Cheng-Yen Liang, Abdon Sepulveda, Jeffrey Bokor, Gregory P Carman, and Robert N Candler. Bi-directional coupling in strain-mediated multiferroic heterostructures with magnetic domains and domain wall motion. *Scientific reports*, 8(1):1–10, 2018.

[15] Mohanchandra K Panduranga, Zhuyun Xiao, Joseph D Schneider, Taehwan Lee, Christoph Klewe, Rajesh Chopdekar, Padraic Shafer, Alpha T N'Diaye, Elke Arenholz, Rob N Candler, et al. Single magnetic domain Terfenol-D microstructures with

passivating oxide layer. *Journal of Magnetism and Magnetic Materials*, page 167798, 2021.

[16] J I Arnaudas, C De La Fuente, M Ciria, L Benito, C Dufour, K Dumesnil, and A Del Moral. Magnetoelastic stresses in epitaxial (110) Terfenol-D thin films. *Journal of magnetism and magnetic materials*, 240(1-3):389–391, 2002.

[17] B T Thole, Paolo Carra, F Sette, and Gerrit van der Laan. X-ray circular dichroism as a probe of orbital magnetization. *Physical review letters*, 68(12):1943, 1992.

[18] Paolo Carra, B T Thole, Massimo Altarelli, and Xindong Wang. X-ray circular dichroism and local magnetic fields. *Physical Review Letters*, 70(5):694, 1993.

[19] J Stöhr. Exploring the microscopic origin of magnetic anisotropies with X-ray magnetic circular dichroism (XMCD) spectroscopy. *Journal of Magnetism and Magnetic Materials*, 200(1-3):470–497, 1999.

[20] Kai Chen, Dieter Lott, Florin Radu, Fadi Choueikani, Edwige Otero, and Philippe Ohresser. Temperature-dependent magnetic properties of ferrimagnetic $DyCo_3$ alloy films. *Physical Review B*, 91(2):024409, 2015.

[21] S Ishio, W Tanaka, and T Miyazaki. Magnetostriction of RCo_3 compounds (R= Pr, Nd, Gd, Tb, Dy). *IEEE translation journal on magnetics in Japan*, 7(10):834–838, 1992.

[22] V Cuartero, Sara Lafuerza, G Subias, Joaquín García, E Schierle, Javier Blasco, and Julia Herrero-Albillos. X-ray magnetic circular dichroism study of the magnetic anisotropy on $TbMnO_3$. *Physical Review B*, 91(16):165111, 2015.

[23] Masakazu Matsubara, Sebastian Manz, Masahito Mochizuki, Teresa Kubacka, Ayato Iyama, Nadir Aliouane, Tsuyoshi Kimura, Steven L Johnson, Dennis Meier, and Manfred Fiebig. Magnetoelectric domain control in multiferroic $TbMnO_3$. *Science*, 348(6239):1112–1115, 2015.

[24] Mohanchandra K Panduranga, Taehwan Lee, Andres Chavez, Sergey V Prikhodko, and Gregory P Carman. Polycrystalline Terfenol-D thin films grown at CMOS compatible temperature. *AIP Advances*, 8(5):056404, 2018.

[25] K P Mohanchandra, S V Prikhodko, K P Wetzlar, W Y Sun, P Nordeen, and G P Carman. Sputter deposited Terfenol-D thin films for multiferroic applications. *Aip Advances*, 5(9):097119, 2015.

[26] Yoshiki Teramura, Arata Tanaka, B T Thole, and Takeo Jo. Effect of Coulomb interaction on the X-ray magnetic circular dichroism spin sum rule in rare earths. *Journal of the Physical Society of Japan*, 65(9):3056–3059, 1996.

[27] Sapana Tripathi. Xmcd investigation at $M_{4,5}$ edges of the rare earth elements in high-performance permanent magnet. 2018.

[28] Heiko Wende. Recent advances in X-ray absorption spectroscopy. *Reports on progress in physics*, 67(12):2105, 2004.

[29] Yoshiki Teramura, Arata Tanaka, and Takeo Jo. Effect of coulomb interaction on the X-ray magnetic circular dichroism spin sum rule in 3d transition elements. *Journal of the Physical Society of Japan*, 65(4):1053–1055, 1996.

[30] Joanna K Kowalska, Brahamjot Nayyar, Julian A Rees, Christine E Schiewer, Sonny C Lee, Julie A Kovacs, Franc Meyer, Thomas Weyhermuller, Edwige Otero, and Serena DeBeer. Iron $L_{2,3}$-edge X-ray absorption and X-ray magnetic circular dichroism studies of molecular iron complexes with relevance to the FeMoco and FeVco active sites of nitrogenase. *Inorganic chemistry*, 56(14):8147–8158, 2017.

[31] P Farber and H Kronmüller. Crystallization behaviour and magnetic properties of highly magnetostrictive Fe–Tb–Dy thin films. *Journal of Magnetism and Magnetic Materials*, 214(3):159–166, 2000.

[32] Göran Engdahl and Isaak D Mayergoyz. *Handbook of giant magnetostrictive materials*, volume 107. Elsevier, 2000.

[33] M A Laguna-Marco, Jesús Chaboy, and Cristina Piquer. Experimental determination of the R(5d)- T(3d) hybridization in rare-earth intermetallics. *Physical Review B*, 77(12):125132, 2008.

[34] D M Eagles. Models for the heavy rare earth metals and (rare earth) Fe2 compounds involving 5d and 6s electrons. *Physik der kondensierten Materie*, 16(3):181–199, 1973.

[35] Claire Arnoult and Simon Gerstenkorn. Experimental and theoretical hyperfine structure of low-lying levels of terbium $4f^8 5d6s^2$ configuration; quadrupole moment of ^{159}Tb. *JOSA*, 56(2):177–181, 1966.

[36] A Scherz, H Wende, C Sorg, K Baberschke, J Minr, D Benea, and H Ebert. Limitations of integral XMCD sum-rules for the early 3d elements. *Physica Scripta*, 2005(T115):586, 2005.

[37] H Wende, A Scherz, C Sorg, K Baberschke, EKU Gross, H Appel, K Burke, J Minár, H Ebert, AL Ankudinov, et al. XMCD analysis beyond standard procedures. In *AIP Conference Proceedings*, volume 882, pages 78–82. American Institute of Physics, 2007.

[38] Cinthia Piamonteze, Piter Miedema, and Frank MF De Groot. Accuracy of the spin sum rule in XMCD for the transition-metal L edges from manganese to copper. *Physical Review B*, 80(18):184410, 2009.

[39] Xiaoxiao Fu, Bénédicte Warot-Fonrose, Rémi Arras, K Dumesnil, and Virginie Serin. Quantitative moment study and coupling of 4f rare earth and 3d metal by transmitted electrons. *Physical Review B*, 94(14):140416, 2016.

[40] J B Goedkoop, N B Brookes, Michel van Veenendaal, and B T Thole. Soft X-ray fluores-

cence yield XMCD sum rules. *Journal of electron spectroscopy and related phenomena*, 86(1-3):143–150, 1997.

[41] Mona Mouallem-Bahout, Octavio Peña, Dionisio Gutierrez, Pedro Duran, and Carlos Moure. Peculiar magnetic properties of (Dy, Ca)MnO_3. *Solid state communications*, 122(10):561–564, 2002.

[42] S Baran, D Kaczorowski, D Sheptyakov, and A Szytuła. Magnetic ordering in DyRhSn. *Journal of magnetism and magnetic materials*, 296(2):89–93, 2006.

[43] E Talik, M Kulpa, T Mydlarz, J Kusz, and H Böhm. Magnetic properties of $DyMn_2$ single crystals. *Journal of alloys and compounds*, 308(1-2):30–37, 2000.

[44] RL Cohen. Mössbauer effect in Dy^{160}. *Physical Review*, 137(6A):A1809, 1965.

[45] A E Clark, R Abbundi, and W R Gillmor. Magnetization and magnetic anisotropy of $TbFe_2$, $DyFe_2$, $Tb_{0.27}$ $Dy_{0.73}Fe_2$ and $TmFe_2$. *IEEE Transactions on Magnetics*, 14(5):542–544, 1978.

[46] H Lassri, R Krishnan, and M Baran. Magnetisation studies in Tb-Fe/Pt single and multilayers. *Journal of magnetism and magnetic materials*, 153(1-2):5–10, 1996.

[47] B Barbara, J P Giraud, J Laforest, R Lemaire, E Siaud, and J Schweizer. Spontaneous magnetoelastic distortion in some rare earth-iron laves phases. *Physica B+ C*, 86:155–157, 1977.

[48] T F Retajczyk Jr and A K Sinha. Elastic stiffness and thermal expansion coefficients of various refractory silicides and silicon nitride films. *Thin Solid Films*, 70(2):241–247, 1980.

[49] T Kozawa, T Kachi, H Kano, H Nagase, N Koide, and K Manabe. Thermal stress in GaN epitaxial layers grown on sapphire substrates. *Journal of applied physics*, 77(9):4389–4392, 1995.

[50] M Al-Jiboory and D G Lord. Study of the magnetostrictive distortion in single crystal Terfenol-D by X-ray diffraction. *IEEE transactions on magnetics*, 26(5):2583–2585, 1990.

[51] LARS Sandlund, MIRKA Fahlander, TORD Cedell, A E Clark, J B Restorff, and M Wun-Fogle. Magnetostriction, elastic moduli, and coupling factors of composite Terfenol-D. *Journal of Applied Physics*, 75(10):5656–5658, 1994.

[52] X J Zheng and X E Liu. A nonlinear constitutive model for Terfenol-D rods. *Journal of applied physics*, 97(5):053901, 2005.

[53] T A Duenas and G P Carman. Large magnetostrictive response of Terfenol-D resin composites. *Journal of Applied Physics*, 87(9):4696–4701, 2000.

[54] A Mougin, C Dufour, K Dumesnil, and P h Mangin. Strain-induced magnetic anisotropy in single-crystal RFe_2 (110) thin films (R= Dy, Er, Tb, $Dy_{0.7}Tb_{0.3}$, Sm, Y). *Physical Review B*, 62(14):9517, 2000.

[55] Christopher E Patrick, George A Marchant, and Julie B Staunton. Spin orientation and magnetostriction of $Tb_{1-x}Dy_xFe_2$ from first principles. *Physical Review Applied*, 14(1):014091, 2020.

[56] J Rhyne and T McGuire. Magnetism of rare-earth elements, alloys, and compounds. *IEEE Transactions on Magnetics*, 8(1):105–130, 1972.

[57] C De la Fuente, J I Arnaudas, L Benito, M Ciria, A Del Moral, C Dufour, and K Dumesnil. Magnetocrystalline anisotropy in a (110) $(Tb_{0.27}Dy_{0.73})Fe_2$ thin-film. *Journal of Physics: Condensed Matter*, 16(17):2959, 2004.

Chapter 5

Magnetic Moment Enhancements in Exchange-Coupled Multilayers

5.1 Introduction

Multilayers consisting of amorphous rare-earth transition metal (RE-TM) alloys and antiparallelly exchange coupled nanocrystalline transition metals (TMs) have been studied due to their superior magnetic properties such as decreased damping, lower saturation and coercive fields, and enhanced magnetostriction as contrasted to their intrinsic monolithic layers. These property improvements originate from magnetic interactions at the interfaces due to competing anisotropic energies (e.g. exchange, magnetoelastic, perpendicular, etc.) producing localized magnetic order/disorder in the RE-TM layers [1, 2, 3]. Due to the material complexity as well as access to sophisticated measurement systems, focused studies on RE-TM/TM multilayers have been limited in developing a more complete understanding of the underlying physics governing these property enhancements. Therefore, closer examination of the local interactions are warranted to better understand and subsequently design future

multilayered RE-TM/TM heterostructures with specific property improvements.

Experimental work and micromagnetic simulations on RE-TM/TM multilayers have shown improvements in magnetostriction and reduced coercive fields compared to their monolithic thin film counterparts [4, 5]. In amorphous $Tb_{41}Fe_{59}/Fe_{83}Al_{17}$ multilayers, interface interactions including localized interlayer stresses reduced the coercive field by 50% while retaining similar magnetostriction as monolithic $TbFe_2$ films [6]. In a related study conducted on $TbFe_2$/Co multilayers, researchers demonstrated the field to reach magnetic saturation was reduced by 38% [7] through a reported exchange interaction at the interface. In $TbFe_2/Fe_3Ga$ multilayers, coercive fields smaller than either of the monolithic films were reported by maximizing the antiparallel exchange coupling between layers [8], which was more recently attributed to the competition between antiferromagnetic (i.e. antiparallel) exchange and domain wall energies present at the interfaces [9]. In all of these studies, the property enhancements originated from spin-spin interactions and spin-orbit coupling [10] and require additional studies at spin and orbital moment levels to better understand the underlying sources leading to these property improvements.

X-ray absorption (XAS) and X-ray magnetic circular dichroism (XMCD) offers a sophisticated approach to study element specific magnetic behavior in layered magnetic structures [11, 12]. In this space, several investigations have been performed on RE-TM/TM bilayers with relatively few studying multilayers. In $TbFe_2$/Co bilayers, elemental XMCD intensities were directly correlated to the degree of moment canting to study interface interactions between in and out-of-plane energies with variations in Co thickness [13] and Tb composition (i.e. Tb_xFe_{1-x} x=0.15, 0.27, & 0.34) [14]. These studies demonstrated by decreasing Co thickness and increasing Tb content, the out-of-plane anisotropic energy at the interfaces becomes dominant. More recent XMCD investigations on Gd/Fe multilayers utilized spectral intensity measurements to measure the extent of magnetic ordering in the Gd layer [15, 16]. Furthermore, XMCD sum rule calculations for magnetically ordered Gd/Fe multi-

layers concluded that neither the spin nor orbital moment of Gd increased near the interfaces, signifying that both stronger exchange coupling and magnetic ordering do not necessarily produce increased RE moments [17, 18, 19, 20]. This finding raises concerns if interface mediated interactions in ordered exchange coupled RE/TM and RE-TM/TM systems increase RE moments or only modulate interfacial energies, suggesting that alternative more complex interfacial interactions may cause RE moment enhancements. Therefore, closer examination is required to better understand how the individual elemental spin and orbital moments contribute to enhancing magnetic properties.

5.2 Experimental Setup

Four thin film samples consisting of 1) 40 nm $TbFe_2$, 2) 40 nm $Ni_{81}Fe_{19}$, 3) 10 layers of [(2nm) $TbFe_2$/(4nm) $Ni_{81}Fe_{19}$ = 33% $TbFe_2$] and 4) 10 layers of [(4nm) $TbFe_2$/(2nm) $Ni_{81}Fe_{19}$ = 67% $TbFe_2$] were prepared by ultra-high vacuum magnetron sputtering. The thin film samples were deposited using alloy targets of $TbFe_2$ and or $Ni_{81}Fe_{19}$ onto 2-inch diameter c-plane Al_2O_3 wafers with a 5 nm Ta barrier layer. The $Ni_{81}Fe_{19}$ layers were deposited using 180 W of power and an argon working pressure of 1.8 mTorr while the $TbFe_2$ layers were deposited using a sputtering power of 220 W and an argon working pressure of 1.8 mTorr. All four films were deposited at a base pressure of 5×10^{-7} Torr. Following all thin film depositions, a 5 nm Ta capping layer was deposited in-situ under-vacuum to prevent oxidation. X-ray diffraction (XRD) results show all $Ni_{81}Fe_{19}$ thin films were nanocrystalline while all $TbFe_2$ films were amorphous. The in-plane magnetization curves (M-H curves) were measured by sweeping the applied magnetic field between -6 kOe to 6 kOe using a Scanning Quantum Interference Device (SQUID) at room temperature.

XAS and XMCD were performed using beamline 6.3.1 at the Advanced Light Source (ALS) of the Lawrence Berkley National Laboratory (LBNL). The samples were mounted onto a

luminescence sample holder and measured in luminescence yield (LY) mode probing the entire depth of the samples. The angle between the incident X-ray beam and the normal of the film surface was fixed at 60. The Fe and Ni $L_{2,3}$ edges were determined by sweeping the energy between 700-740 eV and 840-880 eV for Fe and Ni respectively, while the Tb $M_{4,5}$ edges were determined by sweeping the energy between 1220-1280 eV. The XAS scans were conducted by sweeping the energy while saturating the samples at 5 kOe (μ^+) and -5 kOe (μ) respectively to determine the XMCD ($\Delta\mu = \mu^+ - \mu^-$). Each scan was repeated 8 times and normalized by a reference signal of the incoming beam intensity measured on a gold mesh to exclude any time-dependent scanning errors. The magnitude of the elemental spin and orbital moments were derived from the XMCD sum rules (see chapter 2). The element specific M-H curves were determined by holding the photon energy constant at the characteristic edge energies and measuring the XMCD signal while sweeping the magnetic field from – 2 kOe to 2 kOe. Here the applied magnetic field is canted at an angle of 60angle with the sample normal which is different from the SQUID in-plane measurements.

5.3 Results & Discussion

Figure 1 shows the in-plane SQUID M-H curves for the crystalline $Ni_{81}Fe_{19}$, amorphous $TbFe_2$, and the two x=33% x=67% $TbFe_2$ multilayers with an inset providing a magnified image from -40 Oe to 40 Oe. The $Ni_{81}Fe_{19}$ sample shows soft ferromagnetic properties with a coercive field of 7 Oe, saturation magnetization $M_s = 964$ emu/cc, and a magnetic remanence M_r =920 emu/cc consistent with published values [21]. The $TbFe_2$ film shows hard magnetic behavior with a relative permeability of 1.22 which has been previously observed in slightly Fe rich (i.e. $TbFe_x$ x¿2) as-deposited amorphous films [22]. $TbFe_2$ films which are amorphous have been reported with sperrimagnetic ordering (i.e. randomized ferrimagnetic ordering) as opposed to ferrimagnetic ordering causing disorder across the magnetic moments [23, 24].

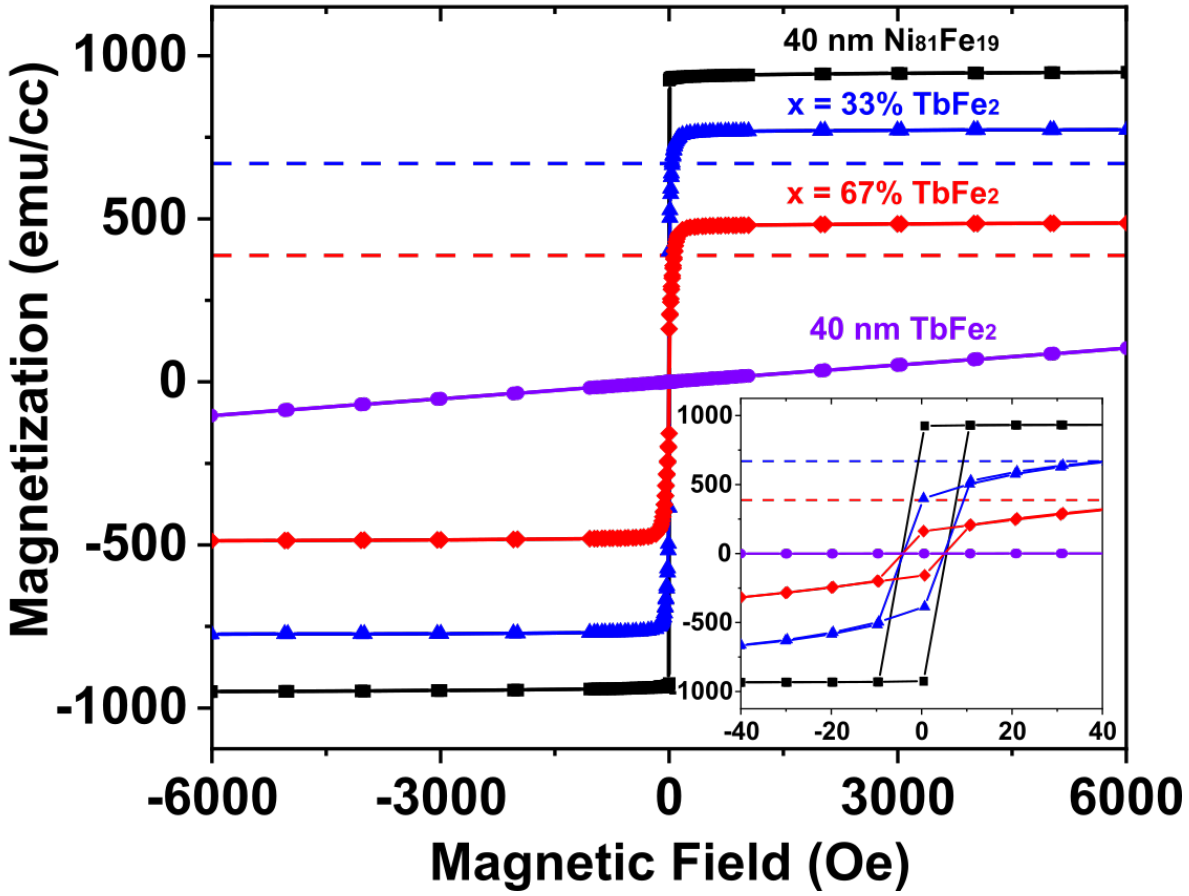

Figure 5.1: M-H curves of the crystalline $Ni_{81}Fe_{19}$, amorphous $TbFe_2$, and the two $Ni_{81}Fe_{19}$ /$TbFe_2$ multilayers. The dashed lines below the multilayers show their expected saturation magnetization (M_s) based on the rule of mixtures (RoM).

The magnetic responses of the x=33% and x=67% $TbFe_2$ multilayers are similar to a soft ferromagnetic material with an M_s = 773 emu/cc and 486 emu/cc and M_r = 362 emu/cc and 147 emu/cc respectively, with coercive fields of 7 Oe for both samples. The two dashed lines in Figure 5.1 represent the M_s calculated using a rule of mixtures (RoM) approach given by $M_s(x) = (1-x)M_s^{NiFe} + xM_s^{TbFe}$, where x is the $TbFe_2$ volume fraction and M_s^{NiFe} and M_s^{TbFe} are the magnetization values at 6 kOe. When compared to the RoM approach, the multilayers show an M_s enhancement which is attributed to exchange coupling present at the interface, reorienting more $TbFe_2$ magnetic moments which is later confirmed in this

manuscript with XMCD generated data.

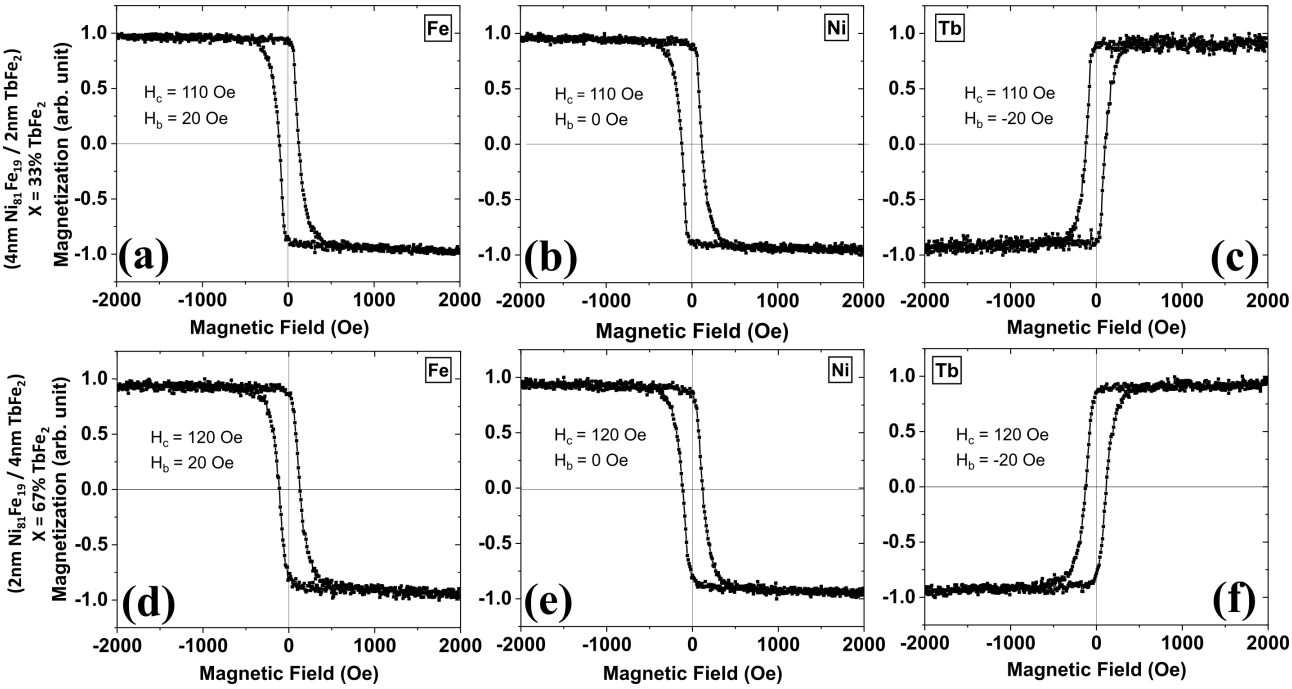

Figure 5.2: Elemental M-H curves performed by XMCD with the magnetic field applied at 60with the sample normal . Multilayer composition of x=33% $TbFe_2$ (a) Fe (b) Ni (c) Tb and multilayer composition of x=67% $TbFe_2$ (d) Fe (e) Ni (f) Tb.

Figures 5.2(a-c) show the XMCD generated elemental (Fe, Ni, and Tb) M-H curves for x=33% $TbFe_2$ while Figures 5.2(d-f) provide similar data for the x=67% $TbFe_2$ multilayer. Figure 5.2 shows that in both samples, the Fe and Ni magnetic moments (a/b & d/e) are antiparallel with the Tb moment in the elemental M-H curves (c & f). For x=33% $TbFe_2$ in Figures 5.2(a-c), the coercive fields are 110 Oe while the coercive fields are 120 Oe for x=67% $TbFe_2$ in Figures 5.2(d-f). The relatively higher coercive field for x=67% $TbFe_2$ is attributed to the higher volume fraction of $TbFe_2$. Additionally, the XMCD measured coercive fields are larger than the SQUID measurements (Figure 5.1) due to the application of the magnetic field in the XAS/XMCD measurement was performed at a 60angle with the sample normal (i.e. SQUID is at 90angle) where contributions from the shape anisotropy towards the coercive responses become noticeable. Surprisingly, Figures 5.2(c/f) show that the Tb element present in the multilayers reorients and appears to saturate with a moderate

magnetic field. This was not observed in the elemental M-H curve for Tb in the 40 nm $TbFe_2$ monolithic sample nor in the SQUID measurement (Figure 5.1). This suggests that the Tb in the multilayers are strongly influenced by the adjacent $Ni_{81}Fe_{19}$ layers. Furthermore, Figure 5.2 shows both multilayer samples contain an exchange bias field (H_b) of 20 Oe for Fe (Figure 5.2 a/d) and a -20 Oe exchange bias field for Tb (Figures 5.2 c/f) while there Ni is an absent of an exchange bias field (Figures 5.2 b/e). While not presented here, an exchange bias field was unobservable in the XMCD results for the monolithic $TbFe_2$ or $Ni_{81}Fe_{19}$ samples and an exchange bias was not observed in any of the samples measured in SQUID which could be due to the relatively small coercive field (i.e. 7 Oe). These results (i.e. Tb magnetized along with an exchange bias) suggests that an interlayer exchange coupling exists between the disordered Tb in $TbFe_2$ and the ordered Fe moments in $Ni_{81}Fe_{19}$.

Figure 5.3(a) plots the XMCD measured average spin, average orbital, and average total (spin+orbital) moments versus the volume percent of $TbFe_2$ in each sample (see chapter 2 for more details). Note that three of the orbital moment values in Figure 5.3(a) are intrinsically opposing the sample's net moment (i.e. negative) and are presented as absolute values with half-shaded pentagons. Additionally, the total moments of all the samples are calculated on an average per atom basis and cannot be directly compared to the M_s values measured by SQUID in Figure 5.1 without factoring in the atomic packing density. Figure 5.3(a) shows the average total magnetic moment remains relatively constant for x=0% & x=33% but dramatically decreases for x=67% & 100% $TbFe_2$. Furthermore, the data shows that spin angular momentum is the major contributor toward the total magnetic moment as expected and is also larger than the total magnetic moment for x=33%, 67% & 100% $TbFe_2$. Finally, there is a notable increase in the orbital moment for x=67% which is larger than all samples suggesting the exchange interaction in x=67% $TbFe_2$ is greater than x=33% $TbFe_2$. To better understand these trends, we break down the magnetic moment of each element in terms of their total, spin, and orbital moments and review these contributions individually.

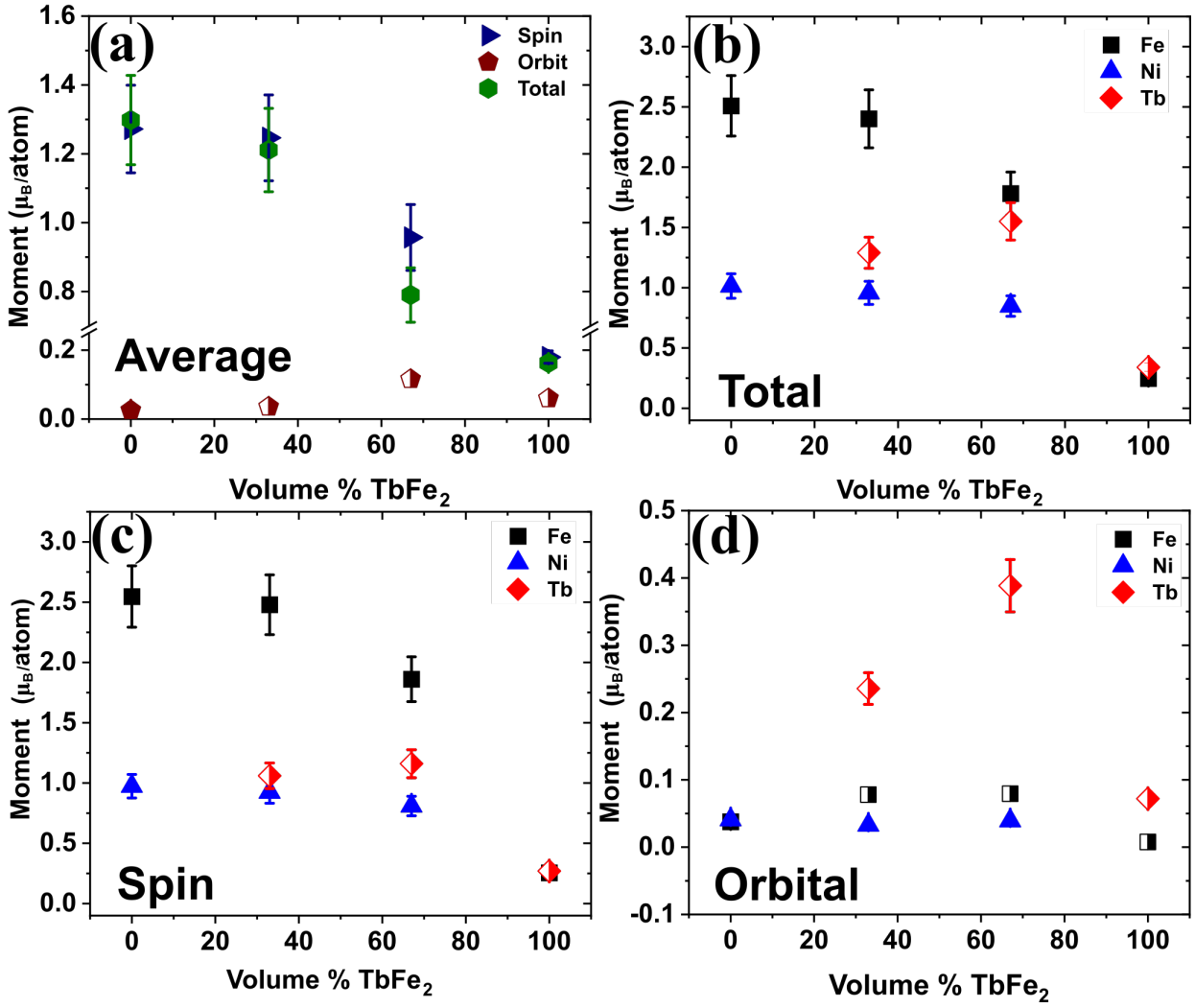

Figure 5.3: (a) Average moment of multilayers denoted by the average spin, orbital, and total (spin+orbital) moments. (b) Total moment (c) Spin moment (d) Orbital moment versus the volume percent $TbFe_2$. The half-shaded-in shapes indicate the absolute value of negative values measured for some moments.

Figures 5.3(b-d) plots the elemental (Fe, Ni, Tb) total (Figure 5.3b), spin (Figure 5.3c), and orbital (Figure 5.3d) moments versus the $TbFe_2$ volume percent for each sample. For all three figures, the Tb moments are intrinsically opposing Fe, Ni, and the net moment, and for all plots their absolute values are presented by half-shaded diamond shapes. Figure 5.3(b) (total magnetic moment) shows that Fe possesses the largest magnetic moment in all samples with the exception of x=100% $TbFe_2$. In comparison, the Ni element contributes

the least in samples containing $Ni_{81}Fe_{19}$ and remains relatively constant despite changes in the $TbFe_2$ volume percent. This suggests that Ni is independent of the coupling with the $TbFe_2$ layers which is supported by the absence of an exchange bias field for Ni in Figures 5.2(b/e). Finally, the large peak in the Tb moment at x=67% $TbFe_2$ is close in magnitude to Fe moment (i.e. 1.6 μ_B/atom vs. 1.8 μ_B/atom). This suggests the presence of stronger coupling between these elements in x=67% $TbFe_2$ with the statement supported by the larger orbital moment observed in Figure 5.3(a). Finally, the total moment of Tb and Fe in x=100% $TbFe_2$ are of similar magnitude supporting the argument that the $TbFe_2$ sample is sperimagnetic (i.e contains randomized ferrimagnetic ordering).

Figure 5.3(c) provides spin magnetic moment data for each element versus the volume percent $TbFe_2$. The Fe and Ni spin moments largely mirror their total moments (Figure 5.3(b)) attributed to the relatively small orbital moments of $3d$ elements. Similarly, the Tb spin moment follows similar trends to those observed for the total moment in Figure 5.3(b) but the magnitudes have decreased only slightly owing to the large orbital moment of $4f$ elements. In regard to x=67% $TbFe_2$ in Figure 5.3(c), the Fe and Tb spin moments reduce and increase respectively similar to their total moments in Figure 5.3(b), implying stronger interlayer exchange coupling between the Fe in $Ni_{81}Fe_{19}$ and the Tb in $TbFe_2$ is present in this particular multilayer. As a result, it is important to analyze the orbital moment data for more information regarding the outcomes of the potentially stronger exchange coupling in x=67% $TbFe_2$ compared to x=33% $TbFe_2$.

Figure 5.3(d) shows the elemental orbital magnetic moments for Fe, Ni, and Tb. As one can see for x=0% $TbFe_2$ (i.e. monolithic $Ni_{81}Fe_{19}$), the Fe orbital moment is parallel to the Ni orbital moment. However, for all other samples the Fe orbital moment is antiparallel to the Ni orbital moment, parallel to the Tb orbital moment, and increases in magnitude with increasing $TbFe_2$ content below x=100% $TbFe_2$ due to the RE($5d$)-TM($3d$) electron hybridization present in $TbFe_2$ [25, 26, 27]. This suggests that the antiparallel Fe orbital

moment in the $TbFe_2$ layers are larger than the parallel Fe orbital moment in the $Ni_{81}Fe_{19}$ and dominate the measured Fe orbital response in the multilayers. Additionally, the Fe orbital moments in the multilayers are larger than either of the two monolithic films (x=0% & x=100% $TbFe_2$), and the Tb orbital moments in the multilayers are larger than the Tb orbital moment in x=100% $TbFe_2$. The combined data in Figures 5.3(b-d) strongly indicates that the interlayer exchange coupling between the ordered Fe in the $Ni_{81}Fe_{19}$ layers and the disordered Tb in the $TbFe_2$ causes magnetic ordering of the Tb and Fe moments at or near the $TbFe_2$ interfaces. As a result of the magnetic ordering of both Tb and Fe in the $TbFe_2$ layers, larger moments are obtained in the $TbFe_2$ layers which are responsible for the M_s enhancements observed in the SQUID data for the multilayers presented in Figure 5.1. The origin of the increases in the Tb orbital moment by the interlayer exchange coupling can be understood from the overlap of the Tb($5d$) and the Fe($3d$) (in $Ni_{81}Fe_{19}$) orbitals [28, 29] which influence the Tb($4f$) orbitals through the Tb($5d$)-Tb($4f$) hybridization of $TbFe_2$ [26, 25].

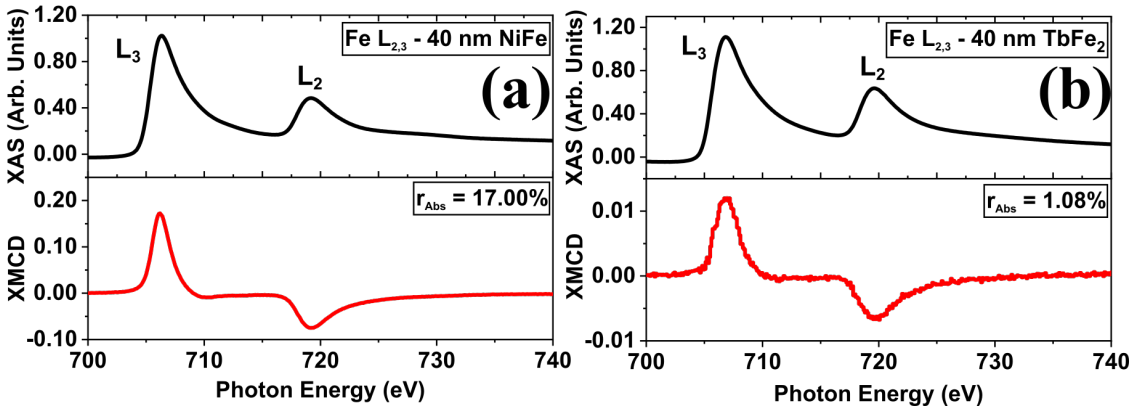

Figure 5.4: Average XAS ($\mu_0 = \mu^+ + \mu^-$) & XMCD absorption spectra & XMCD absorption spectra of Fe $L_{2,3}$ edges in (a) 40 nm $Ni_{81}Fe_{19}$ x=0% $TbFe_2$ and (b) in 40 nm $TbFe_2$. x=100% $TbFe_2$.

The magnetic ordering depth in the $TbFe_2$ layers of the multilayers can be determined using the experimental XMCD and XAS spectra. In the previous chapters, it was explicitly demonstrated how the XMCD absorption spectra correlate to the magnetic moment (i.e. magnetization) in both 3d & 4f elements. During the XMCD measurements, a magnetic field

is applied to saturate moments and measure the XAS spectra accordingly. If the applied field during measurement fully saturates the moments (determined by the material's the M-H curve) at the applied field, a dimensionless ordering parameter can be determined by dividing the XMCD peak intensity by the XAS peak intensity at the respective absorption edge of the element referred to as the relative absorption intensity (r_{abs}) [**?**]. Similarly, a dimensionless disorder parameter for an element can be determined using the sample's (r_{abs}) if the same magnetic field in magnitude was applied during the XMCD measurement but did not saturate the sample in the M-H curve.

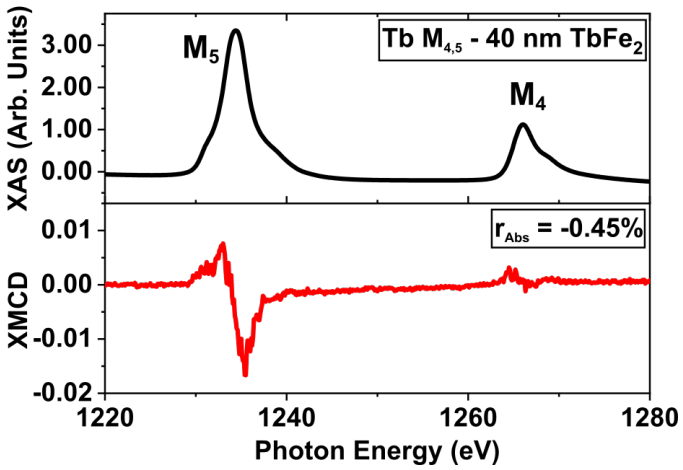

Figure 5.5: Average XAS ($\mu_0 = \mu^+ + \mu^-$) & XMCD absorption spectra of Tb $M_{4,5}$ edges in 40 nm $TbFe_2$ x=100% $TbFe_2$.

Recall that in this work, the magnetic fields applied during all XAS/XMCD spectroscopy were ± 5 kOe, for which complete saturation in the monolithic (i.e. 40 nm) $Ni_{81}Fe_{19}$ film was determined in Figure 1 in the manuscript, whereas the monolithic $TbFe_2$ film was not saturated at the similar 5 kOe field. Moreover, Fe is the element in common between the two samples and using the the XAS/XMCD absorption spectra of the Fe in $Ni_{81}Fe_{19}$ and Fe in the $TbFe_2$ at the $L_{2,3}$, a dimensionless order and disorder parameter can be respectively determined for Fe. As shown in Figure 5.4(a), the dimensionless Fe order parameter (Fe_o) is given by the r_{abs} 17% by dividing the Fe XMCD L_3 peak intensity by the average XAS L_3 peak intensity. Similarly, the dimensionless Fe disorder parameter (Fe_d) is given by the

r_{abs} measured as 1.08% in Figure 5.4(b). Therefore, the ordering depth of an element in a layered heterostructure can be determined by equation 5.1

$$(d_i - I_i\alpha_i)A_d + (I_i\alpha_i)A_o = d_iA_i \tag{5.1}$$

where d_i is the total thickness of the element present in the structure, I_i is the number of interfaces, α_i is the magnetic ordering depth with length units, A_d is the r_{abs} taken of the element in a disordered sample, A_o is the r_{abs} taken of the element in an ordered sample, and A_i is r_{abs} of the element of interest in the layered heterostructure. However, using the Fe ordering parameters does not directly provide the correct ordering depth in the $TbFe_2$ layers as the Fe absorption spectra are measured from both $Ni_{81}Fe_{19}$ and $TbFe_2$ layers in the multilayers. Therefore, an order and disorder parameter for Tb must be used inplace of Fe, as it is the element which exists only in the disordered $TbFe_2$ layers.

Figure 5.5 shows the average XAS and XMCD spectra 40 nm Tb $M_{4,5}$ edges. The Tb disorder parameter (Tb_d) can be determined from Tb using the r_{abs} this sample measured at -0.45%. However, a Tb order parameter cannot be directly determined as a sample referencing completely ordered Tb was not available in this study. Therefore, a Tb ordering parametering is needed in order to determine the magnetic ordering depth in the $TbFe_2$ layers. If the ratio of disorderd Fe to disordered Tb in the $TbFe_2$ sample is governed by the exchange interaction between the two elements, then it can also be assumed that if Tb were to be ordered it would still be governed by the same exchange interaction. Therefore, the

Tb order parameter Tb_o can be determined from the relationship in equation 5.2

$$Tb_o = \frac{Fe_o Tb_d}{Fe_d} = -7.08\% \tag{5.2}$$

where Fe_0 and Fe_d are the Fe order and disorder parameters respectively, and Tb_d is the Tb disorder parameter. Figure 5.6 shows the Tb $M_{4,5}$ edges in (a) [4 nm $Ni_{81}Fe_{19}$/ 2 nm $TbFe_2$] x=33% $TbFe_2$ and (b) in [2 nm $Ni_{81}Fe_{19}$/ 4nm $TbFe_2$] x=67% $TbFe_2$ respectively. Similarly, dividing the XMCD peak intensity by the XAS peak intensity at the M_5 edges gives the degree of ordering in the $TbFe_2$ layers from the two different samples. With these parameters, the magnetic ordering depths can be determined for the x=33% and x=67% $TbFe_2$ multilayers using equations 5.3 and 5.4 respectively.

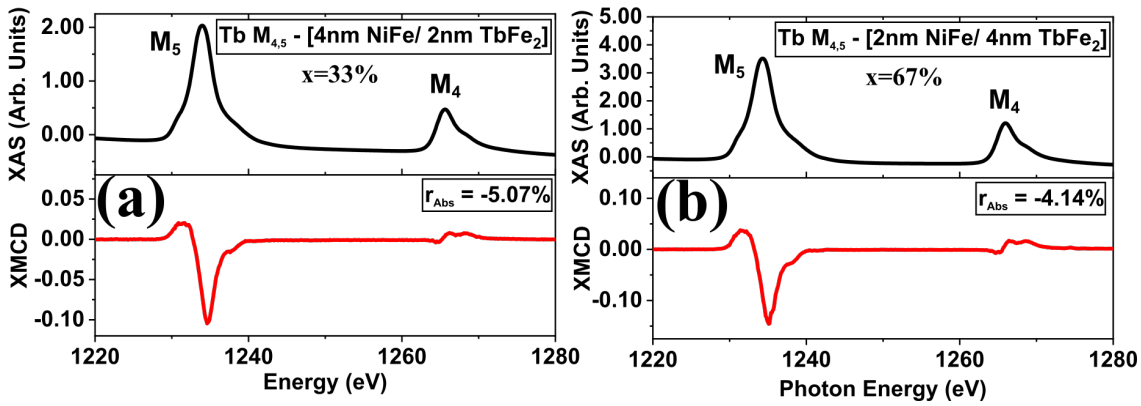

Figure 5.6: Average XAS ($\mu_0 = \mu^+ + \mu^-$) & XMCD absorption spectra of Tb $M_{4,5}$ edges in (a) [4 nm $Ni_{81}Fe_{19}$/ 2 nm $TbFe_2$] x=33% $TbFe_2$ and (b) in [2 nm $Ni_{81}Fe_{19}$/ 4nm $TbFe_2$] x=67% $TbFe_2$.

$$(20 - 19\alpha_{33})Tb_d + (19\alpha_{33})Tb_o = 20Tb_{33} \tag{5.3}$$

$$(40 - 19\alpha_{67})Tb_d + (19\alpha_{67})Tb_o = 40Tb_{67} \tag{5.4}$$

In equations 5.3 and 5.4, Tb_{33} and Tb_{67} are the relative absorption intensities (r_{abs}) taken from Figures 5.6(a) and 5.6(b) respectively, and α_{33} and α_{67} are the magnetic ordering lengths for the x=33% and x=67% $TbFe_2$ multilayers respectively. Referring back to equation 5.1, there are 10 repeating units in both multilayers meaning there are 19 interfaces such that $I_i = 19$. For x=33% $TbFe_2$, there are 20 nm total of $TbFe_2$ that can be magnetically ordered meaning $d_{33} = 20\ nm$ as shown in equation 5.3. On the otherhand, there is more available thickness at 40 nm ($d_{67} = 40\ nm$) reflected in equation 5.4. Rearranging equations 5.3 and 5.4 and solving for the ordering depths α_{33} and α_{67} are given as follows.

$$\alpha_{33} = (\frac{20}{19})\frac{Tb_{33} - Tb_d}{Tb_0 - Tb_d} = (\frac{20}{19})\frac{-5.07 + 0.45}{-7.08 + 0.45} = 0.73\ nm \tag{5.5}$$

$$\alpha_{67} = (\frac{40}{19})\frac{Tb_{67} - Tb_d}{Tb_0 - Tb_d} = (\frac{40}{19})\frac{-4.14 + 0.45}{-7.08 + 0.45} = 1.17\ nm \tag{5.6}$$

Figure 5.7 shows an illustration of the elemental total magnetic moment alignment for a single repeating unit of the (a) x=33% and (b) x=67% $TbFe_2$ multilayers under a 5 kOe field. This illustration is based on the data presented in Figure 5.2 which focuses on the orientation of the total magnetic moments. The arrows in the figure illustrate each atom's total magnetic moment direction, and as one can see the depth of orientation and magnetic ordering at the $TbFe_2$ interfaces are slightly different for the two samples. The ordering

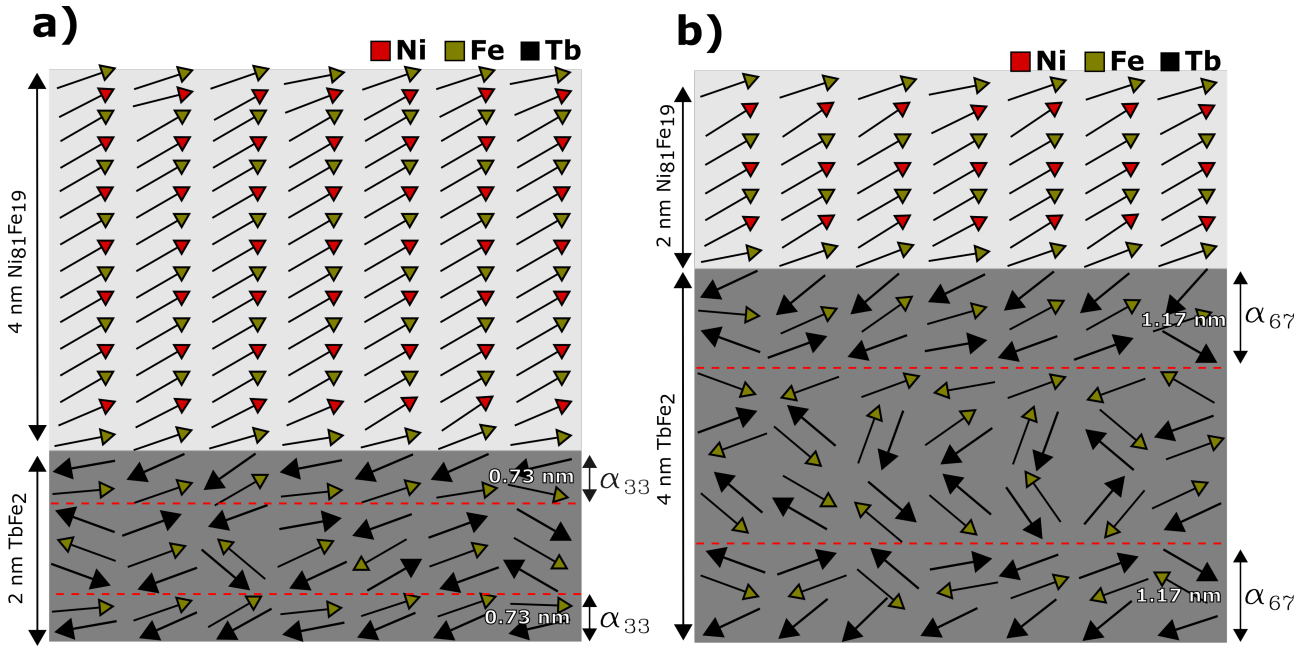

Figure 5.7: Representation of the moment behavior and ordering depth for one repeating unit of the (a) x=33% and (b) x=67% $TbFe_2$ multilayers saturated at 5 kOe based on the data presented in Figure 5.2.

depths (i.e. α_{33} & α_{67}) in the figure were calculated from the XAS and XMCD absorption spectra as shown above. The ordering depth is defined as the distance from the interfaces where the Tb and Fe atoms in the $TbFe_2$ layers are exchange coupled with the adjacent $Ni_{81}Fe_{19}$ layers and reorient with the applied field due to exchange coupling. The ordering depths of x=33% and x=67% $TbFe_2$ are 0.73 nm and 1.17 nm respectively and represented in the figure. Additionally, the regions outside these ordered regions are referred to as the disordered $TbFe_2$ regions with magnetic properties similar to the x=100% $TbFe_2$ film.

As can be seen in Figure 5.7, the ordering lengths show $\alpha_{67} > \alpha_{33}$, although x=33% $TbFe_2$ contains more $Ni_{81}Fe_{19}$ per volume (i.e. per thickness). This indicates that the exchange bias strength and ordering depths are independent of the $Ni_{81}Fe_{19}$ layer thickness even for these fairly thin films (i.e. 2 & 4 nm thick). Additionally, referring back to Figure 5.2, the measured exchange bias field was determined to be $H_b = \pm 20$ Oe between Tb and Fe in both multilayers. This implies that the different ordering depths are due to the $TbFe_2$ layer thickness in the multilayers rather than intrinsic differences in exchange bias strengths.

For thicker $TbFe_2$ layers (i.e. x=67% compared to x=33% $TbFe_2$), the exchange bias at one interface (top) gradually becomes more decoupled from the other interface (bottom). Therefore, with increasing $TbFe_2$ layer thickness, one would expect a diminishing trend in the competing interactions between the two adjacent interfaces in a single $TbFe_2$ layer producing larger depths of ordered moments, i.e. $\alpha_{67} > \alpha_{33}$. However, these remarks only hold true for ultra-thin layers studied in this manuscript. With increasing layer thickness, eventually a critical thickness should be reached where the two interactions are eliminated, and the ordering depth plateaus to a maximum value. These results clearly show the impact that exchange coupling has on these multilayer samples and may provide information important for designing new softer or harder magnetic materials via exchange coupling as well as an understanding of the contributions from spin and orbital moments to this phenomenon.

5.4 Conclusion

SQUID magnetometry revealed magnetization enhancements in two distinct $TbFe_2/Ni_{81}Fe_{19}$ (2nm/4nm or 4nm/2nm) multilayers compared to predictions from a rule-of-mixtures model. Elementwise XMCD results indicated these enhancements are caused by interface mediated antiparallel exchange coupling between Tb in the $TbFe_2$ and Fe in the $Ni_{81}Fe_{19}$. XMCD M-H curves demonstrated this coupling is sufficient to provide pronounced saturation and reorientation in the Tb orbital and spin moments with coercive fields equal to monolithic $Ni_{81}Fe_{19}$ at or near the interfaces. XMCD spectroscopy showed increased magnetic ordering lengths within $TbFe_2$ layers as the $TbFe_2$ layer thicknesses are increased due to less interference between the two competing interactions at the opposing (i.e. top bottom) $TbFe_2$ layer interfaces. These results provide important information and an alternative pathway for investigating and understanding the influence of various elemental-level interactions at the spin and orbital moment level in RE-TM/TM multilayers with the intent of creating

superior layered magnetic heterostructures.

Chapter References

[1] Colin R Rementer, Kevin Fitzell, Qiang Xu, Paul Nordeen, Gregory P Carman, Yuanxun E Wang, and Jane P Chang. Tuning static and dynamic properties of FeGa/NiFe heterostructures. *Applied Physics Letters*, 110(24):242403, 2017.

[2] IA Subbotin, EM Pashaev, AL Vasiliev, Yu M Chesnokov, GV Prutskov, EA Kravtsov, MV Makarova, VV Proglyado, and VV Ustinov. The influence of microstructure on perpendicular magnetic anisotropy in Co/Dy periodic multilayer systems. *Physica B: Condensed Matter*, 573:28–35, 2019.

[3] ZS Shan and David J Sellmyer. Magnetism of rare-earth–transition-metal nanoscale multilayers. I. experiments on Dy/Co, Dy/Fe, and Tb/Fe. *Physical Review B*, 42(16):10433, 1990.

[4] J Juraszek, A Grenier, J Teillet, N Tiercelin, F Petit, J Ben Youssef, and M Toulemonde. Swift ion irradiation of magnetostrictive multilayers. *Nuclear Instruments and Methods in Physics Research Section B: Beam Interactions with Materials and Atoms*, 245(1):157–160, 2006.

[5] F Petit, J Juraszek, J Ben Youssef, J Teillet, DT Dekadjevi, and H Le Gall. Effect of annealing on the structural and magnetic properties of giant magnetostrictive multilayers. *Journal of magnetism and magnetic materials*, 290:839–842, 2005.

[6] WANG Wei, MI Yiming, QIAN Shiqiang, and ZHOU Xiying. Magnetic and magne-

tostrictive properties of amorphous TbFe/FeAl multilayer thin film. *Journal of Rare Earths*, 26(4):571–574, 2008.

[7] A Grenier, J Juraszek, N Tiercelin, J Teillet, M Toulemonde, and JM Le Breton. Magnetostrictive properties of kr-ion irradiated multilayers. *Journal of magnetism and magnetic materials*, 310(2):2624–2626, 2007.

[8] R Ranchal, V Gutiérrez-Díez, and V González-Martín. Magnetic properties of nanostructured systems based on $TbFe_2$. *Journal of alloys and compounds*, 536:S329–S332, 2012.

[9] Pablo Bartolomé and Rocío Ranchal. Synthetic domain walls in $[TbFeGa/TbFe]_2$ multilayers. *Nanotechnology*, 31(33):335715, 2020.

[10] Bernard Dennis Cullity and Chad D Graham. *Introduction to magnetic materials*. John Wiley & Sons, 2011.

[11] S Mangin, C Bellouard, S Andrieu, F Montaigne, P Ohresser, NB Brookes, and B Barbara. Magnetization reversal in exchange-coupled GdFe/TbFe studied by x-ray magnetic circular dichroism. *Physical Review B*, 70(1):014401, 2004.

[12] Biplab Sanyal, Carolin Antoniak, Till Burkert, Bernhard Krumme, Anne Warland, Frank Stromberg, Christian Praetorius, Kai Fauth, Heiko Wende, and Olle Eriksson. Forcing ferromagnetic coupling between rare-earth-metal and 3 d ferromagnetic films. *Physical review letters*, 104(15):156402, 2010.

[13] Chao-Cheng Lin, Chih-Huang Lai, n bilayers DH Wei, YJ Hsu, and Han-Ping D Shieh. Thickness dependence of co anisotropy in TbFe/Co exchange-coupled bilayers. *Journal of applied physics*, 95(11):6846–6848, 2004.

[14] DH Wei, YJ Hsu, Chao-Cheng Lin, Chih-Huang Lai, JY Ou, and Jong-Ching Wu. Layer-

and lateral-resolved magnetization studies using photoemission electron microscopy. *Journal of magnetism and magnetic materials*, 282:49–52, 2004.

[15] Y Choi, D Haskel, RE Camley, DR Lee, JC Lang, G Srajer, JS Jiang, and SD Bader. Temperature evolution of the gd magnetization profile in strongly coupled Gd/Fe multilayers. *Physical Review B*, 70(13):134420, 2004.

[16] Nobuhiko Sakai, Ritthikrai Chai-Ngam, Akihisa Koizumi, and Hisao Kobayashi. Experimental study on interlayer magnetic coupling in sputtered Al/Fe/Al/Gd magnetic multilayer films: II. hysteresis curves of x-ray magnetic circular dichroism at the Gd-L_3 edge. *Journal of the Physical Society of Japan*, 79(6):064703, 2010.

[17] D Haskel, G Srajer, JC Lang, J Pollmann, CS Nelson, JS Jiang, and SD Bader. Enhanced interfacial magnetic coupling of Gd/Fe multilayers. *Physical review letters*, 87(20):207201, 2001.

[18] BT Thole, Paolo Carra, F Sette, and Gerrit van der Laan. X-ray circular dichroism as a probe of orbital magnetization. *Physical review letters*, 68(12):1943, 1992.

[19] Yoshiki Teramura, Arata Tanaka, and Takeo Jo. Effect of coulomb interaction on the x-ray magnetic circular dichroism spin sum rule in 3d transition elements. *Journal of the Physical Society of Japan*, 65(4):1053–1055, 1996.

[20] Yoshiki Teramura, Arata Tanaka, Thole BT, and Takeo Jo. Effect of coulomb interaction on the x-ray magnetic circular dichroism spin sum rule in rare earths. *Journal of the Physical Society of Japan*, 65(9):3056–3059, 1996.

[21] S Ingvarsson, Gang Xiao, SSP Parkin, and William J Gallagher. Thickness-dependent magnetic properties of $Ni_{81}Fe_{19}$, $Co_{90}Fe_{10}$ and $Ni_{65}Fe_{15}Co_{20}$ thin films. *Journal of magnetism and magnetic materials*, 251(2):202–206, 2002.

[22] R Ranchal, E López, JL Prieto, and C Aroca. Enhancement of the crystallization of Tb_xFe_{1-x} thin films upon the formation of α-Tb phase. *Acta Materialia*, 59(7):2865–2871, 2011.

[23] R Hussain, B Brahma, RK Basumatary, R Brahma, S Ravi, SK Srivastava, et al. Sperimagnetism in perpendicularly magnetized Co-Tb alloy-based thin films. *Journal of Superconductivity and Novel Magnetism*, 32(12):4027–4031, 2019.

[24] Birgit Hebler, Alexander Hassdenteufel, Patrick Reinhardt, Helmut Karl, and Manfred Albrecht. Ferrimagnetic Tb–Fe alloy thin films: composition and thickness dependence of magnetic properties and all-optical switching. *Frontiers in Materials*, 3:8, 2016.

[25] MA Laguna-Marco, Jesús Chaboy, and Cristina Piquer. Experimental determination of the R(5 d)- T(3d) hybridization in rare-earth intermetallics. *Physical Review B*, 77(12):125132, 2008.

[26] DM Eagles. Models for the heavy rare earth metals and (rare earth) Fe_2 compounds involving 5d and 6s electrons. *Physik der kondensierten Materie*, 16(3):181–199, 1973.

[27] Paymon Shirazi, Taehwan Lee, Mohanchandra K Panduranga, Alpha T N'Diaye, Anthony Barra, and Gregory P Carman. Rare-earth orbital moment contributions to the magnetic anisotropy in magnetostrictive $Tb_{0.3}$ $Dy_{0.7}Fe_2$. *Applied Physics Letters*, 118(16):162401, 2021.

[28] H-C Su, M-J Huang, H-J Lin, C-H Lee, C-T Chen, C-H Liu, H-F Hsu, K-W Lin, and J van Lierop. Connection between orbital moment enhancement and exchange bias in a [ni 80 fe 20/mn] 3 multilayer. *Physical Review B*, 87(1):014402, 2013.

[29] Jinghua Song, Yuansha Chen, Xiaobing Chen, Tahira Khan, Furong Han, Jine Zhang, Hailin Huang, Hui Zhang, Wenxiao Shi, Shaojin Qi, et al. Electric tuning of magnetic anisotropy and exchange bias of la 0.8 sr 0.2 co o 3/la 0.67 sr 0.33 mn o 3 bilayer films. *Physical Review Applied*, 14(2):024062, 2020.

Chapter 6

Magnetostriction in antiferromagnetic γ-Fe_xMn_{1-x} thin-films

6.1 Introduction

Antiferromagnet (AFM) thin films have become a candid alternative to ferromagnets (FM) in memory device applications due to their lack of stray-fields [1] and intrinsically faster resonances [2]. Additionally, their availability with metallic [3], semiconducting [4], or insulating material properties [5] allows their readily availability towards a wider array of device designs and configurations. Successful 90°reorientation of the Nèel vector in several collinear metallic AFMs by spin-orbit torques (SOTs) have been performed which displays the strong aptitude of AFMs in future memory applications [6, 7, 8]. However, more recent studies have determined that the reorientation of the Nèel vector by SOT in metallic AFMs are in fact due to current-induced localized heating causing expansion of the crystal lattice generating strains [9, 10, 11]. With the difficulty in assessing the thermal expansion due to such induced-currents, researchers have now turned their interest towards more direct

studies utilizing strains to reorient the Nèel vector in AFMs. However, studies conducted on various AFM thin films have not been able to provide a direct method for measuring the direct response of the Nèel vector (AFM moment) resultant from applied strains such as the saturation magnetostriction (λ_s) commonly measured in ferri and ferromagnets. As a result, closer examination of similar induced strains towards the reorientation of the AFM Nèel vector are required with the aim to determine λ_s in AFMs.

Previous work has shown strain-mediated magnetoresistance changes in several metallic AFM thin films coupled to piezoelectric substrates. These studies have demonstrated that induced strains generated by the application of an electric field to a piezoelectric substrate alters the resistance which indirectly correlates to the reorientation of the Nèel vector [12]. More direct observations of the Nèel vector reorientation have reported a reduction in the spin-flop field (H_{sf}) in NiO through strains induced by PMN-PT by the measuring spin-hall magnetoresistance (SMR) [13]. Other investigations utilized X-ray magnetic linear dichroism (XMLD) [14] and found that a 0.1% tensile strain in Mn2Au is sufficient to cause spin-flop transition normally requiring an applied field of 70 T [15]. Similarly, for a $Fe_{50}Mn_{50}$ thin film coupled to NiTi shape memory alloy substrate demonstrated a 90°reorientation in the Nèel vector by application of -1.3% strain obtained by changes in the linear dichorism [16]. Additionally, XMLD-photoemission electron microscopy (XMLD-PEEM) has been utilized to directly visualize the reorientation of the Nèel vector and domain wall motion in Mn_2Au [17] and $LaFeO_3$ [18], which are commonly observed in magnetostrictive FMs. These results show considerable promise for strain-mediated control of the Nèel vector in future memory applications and provide experimental evidence of magnetostrictive properties in AFMs. However, these studies do not directly provide a method to determine nor correlate the magnitude of the strain to the reorientation of the Nèel vector (i.e. magnetostriction) in AFMs.

Measurement of the magnetostrictive properties in AFMs have been widely absent due to

the difficulty in the application of the large magnetic fields required to saturate AFMs beyond their H_{sf}. Direct measurement of the magnetostriction in AFMs began with the bulk room-temperature AFM NiO, reporting magnetostriction values up to -20 ppm [19, 20]. For metallic AFMs, investigations on the bulk polycrystalline γ-FeMn alloys have shown considerably large magnetostriction with results ranging from 350 [21] to 750 ppm [22] originating from one group. However, more recent investigations on bulk γ-FeMn alloys have contradicted previous results with the reported absence of magnetostriction in several compositions of γ-$Fe_{1-x}Mn_x$ (x=0.38, 0.42, 0.46, 0.50, & 0.56) [23]. It was also found that in an exchange biased NiFe/FeMn thin film bilayer, the exchange bias field decreased when the films were deposited with more compressive stresses [24]. Furthermore, a strain-induced phase transition from γ-FeMn to α-FeMn has been reported in epitaxial $Fe_{50}Mn_{50}$ films by a 0.3% tensile strain caused by lattice mismatch between the film and the substrate upon cooling down to room temperature from growth conditions [25]. Additionally, first-principles ab-initio calculations have found that γ-FeMn possesses pronounced orbital-magnetostrictive properties which are largely governed by the strain-state (i.e. volume) of the lattice [26]. Therefore, the results of these combined studies indicate that both the γ-phase and the stress-state (i.e. compressive stress) of FeMn alloys largely constitutes its magnetostrictive properties.

In this work, we employ the magnetron sputtering process to adjust the Argon (Ar) pressures in the deposition of polycrystalline FeMn thin films on Silicon substrates to vary film residual stresses and study the influence of strain on the orientation of the Nèel vector. We demonstrate a strain-induced phase transition from α-FeMn to γ-FeMn by a -0.03% compressive strain (-55 MPa stress). Additionally, AC susceptibility measurements show an in-plane to out-of-plane reorientation (i.e. 90°reorientation) in the γ-FeMn Nèel vector followed by a 12 kOe increase in the spin-flop field resultant from a -0.028% compressive strain (-52 MPa stress). From the measured AC and DC susceptibility data, our calculations indirectly predict a saturation magnetostriction value of 305 ppm in our FeMn thin films.

6.2 Experimental Setup

Three Fe_xMn_{1-x} thin films were deposited onto 4-inch (100) silicon substrates by ultra-high vacuum DC magnetron sputtering from a single alloy target ($Fe_{50}Mn_{50}$ at.%) with a sputtering power of 205 W at a base chamber pressure of $1x10^{-6}$ Torr without substrate heating. The three films were deposited with Ar working pressures of 5, 10, or 15 mTorr respectively producing films with different residual stresses. All films had a 10 nm Ta barrier and a 5 nm Ta capping layer deposited prior and post-deposition without breaking vacuum. Wafer curvature measurements taken prior and post-deposition of the films were utilized with Stoney's equation [27] to determine residual stresses using Si and Fe_xMn_{1-x} Young's moduli of 130 GPa [28] and 180 GPa [29] respectively. X-ray diffraction (XRD) in Bragg-Brentano geometry verified the crystal structure and phases present by scanning the 2θ angle from 35°to 60°. Inductively coupled plasma mass spectrometry (ICP-MS) was used to determine the chemical composition of the films. In-plane (IP) and out-of-plane (OOP) DC M-H curves were measured by sweeping the magnetic field between -60 kOe to 60 kOe using Scanning Quantum Interference Device (SQUID) magnetometry at 300 K. IP and OOP AC susceptibility measurements were performed in-situ with the DC M-H measurements by SQUID with an AC magnetic field amplitude of 10 Oe at a frequency of 7.69 Hz.

6.3 Results & Discussion

Figure 6.1(a) shows the residual stress (left ordinate axis) and Fe atomic composition (right ordinate axis) versus the Argon (Ar) working pressure for the Fe_xMn_{1-x} thin films andFigure 6.1(b) shows the XRD spectra of the three Fe_xMn_{1-x} films deposited at 5, 10, and 15 mTorr followed by the references for the α-FeMn and γ-FeMn phases. 6.1(a) shows the significant changes in the residual stresses in the Fe_xMn_{1-x} films as the Ar pressures are increased from 5

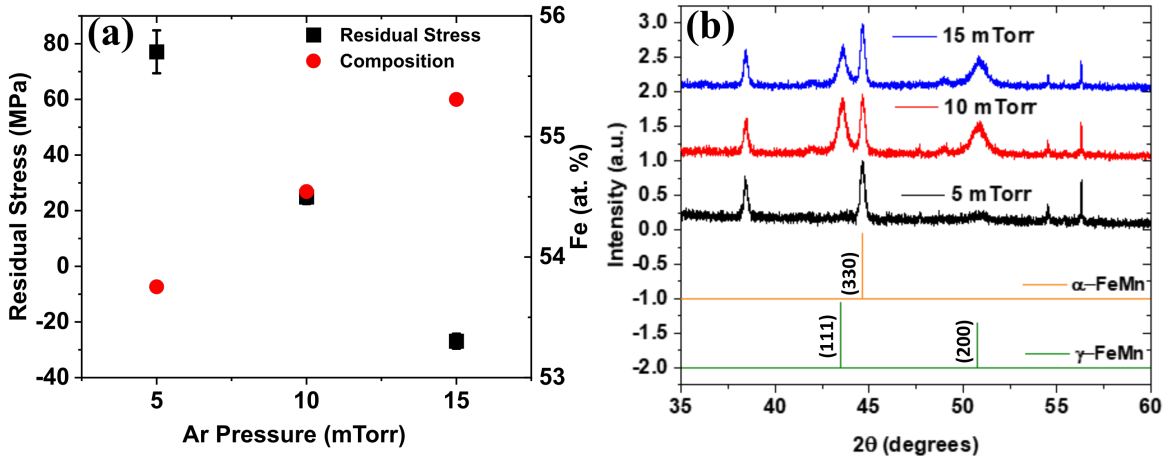

Figure 6.1: (a) Residual Stress and Fe atomic composition versus the Ar working pressure. (b) X-ray diffraction (XRD) spectra for the 5, 10 and 15 mTorr FeMn films with the references for α-FeMn and γ-FeMn phases.

to 15 mTorr altering the film residual stress from 77 MPa (tensile) to -27 MPa (compressive). However, only modest changes in the Fe atomic composition are found increasing from 53.8 to 55.3 at.% Fe as the Ar pressure increases from 5 to 15 mTorr. In 6.1(b), the XRD spectra indicates that all films are polycrystalline with an average grain size of 5 nm for all films. For the 5 mTorr film, only the α-FeMn phase is observed with the corresponding (110) peak at 44.6°[30]. However, the XRD spectra of the 10 and 15 mTorr films also show the presence of the γ-FeMn phase with the two peaks (111) and (200) peaks at 43.6°and 50.8°respectively [31] along with the α-FeMn (311) peak located at 44.6°. Referring to the equilibrium phase diagram for the FeMn alloy, our as-deposited films without post-deposition annealing may exhibit either an amorphous structure absent of a crystallographic phase or only the α-FeMn within the measured compositional range (i.e. Fe_xMn_{1-x} $0.538<x<0.553$) of our films and require thermal treatment to transform into the γ-FeMn phase [32]. Additionally, based on first-principles energy calculations, both phases can coexist while the γ-phase possesses a higher energy state across the Fe at.% compositional range in our films [26]. This suggests that the γ-FeMn phase present in the 10 and 15 mTorr films are induced by altering the energy landscape through a -0.03% tensile strain observed in previous reports [25].

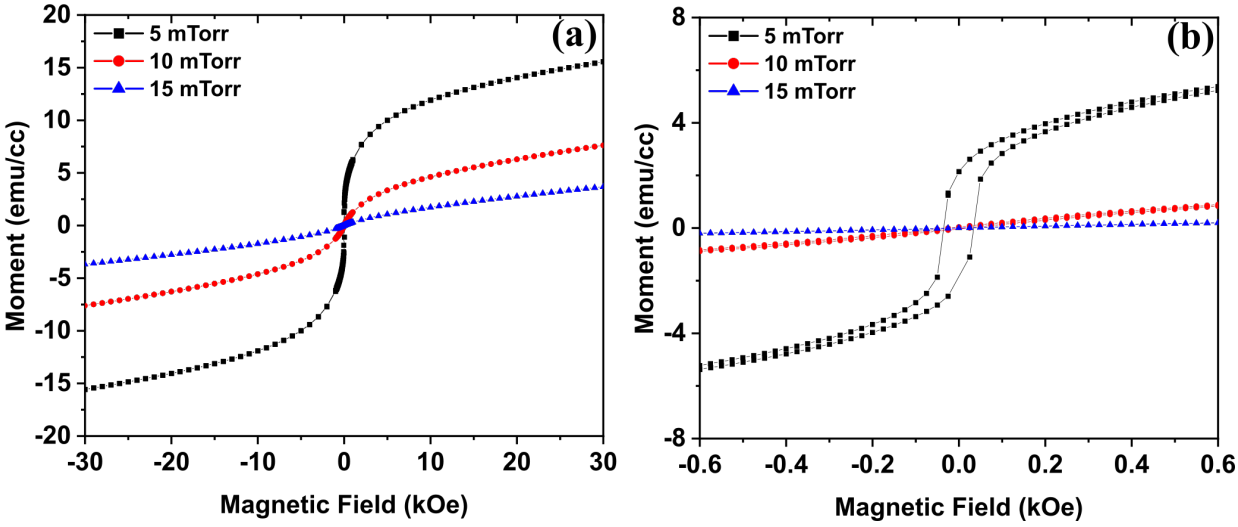

Figure 6.2: M-H curves measured by scanning quantum interference device (SQUID) magnetometry for the 5, 10, and 15 mTorr FeMn films from (a) -30 to 30 kOe (b) low-field magnetic properties from -0.6 to 0.6 kOe.

Figure 6.2 shows the IP DC M-H curves for the 5, 10 and 15 mTorr FeMn films from -30 to 30 kOe with the provided inset showing the low field magnetic responses of the films within the range of -0.6 to 0.6 kOe. It can be seen that the 5 mTorr FeMn film with only the α-FeMn phase shows the largest magnetic response following a magnetic remanence of 3 emu/cc and a coercive field of 325 Oe by referring to the inset. However, the 10 and 15 mTorr films show much lower moment values as compared to the 5 mTorr film as they also possess both α and γ phases of FeMn. Referring to the inset showing the low field magnetic behavior, the 10 and 15 mTorr films lack magnetic remanence, coercive fields, and do not saturate while showing a linear positive slope in their M-H responses expected in AFMs. Comparing the 15 mTorr film with a compressive stress of -27 MPa to the 10 mTorr film with a tensile stress of 25 MPa, it can be seen that the 15 mTorr film shows a lower moment. This indicates that as the film residual stresses become compressive (i.e. 25 MPa to -27 MPa), the films show magnetic behavior more indicative of the γ-FeMn phase [33]. Due to the antiferromagnetic responses in the 10 and 15 mTorr films, it is necessary to measure the IP and OOP DC M-H curves followed by AC susceptibility measurements to investigate moment reorientations in

the α and γ phases.

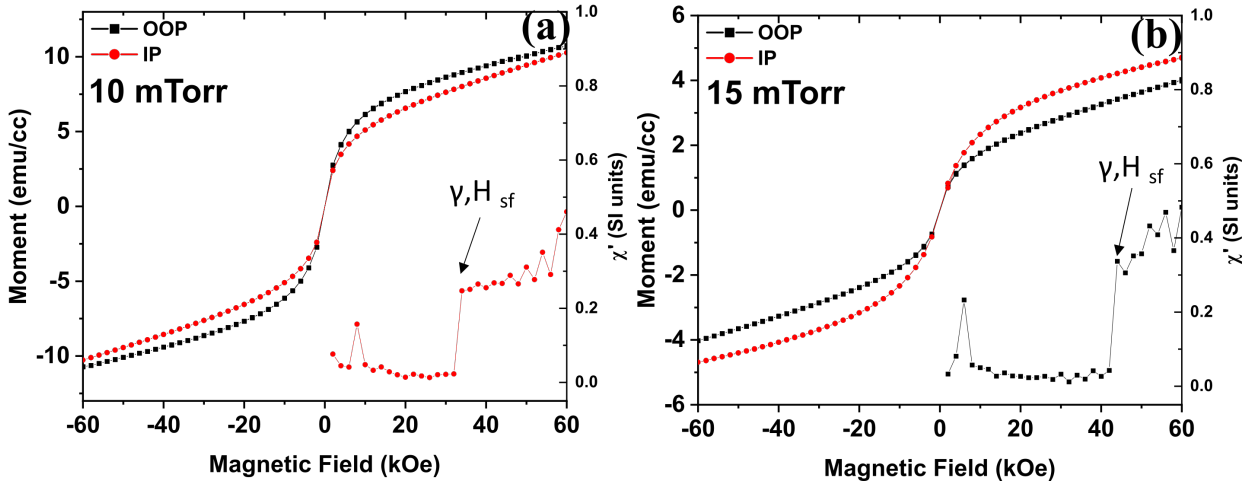

Figure 6.3: IP and OOP DC M-H curve (left ordinate axis) and real-part of the volume AC susceptibility ($\chi_v^{'}$) (right ordinate axis) for the FeMn films deposited at (a) 10 mTorr and (b) 15 mTorr.

Figure 6.3 shows the IP and OOP DC M-H curve (left ordinate axis) and the real-part of volume AC susceptibility ($\chi_v^{'}$) (right ordinate axis) for the FeMn films deposited at (a) 10 mTorr and (b) 15 mTorr. Measuring the AC susceptibility while sweeping the magnetic field at constant temperature offers a convenient and accurate method for the determining the AFM H_{sf} [34]. In Figure 6.3(a), the AC susceptibility measurement results find that only the IP direction shows a spin-flop transition at a magnetic field of 34 kOe where for the OOP orientation shows noise at higher susceptibility values an order higher compared to the IP direction. These results agree with the DC M-H response, as the IP orientation shows a lower moment (i.e. susceptibility). The combined AC susceptibility and DC M-H responses indicate that the Nèel vector lies IP for the 10 mTorr film as the susceptibility is expected to be lower when magnetic fields are applied parallel to the Nèel vector. Additionally, the IP AC susceptibility measurement for the 10 mTorr film shows a peak at 8 kOe which may indicate the reorientation of α-FeMn phase. In Figure 6.3(b), the measured AC susceptibility measurements in the OOP orientation show the spin-flop transition at 44 kOe, while the IP measurements show noise at susceptibility values an order of magnitude larger compared

to the OOP direction. Additionally, DC M-H curves for the 15 mTorr film show that the OOP orientation shows a lower moment value (i.e. susceptibility) as compared to the IP direction. Combining the AC susceptibility measurements and the DC M-H curve responses for the 15 mTorr film implies that the Nèel vector in this film lies OOP. Furthermore, the AC susceptibility response shows a peak at 4 kOe which may correspond to the reorientation of the α-FeMn phase. Assuming that only the residual stresses between the two films are different, a resultant compressive stress of -52 MPa (i.e. -0.028% strain) is sufficient to cause an IP to OOP reorientation of the Nèel vector in γ-FeMn.

Next the influence of strain towards the magnitude of H_{sf} will be investigated to indirectly determine a saturation magnetostriction λ_s in γ-FeMn. The stress-free H_{sf} [35, 36] is given by the equation below

$$H_{sf} = [H_{ex} 2Ha]^{1/2} \tag{6.1}$$

where H_{ex} is the exchange field controlling the antiparallel alignment of the AFM sublattice moments, and H_a is the anisotropy energy which for an antiferromagnet with uniaxial [37] reduces to

$$H_a = \frac{2K_1}{\mu_0 M} \tag{6.2}$$

where K_1 is the uniaxial anisotropy energy, μ_0 is the permeability of free space, and M is the magnetization at the spin-flop field when the sublattice moments cant. Therefore, for a

stress-free AFM, 6.1 can be written as follows.

$$H_{sf}^{eq} = [4\frac{H_{ex}}{\mu_0 M}K_1]^{1/2} \tag{6.3}$$

However, when stresses are present in the system, the newly induced the magnetoelastic and elastic anisotropies add the effective field terms (H_{me}) and (H_{el}) alter the equilibrium H_{sf} given by 6.4.

$$H_{sf} = [2H_{ex}(H_a + H_{me} + H_{el})]^{1/2} \tag{6.4}$$

this indicates that stresses can alter H_{sf} without directly fighting AFM exchange H_{ex}. Equation 6.4 then can be written as follows

$$H_{sf} = [2\frac{H_{ex}}{\mu_0 M}(2K_1 + \frac{3}{2}\lambda_s\sigma + \frac{\sigma^2}{2Y})]^{1/2} \tag{6.5}$$

where λ_s is the saturation magnetostriction, σ is the stress, and Y is the Young's modulus. Now if we include the equilibrium H_{sf}^{eq} to 6.5, H_{sf} in terms of σ can be determined.

$$H_{sf}(\sigma) = H_{sf}^{eq}[1 + (\frac{3\lambda_s\sigma}{4K_1} + \frac{\sigma^2}{4YK_1})]^{1/2} \tag{6.6}$$

In equation 6.5, it can be seen that the relationship between the stress and the H_{sf} are virtually linear. From Figure 6.3 the 10 mTorr film under -25 MPa shows a H_{sf} of 34 kOe whereas the 15 mTorr film under 27 MPa is 44 kOe. Taking values of K_1 of -9.5 kJ/m^3 based on reported values [38, 39] for Fe-based FCC alloys, we find H_{sf}^{eq} of 41.2 kOe and λ_s equal to 116 ppm. The approximated λ_s value reasonably agrees with previous reports of magnetostriction for polycrystalline Fe_xMn_{1-x} ($0.40 < x < 0.60$) alloys between 300 to 750 ppm [21, 22]. Additionally, λ_s values for γ-FeMn alloys may be larger than what we report here due to the nanocrystalline nature of the films which may exhibit a reduction in the spin-orbit coupling compared to polycrystalline or epitaxial films. However, previous studies have demonstrated that AFMs which undergo strain-mediated reorientation in their Nèel vectors must possess low MCA as it directly influences the magnitude of H_{sf} as demonstrated by equation 6.3 [2]. For reference, in comparison to Mn_2Au which possesses a H_{sf} of 700 kOe [17] and K_1 700x10^3 kJ/m^3 [40], FeMn shows a H_{sf} an order of magnitude lower since the K_1 term is an order of magnitude lower compared to Mn_2Au which demonstrates the critical importance for low MCA for strain-mediated reorientations in AFMs. Next the stress response towards the AFM behavior is evaluated by a theoretical model based on 6.6.

Figure 6.4 shows a stress-based magnetic phase diagram shown by the curve calculated using equation 6.6 with $K_1 = -9.5$ kJ/m^3 and $\lambda_s = 116$ ppm along with the experimental data points for the 3 FeMn films shown by the red squares. The plot shows 2 regions in total composed of one ferromagnetic (Fm) and one antiferromagnetic (AFM) region, where the phase-boundary between two regions is located at 56.4 MPa (0.032%). The FM regions do not have a H_{sf} and show only imaginary portions when using equation 6.6 meaning they cannot naturally exist as an AFM. However, within the AFM region are real numbers were determined for the stresses using equation 6.6. Additionally, the theoretical curve agrees well with our data as the film under 77 MPa showed FM magnetic properties in the α phase, whereas the other two films behaved similar to AFMs with the γ phase. In the determination of the theoretical curve, the AFM boundary region became wider as the K_1 term increased

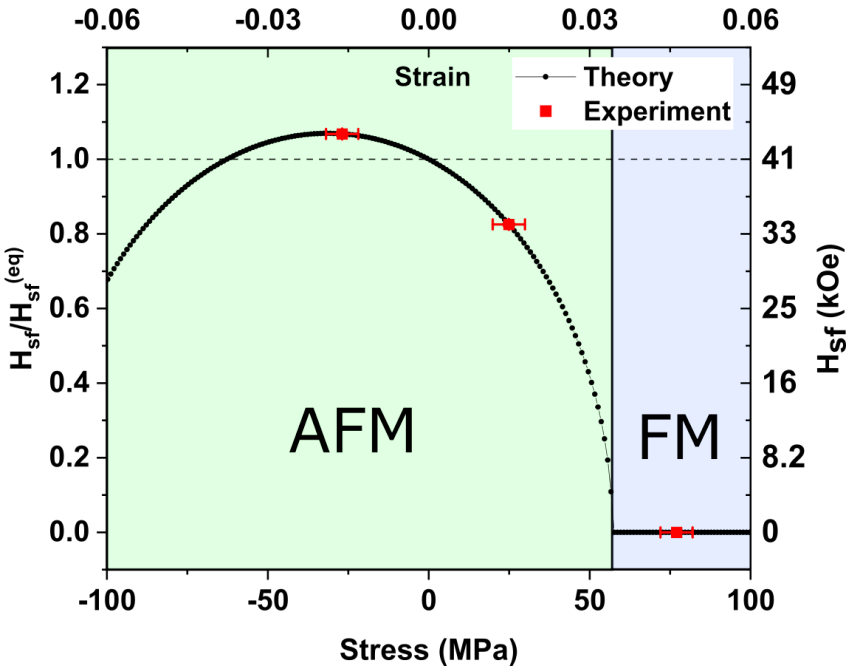

Figure 6.4: Magnetic phase diagram of FeMn as a function of stress from -100 MPa to 100 MPa. H_{sf}/H_{sf}^{eq} (left-ordinate axis) and H_{sf} (right-ordinate axis) vs stress (bottom) and strain (top).

in magnitude. Therefore, referring back to equation 6.6, the magnetoelastic response (i.e. λ_s) has to be larger in order to overcome the larger MCA as K_1 increases.

6.4 Conclusion

In this work, we employ the magnetron sputtering process to adjust the Argon pressures in the deposition of polycrystalline FeMn thin films on Silicon substrates to vary film residual stresses and study the influence of strain on the orientation of the Nèel vector. We demonstrate a strain-induced phase transition from α-FeMn to γ-FeMn by a -0.03% compressive strain (-55 MPa stress). Additionally, AC susceptibility measurements show an in-plane to out-of-plane reorientation (i.e. 90°reorientation) in the γ-FeMn Nèel vector significantly less than the reported -1.3% strain in a previous study. Furthermore, this reorientation in the

Nèel vector as a result of the -0.028% compressive strain was found to increase the spin-flop field by 10 kOe. From the measured AC and DC susceptibility data, our calculations indirectly predict a saturation magnetostriction value of 116 ppm for our FeMn thin films. We find that these results are critical for researchers investigating the strain-mediated properties in AFM materials and demonstrates the viability of strain-mediated control of the Nèel vector in future spintronic applications.

Chapter References

[1] Tomas Jungwirth, X Marti, P Wadley, and J Wunderlich. Antiferromagnetic spintronics. *Nature nanotechnology*, 11(3):231–241, 2016.

[2] Anthony Barra, John Domann, Ki Wook Kim, and Greg Carman. Voltage control of antiferromagnetic phases at near-terahertz frequencies. *Physical Review Applied*, 9(3):034017, 2018.

[3] Saima A Siddiqui, Joseph Sklenar, Kisung Kang, Matthew J Gilbert, André Schleife, Nadya Mason, and Axel Hoffmann. Metallic antiferromagnets. *Journal of Applied Physics*, 128(4):040904, 2020.

[4] I Fina, X Marti, D Yi, J Liu, JH Chu, C Rayan-Serrao, S Suresha, AB Shick, J Železnỳ, T Jungwirth, et al. Anisotropic magnetoresistance in an antiferromagnetic semiconductor. *Nature communications*, 5(1):1–7, 2014.

[5] Natascha Hedrich, Kai Wagner, Oleksandr V Pylypovskyi, Brendan J Shields, Tobias Kosub, Denis D Sheka, Denys Makarov, and Patrick Maletinsky. Nanoscale mechanics of antiferromagnetic domain walls. *Nature Physics*, 17(5):574–577, 2021.

[6] Shunsuke Fukami, Chaoliang Zhang, Samik DuttaGupta, Aleksandr Kurenkov, and Hideo Ohno. Magnetization switching by spin–orbit torque in an antiferromagnet–ferromagnet bilayer system. *Nature materials*, 15(5):535–541, 2016.

[7] Jing Zhou, Xiao Wang, Yaohua Liu, Jihang Yu, Huixia Fu, Liang Liu, Shaohai Chen, Jinyu Deng, Weinan Lin, Xinyu Shu, et al. Large spin-orbit torque efficiency enhanced by magnetic structure of collinear antiferromagnet irmn. *Science advances*, 5(5):eaau6696, 2019.

[8] XF Zhou, J Zhang, F Li, XZ Chen, GY Shi, YZ Tan, YD Gu, MS Saleem, HQ Wu, F Pan, et al. Strong orientation-dependent spin-orbit torque in thin films of the antiferromagnet mn 2 au. *Physical Review Applied*, 9(5):054028, 2018.

[9] Hendrik Meer, Felix Schreiber, Christin Schmitt, Rafael Ramos, Eiji Saitoh, Olena Gomonay, Jairo Sinova, Lorenzo Baldrati, and Mathias Klaui. Direct imaging of current-induced antiferromagnetic switching revealing a pure thermomagnetoelastic switching mechanism in nio. *Nano Letters*, 21(1):114–119, 2020.

[10] MS Wörnle, P Welter, Z Kašpar, K Olejník, V Novák, RP Campion, P Wadley, T Jungwirth, CL Degen, and P Gambardella. Current-induced fragmentation of antiferromagnetic domains. *arXiv preprint arXiv:1912.05287*, 2019.

[11] Pengxiang Zhang, Joseph Finley, Taqiyyah Safi, and Luqiao Liu. Quantitative study on current-induced effect in an antiferromagnet insulator/pt bilayer film. *Physical review letters*, 123(24):247206, 2019.

[12] Han Yan, Zexin Feng, Shunli Shang, Xiaoning Wang, Zexiang Hu, Jinhua Wang, Zengwei Zhu, Hui Wang, Zuhuang Chen, Hui Hua, et al. A piezoelectric, strain-controlled antiferromagnetic memory insensitive to magnetic fields. *Nature nanotechnology*, 14(2):131–136, 2019.

[13] A Barra, Andrew Ross, Olena Gomonay, Lorenzo Baldrati, A Chavez, Romain Lebrun, JD Schneider, Paymon Shirazi, Q Wang, Jairo Sinova, et al. Effective strain manipulation of the antiferromagnetic state of polycrystalline nio. *Applied Physics Letters*, 118(17):172408, 2021.

[14] Xianzhe Chen, Xiaofeng Zhou, Ran Cheng, Cheng Song, Jia Zhang, Yichuan Wu, You Ba, Haobo Li, Yiming Sun, Yunfeng You, et al. Electric field control of néel spin–orbit torque in an antiferromagnet. *Nature materials*, 18(9):931–935, 2019.

[15] AA Sapozhnik, R Abrudan, Yu Skourski, M Jourdan, H Zabel, M Kläui, and H-J Elmers. Manipulation of antiferromagnetic domain distribution in mn2au by ultrahigh magnetic fields and by strain. *physica status solidi (RRL)–Rapid Research Letters*, 11(4):1600438, 2017.

[16] Chun Feng, Yukun Li, Lei Wang, Yi Cao, Mingke Yao, Fei Meng, Feng Yang, Baohe Li, Kaiyou Wang, and Guanghua Yu. Giant strain control of antiferromagnetic moment in metallic femn by tuning exchange spring structure. *Advanced Functional Materials*, 30(14):1909708, 2020.

[17] S Yu Bodnar, Mariia Filianina, SP Bommanaboyena, T Forrest, F Maccherozzi, AA Sapozhnik, Y Skourski, Mathias Kläui, and Martin Jourdan. Imaging of current induced néel vector switching in antiferromagnetic mn 2 au. *Physical Review B*, 99(14):140409, 2019.

[18] A Scholl, J Stöhr, J Lüning, Jin Won Seo, J Fompeyrine, H Siegwart, J-P Locquet, F Nolting, S Anders, EE Fullerton, et al. Observation of antiferromagnetic domains in epitaxial thin films. *Science*, 287(5455):1014–1016, 2000.

[19] L Alberts and EW Lee. Magnetostriction in antiferromagnetic nickel oxide. *Proceedings of the Physical Society (1958-1967)*, 78(5):728, 1961.

[20] TR McGuire and WA Crapo. Magnetic susceptibility and magnetostriction of coo, mno, and nio. *Journal of Applied Physics*, 33(3):1291–1292, 1962.

[21] WY Peng and JH Zhang. Magnetostriction studies in an antiferromagnetic polycrystalline mn 42 fe 58 alloy. *Applied physics letters*, 89(26):262501, 2006.

[22] Aina He, Tianyu Ma, Jingjing Zhang, Wei Luo, and Mi Yan. Antiferromagnetic mn50fe50 wire with large magnetostriction. *Journal of magnetism and magnetic materials*, 321(22):3778–3781, 2009.

[23] R Sato Turtelli, C Grijalva, F Kubel, D Geist, R Grössinger, M Kriegisch, S Sorta, M Zehetbauer, and N Mehmood. Low magnetostriction in fe100-xmnx (x= 45, 48, 50, 52, 55) alloys. In *IOP Conference Series: Materials Science and Engineering*, volume 60, page 012006. IOP Publishing, 2014.

[24] E Linville, D Han, J Judy, J Sivertson, and S Mao. Stress effects on the magnetic properties of femn and nimn spin valves. *IEEE transactions on magnetics*, 34(4):894–896, 1998.

[25] Younghun Hwang, Sungyoul Choi, Jeongyong Choi, and Sunglae Cho. Induced high-temperature ferromagnetism by structural phase transitions in strained antiferromagnetic γ-fe 50 mn 50 epitaxial films. *Scientific reports*, 9(1):1–10, 2019.

[26] Jan-Philipp Hanke, Frank Freimuth, Stefan Blügel, and Yuriy Mokrousov. Prototypical topological orbital ferromagnet γ-femn. *Scientific reports*, 7(1):1–7, 2017.

[27] Yin Zhang and Ya-pu Zhao. Applicability range of stoney's formula and modified formulas for a film/substrate bilayer. *Journal of applied physics*, 99(5):053513, 2006.

[28] E Török, M Weller, and G Hausch. Young's modulus of fe-mn. *Le Journal de Physique Colloques*, 44(C9):C9–477, 1983.

[29] Euan J Boyd and Deepak Uttamchandani. Measurement of the anisotropy of young's modulus in single-crystal silicon. *Journal of Microelectromechanical Systems*, 21(1):243–249, 2011.

[30] Lu Xing, Qin Zuoxiang, Zhang Yansheng, Wang Xingyu, Li Fengxian, Ding Bingzhe, and Hu Zhuangqi. Study of the paramagnetic-antiferromagnetic transition and the γ ε

martensitic transformation in fe-mn alloys. *Journal of materials science*, 35(22):5597–5603, 2000.

[31] Till Jurgeleit, Lea Katharina Jessen, Eckhard Quandt, and Christiane Zamponi. Magnetron-sputtered, biodegradable femn foils: The influence of manganese content on microstructure, mechanical, corrosion, and magnetic properties. *Materials*, 11(4):482, 2018.

[32] Yoshikazu Ishikawa, Hisashi Sekine, and Kazuyoshi Yamada. Magnetic phase diagram of γ femn alloys. *Journal of the Physical Society of Japan*, 37(3):874–874, 1974.

[33] Bernard Dennis Cullity and Chad D Graham. *Introduction to magnetic materials*. John Wiley & Sons, 2011.

[34] Björn Westerstrand, Per Nordblad, and Lars Nordborg. The magnetocrystalline anisotropy constants of iron and iron-silicon alloys. *Physica Scripta*, 11(6):383, 1975.

[35] D Mauri, HC Siegmann, PS Bagus, and E Kay. Simple model for thin ferromagnetic films exchange coupled to an antiferromagnetic substrate. *Journal of Applied Physics*, 62(7):3047–3049, 1987.

[36] NC Koon. Calculations of exchange bias in thin films with ferromagnetic/antiferromagnetic interfaces. *Physical review letters*, 78(25):4865, 1997.

[37] John MD Coey. *Magnetism and magnetic materials*. Cambridge university press, 2010.

[38] Michael E McHenry, Matthew A Willard, and David E Laughlin. Amorphous and nanocrystalline materials for applications as soft magnets. *Progress in materials Science*, 44(4):291–433, 1999.

[39] Ian Joseph McDonald. *Designing Magnetic Anisotropy in Ferrous Alloys*. PhD thesis, Northeastern University, 2018.

[40] VMTS Barthem, CV Colin, H Mayaffre, M-H Julien, and Dominique Givord. Revealing the properties of mn 2 au for antiferromagnetic spintronics. *Nature communications*, 4(1):1–7, 2013.

Chapter 7

Conclusion

This disseration addresses new investigation methods for the design of magnetostrictive intermetallic and multilayered materials with superior magnetic properties tailored for multiferroic applications. Element specific investigations of the spin and orbital momenta by XMCD and the XMCD sum rule approach were demonstrated, providing insight on the elements that control the MCA and magnetoelastic anisotropic responses in complex intermetallics such as Terfenol-D. Additionally, XMCD and its sum rule calculations were performed on multilayered RE-TM/TM heterostructures which show magnetization enhancements with ultra soft magnetic responses due to interface mediated interactions between specific elements in the hard and the soft layers. Furthermore, the orientation of the Néel vector with applied stresses (i.e. strains) in polycrystalline metallic AFM thin-films were investigated demonstrating the magnetoleastic response with the 90°Néel vector switching, followed by the saturation magnetostriction in AFM thin films. The results presented in this disseration aid in the development of superior energy-efficient and effective magnetostrictive ferri and antiferromagnetic thin films to meet the growing demand of micro and nanoscale magnetic devices in future spintronic applications.

Chapter 2 provides the fundamental concepts of magnetism discussed in this dissertation. This chapter begins by illustrating the origin of magnetism in materials at the atomic level. Further, a brief overview of the various types of magnetic ordering are introduced to provide the background for the research conducted on ferri and antiferromagnetic systems. Furthermore, the magnetization process and the origins of the hysteric behavior are briefly discussed to provide an introduction to the various energies that contribute towards the magnetic anisotropy, which is heavily referenced in chapters 4-6 of this dissertation.

Chapter 3 of this dissertation provides the background required to understand the X-Ray magnetic circular dichroism (XMCD) results in chapters 4 and 5. This first begins with the brief overview of the interaction of transmitting X-Rays with matter. Subsequently, X-Ray absorption (XAS) in materials are introduced followed by XAS several detection methods typically used in XAS experiments since these are prerequisites in understanding XMCD. Next, the fundamental concepts that produce the dichroic responses in magnetic materials with a net spontaneous magnetization in response to polarized circular X-Rays are provided to understand XMCD spectroscopy. Finally, the XMCD sum rules are introduced which utilize both the XAS and XMCD spectra in magnetic materials to determine the elemental spin and orbital angular momenta which are vital for grasping the results in chapters 4 and 5.

In chapter 4, soft X-Ray Magnetic Circular Dichroism (XMCD) spectroscopy at the Dy and Tb $M_{4,5}$ and the Fe $L_{2,3}$ edges were performed on sputter deposited polycrystalline Terfenol-D ($Tb_{0.3}Dy_{0.7}Fe_2$) film on sapphire substrates at temperatures from 100 to 300 K to evaluate the elementwise contribution to the magnetocrystalline anisotropy and coercive field. The elemental spin and orbital magnetic moments were calculated using the X-Ray Magnetic Circular Dichroism sum rules. As temperatures decreased, the Tb and Fe moments plateau at 200 K with values of 7.6 μ_B/atom and 1.8 μ_B/atom respectively while the Dy moment increases to 8.9 μ_B/atom at 100 K. Between 300 to 200 K the change in magnetic anisotropy

is dominated by thermally induced magnetoelastic effects while for temperatures below 200 K magnetocrystalline anisotropy (MCA) changes are dominant. The MCA changes below 200 K appear to be due to increases in the Dy orbital moment with decreasing temperature in this temperature regime.

In chapter 5 explores moment enhancements in two multilayers composed of ultra-thin $Ni_{81}Fe_{19}$ and $TbFe_2$ (2nm/4nm or 4nm/2nm) layers using X-ray magnetic circular dichroism (XMCD). The elementwise XMCD results indicate that these enhancements are induced by interface mediated antiparallel exchange coupling between Tb in the $TbFe_2$ and Fe in the $Ni_{81}Fe_{19}$. XMCD M-H curves demonstrate this coupling is sufficient to provide pronounced saturation and reorientation in the Tb orbital and spin moments with coercive fields similar to monolithic $Ni_{81}Fe_{19}$ at or near the interfaces. Results also show increased magnetic ordering lengths within $TbFe_2$ layers as the $TbFe_2$ layer thickness increases.

In chapter 6, the residual stresses in magnetron sputtered polycrystalline FeMn thin films on Silicon substrates were varied by adjusting the deposition Argon pressure to study the influence of strain on the orientation of the Néel vector. Here, a strain-induced phase transition from α-FeMn to γ-FeMn is demonstrated by a -0.03% compressive strain (-55 MPa stress). Futher, AC susceptibility measurements show an in-plane to out-of-plane reorientation (i.e. 90reorientation) in the γ-FeMn Néel vector followed by a 12 kOe increase in the spin-flop field resultant from a -0.028% compressive strain (-52 MPa stress). Calculations using measured AC and DC susceptibility data indirectly predict a saturation magnetostriction value of 305 ppm for γ-FeMn thin films.

The results demonstrated in this dissertation offer more insight on the future of magnetostrictive materials tailored to strain-mediated multiferroic applications. In addition, these results provide valuable insight for researchers in their investigations for the development of superior magnetostrictive intermetallics and multilayered materials by tailoring the anisotropic responses at the elemental spin and orbital moment level. Furthermore, demonstration of

the substantial magnetostrictive properties in metallic antiferromagnets are demonstrated which will support researchers in their investigation and development of magnetostrictive antiferromagnetic materials.